



PONTIFICIA UNIVERSIDAD CATOLICA DE CHILE
FACULTAD DE FISICA
INSTITUTO DE ASTROFISICA

SEARCHING FOR *I*-BAND DROPOUT GALAXIES
LENSED BY GALAXY CLUSTERS

BY

MARTIN TOURNEBOEUF

Tesis presented in the Faculty of Physics
of the Pontificia Universidad Católica de Chile
to obtain the title of Master in Astrophysics.

Supervisor : Dr. Felipe Barrientos

Correctors : Dr. Gaspar Galaz

Dr. Leopoldo Infante

Dr. Veronica Motta

August, 2013
Santiago, Chile

Thanks

Felipe Barrientos for guiding me through darkness.

Julien Girard for flattening space around mi geodesic.

Cristobal Armaza for guiding darkness through me.

The working group gravitating around Felipe or my classes for their inertial energy.

Rocio Sanhueza for receiving me in her tight binary system.

Mi parents for appending new event horizons into theirs.

Overall, I thank my dear reader for honouring this work by putting an eye (or more) on it.

The present work was financed by Pontificia Universidad Catolica de Chile and Felipe Barrientos.

Abstract

This report presents a search for i-band dropouts galaxies ($z \sim 6$) located around foreground galaxy clusters detected in the RCS2 or SDSS surveys and which are likely to magnify the brightness of the i -band dropouts allowing a future high S/N spectroscopic study of these sources. For each of the 24 clusters studied (12 from each survey), two images were obtained, in the H and I band. Furthermore, for 10 clusters of the RCS2, an image in the R band was also obtained. The depth of the images is 23.5, 24 and 24.4 mag_{AB} in H , I and R band respectively. Additional HST images in $F160W$, $F105W$, $F606W$ and $F390W$ were also obtained for 7 fields in the SDSS dataset but the photometry of i-band dropouts, detected in the H band, was not extracted from HST images due to a lack of time.

SED models were computed assuming a Salpeter IMF and an exponentially decaying SFH with PEGASE.2, these models were redshifted and passed through the used filters with LEPHARE. Following the models, the color selection employed was $I - H > 2.5$ and $R - I > 2$. This permitted to include the majority of $z \sim 6$ galaxies rejecting all the lower redshift interlopers galaxies modelled.

The total area studied was 250 $arcmin^2$ for RCS2 and 150 $arcmin^2$ for SDSS fields. The number of LBG candidates detected was 67 for RCS2 and 73 for SDSS, which led to an average of 0.35 $objects/arcmin^2$. However, as the redshift of the sources could not be well constrained and the foreground lenses distort the observed angles, the spatial density of i-band dropouts could not be easily determined.

Resumen

Este reporte presenta la búsqueda de galaxias “marginadas” (dropout galaxies) ($z \sim 6$) en la banda i ubicadas en torno a cúmulos de galaxias de primer plano detectados en las bases de datos RCS2 y SDSS, los cuales probablemente magnifican el brillo de las candidatas permitiendo un futuro estudio espectroscópico de alto S/N de estos objetos. Para cada uno de los 24 cúmulos estudiados (12 de cada base), dos imágenes en las bandas H e I fueron obtenidas. Además, para 10 cúmulos de RCS2, una imagen en la banda R fue también obtenida. La profundidad de las imágenes es 23.5, 24 y 24.4 mag_{AB} en las bandas H , I y R , respectivamente. Imágenes adicionales de HST en $F160W$, $F105W$, $F606W$ y $F390W$ fueron además obtenidas para 7 campos de los datos de SDSS, pero la fotometría de las candidatas detectadas en la banda H , no fue extraída de las imágenes de HST.

Los modelos SED fueron calculados usando una función de masa inicial (IMF) de Salpeter y una historia de formación estelar (SFH) que decae exponencialmente, usando PEGASE.2. Estos modelos fueron corridos al rojo y pasados a través de los filtros usados con LEPHARE. Siguiendo los modelos, la selección de color empleada fue $I - H > 2.5$ y $R - I > 2$. Esto permitió incluir la mayoría de $z \sim 6$ rechazando todas las galaxias modeladas contaminantes de menor redshift.

El área total estudiada fue de 250 $arcmin^2$ para RCS2 y de 150 $arcmin^2$ para SDSS. El número de candidatas a Lyman-break galaxies (LBG) detectadas fue de 67 para RCS2 y de 73 para SDSS, lo cual llevó a un promedio de 0.35 $objetos/arcmin^2$. Sin embargo, como el redshift de las fuentes no pudo ser bien acotado y los lentes de primer plano distorsionan los ángulos observados, la densidad espacial de las candidatas no pudo ser

bien determinada.

Contents

Abstract	iii
Abstract	v
1 Introduction	2
1.1 Looking further	3
1.2 Learning from high redshift galaxies	4
1.3 The Lyman break technique	6
2 Data	8
2.1 Detectors	8
2.1.1 FourStar	8
2.1.2 IMACS	9
2.1.3 HAWK-I	10
2.1.4 FORS2	10
2.1.5 2MASS and USNO surveys	11
2.2 Objects	16
2.2.1 The RCS2 Sample	16
2.2.2 The SDSS Sample	22
3 Reduction	24
3.1 FourStar <i>H</i> band images	24
3.1.1 Image sum	24

3.1.2	Dark subtraction	25
3.1.3	Non linearity correction	25
3.1.4	First sky subtraction	27
3.1.5	Masks construction	30
3.1.6	Second sky subtraction and image stacking	32
3.2	IMACS <i>I</i> band images	32
3.2.1	Flat and bias	33
3.2.2	Standard	34
3.3	Stack chip	34
4	Calibration and photometry	37
4.1	WCS	38
4.2	Zero point	42
4.3	Pixel matching and Photometry	47
4.3.1	Pixel matching (SWarp)	47
4.3.2	Photometry (SExtractor)	49
4.4	Detection Limit	51
4.4.1	Signal/Noise	52
4.4.2	Luminosity Function	52
4.4.3	Fake stars	52
4.5	Composite band	56
5	Model	59
5.1	Softwares employed	60
5.1.1	PEGASE.2	60
5.1.2	LePHARE	60
5.2	Models	62
5.2.1	Galaxies evolving with redshift	62
5.2.2	Galaxies of different ages for each redshift	64
5.2.3	Galaxy angular size	69
5.2.4	Stars	73

6 Results	75
6.1 Color Magnitude Diagrams	75
6.2 Candidates	79
6.2.1 RCS2 objects	79
6.2.2 SDSS objects	90
6.3 Correlation Function	106
A Geometry of a gravitational lens	109
B The metric of light deviation	114
B.1 Connection coefficients	114
B.2 Quasi-Minkowsky space	115
B.3 Schwarzschild metric	115
B.4 Light deviation	117
C Example of a asctoldac configuration file	118
D On the way Scamp can work	120
E WCS projection with FITS header	122
F Schechter function	125
G Auto-correlation Function	128
H Other points	130

Chapter 1

Introduction

Witrangé anay! Wunkey com pu che gni duam.

“Get up! The sun rises for everybody”

Cosmology, like magic has always been a difficult and great issue. In modern cosmology, scientist have to face an enormous degeneracy. The evolution of space and the evolution of visible matter. Matter and space are intrinsically linked but 0.4% of the matter is visible and from it, the nature of the whole universe must be derived.

All began with a simple argument of homogeneity and isotropy. Then, thanks to variable stars, in 1931, Hubble found that the universe was in expansion and he roughly determined its age: 10 Gyr. However, star specialists found stars older than 10 Gyr. Supernovas, lens statistics and CMB studies (Bennett et al 2013) found a better estimation of the age of the universe: 13.7 Gyr. Furthermore these studies constrained the present energy density of the universe to a value close to the critical density which seems to be more than a coincidence. Even though, the nature of dark energy and its density evolution as well as the existence of dark matter remain unexplained today.

Visible matter traces the gravitational field. It can be used to determine the shape of the universe and its evolution. It is thought necessary to know how visible matter intrinsically evolves in order to use it as a tracer. Consequently, the knowledge of galaxy properties and their evolution is an important tool in cosmology. Therefore, the mechanisms ruling the star formation in galaxies must be determined at low and high redshift.

The flux in the i band of $z \sim 6$ galaxies is dropping due to the Lyman absorption by neutral Hydrogen in the IGM (see Section 1.3): they are i-band dropouts. Previous studies were performed on $z \sim 6$ galaxies (Bouwens et al 2006, Dow-Hygelund et al 2007). The SFR density (ρSFR) was determined to be $\rho SFR = 0.0090 \pm 0.0031 M_{\odot} yr^{-1} Mpc^{-3}$ to $z_{AB} \sim 27$ or $\rho SFR = 0.036 \pm 0.012 M_{\odot} yr^{-1} Mpc^{-3}$ extrapolating (with a Schechter function) the luminosity function to the faint limit (Bouwens et al 2003). Furthermore, Overzier et al (2006) found the presence of clustering with 94% significance and a strong Balmer breaks in some i-band dropouts, indicative of stellar populations older than 100 Myr and with masses comparable to those of L^* galaxies at $z \sim 0$.

The current work aims to select galaxies at $z=6$ around foreground lensing galaxy clusters with the Lyman break technique. Hoping for a later high S/N spectroscopy, this study will permit to constrain the formation of primordial galaxies and the factors which rule the star formation.

Throughout this report, a Λ -dominated flat cosmology is assumed with $H_0 = 70 \text{ km s}^{-1} \text{ Mpc}^{-1}$, $\Omega_m = 0.3$, and $\Omega_{\Lambda} = 0.7$ (Komatsu et al. 2011). All magnitudes are on the AB system¹ (Oke & Gunn 1983). Coordinates are given in degree in J2000.

1.1 Looking further

High precision cosmology now requires to look father instead of extrapolating. For example, to calculate the parameters ruling the evolution of energy density, it is required to look at high redshift where the non-linear evolution becomes important. Moreover, to determine the evolution of structure, it is needed to study high redshift galaxies directly because they and their neighbourhood is completely different from local galaxies. Variable stars and supernovae are not bright enough any more for high redshift studies,

¹ $Mag_{AB} = -2.5 \log_{10} f_{\nu} - 48.60$ where f_{ν} is in $\frac{\text{ergs}}{\text{scmHz}}$. The magnitude zero-point corresponds to a spectral flux density of 3631 Jy (1 Jy = 1 Jansky = $10^{-26} \text{ WHz}^{-1} \text{ m}^{-2} = 10^{-23} \text{ ergs}^{-1} \text{ Hz}^{-1} \text{ cm}^{-2}$)

it is thought necessary to look at galaxies. Galaxies with a high star formation rate or an active nucleus, with today's large telescopes, are bright enough to look at redshift 6 (ie: 950 Myr after the big bang). Some studies were done using AGNs to constrain the density of neutral hydrogen in function of redshift (Hu et al 1995). Other studies use the absorption from the Lyman forest to detect high redshift galaxies. Galaxies detected by this method are called Lyman Break Galaxies (LBG) (Bouwens et al 2006). It is also possible to detect high redshift galaxies by their Lyman rest-frame emission peak because it is known that star forming galaxies are likely to have a $Ly\alpha$ emission peak (Curtis-Lake et al 2012). Therefore, 3 narrow band filters centred on the rest-frame $Ly\alpha$ wavelength permit to detect them. The Lyman break technique suppose that there is neutral hydrogen in the IGM around the source galaxy and the Lyman peak technique only detects star forming galaxies.

1.2 Learning from high redshift galaxies

Studies of high redshift galaxies permit to constrain:

- **The reionization period.** To detect $z=7,8$ galaxies, Henry et al 2007 used the Lyman break technique with a color selection of $J_{110} - H_{160} \geq 2.5$. They concluded that it is currently uncertain if the the amount of star formation at $z = 6$ is sufficient to reionize the universe. Therefore J-dropout LBGs may play an important role in this process, which is likely between $9 \leq z \leq 14$ ² The critical star formation rate density (ρSFR) required to ionize the universe at this epoch, is $\rho SFR(z = 9.5) = 0.09 M_{\odot} yr^{-1} Mpc^{-1}$ (Madau et al. 1999).
- **The evolution of structures.** The angular correlation function (ACF) is widely used in high redshift galaxy studies (Eyles et al 2005, Yan et al 2005). It is described in Appendix G. Basically, it aims to measure the clustering strength of an angular distribution of objects (here galaxies). The ACF, depending on the

²Before $z=14$ there were not enough sources to ionize the universe and after $z=6,7$ the universe is ionized yet because we can detect some Lyman- α radiation.

angular separation, can be written as a function of the covariant distance between galaxies at a given redshift (Kahikawa et al 2006). The ACF can be also derived with some conditions: for example, (Cooray et Ouchi 2006) derived the correlation function of $z \sim 4$ galaxies according to their luminosity. Furthermore, they derived the luminosity function according the local density of objects. This allowed them to determine the differences between the evolution of satellite galaxies and central ones.

- **The average star formation history (SFH) of the universe.** The rest-frame UV luminosity can be converted to SFR using the relation given in Kennicutt (1998).

$$SFR[M_{\odot}yr^{-1}] = 1.4 \times 10^{28} L\nu[ergs^{-1}Hz^{-1}]. \quad (1.1)$$

Where $L\nu$ is the average luminosity in the wavelength range 1500-2800 Å. This relation were obtained with a Salpeter (1955) IMF and a SFR constant over at least 10^8 years. The UV rest-frame luminosity must be determined for each galaxy and a luminosity function may be drawn up to the limit magnitude and then interpolated to faint luminosities. This procedure gives the expected total UV flux of selected sources. The SFR can also be scaled to other fluxes (Kennicutt 1998), but the UV flux, is the easiest to measure and therefore the most widely used. Measuring the SFR for many redshift bins permits to determine the history of star formation of the universe (Bouwens et al 2006).

- **The precursors of today's galaxies.** It is highly probable (thanks to the argument of homogeneity) that the surrounding galaxies used to look like high redshift galaxies 13 Gyrs ago: there is no reason to be in a peculiar region of the universe. The study of high redshift galaxy properties permits to explain the processes implied in the galaxy formation. To understand how a galaxy, our galaxy formed, it is necessary to know the SFR, metallicity, mass, accretion rate of early types galaxies. Information can be obtained by broad band analysis or by spectroscopy. With broad band images, luminosity functions can be obtained. They permit to get average properties of the selected galaxies. And with spectra, as high red-

shift galaxies are faint, spectroscopic studies are often performed by stacking the spectra of several galaxies (Shapley et al 2003, Lee et al 2011). Stacking spectra from different galaxies increases the signal to noise ratio and underlines some features: spectral line or color average. But these studies demonstrated that high redshift galaxies are very different from each other. They differ in their Lyman emission, UV-slope, extinction and it is believed that they differ in their SFR. And as stacked spectroscopy groups galaxies according to their flux in certain bands (typically the rest-frame UV band), this method cannot provide an accurate measure of the SFR according to the galaxy mass (Lee et al 2011). High redshift galaxies appear very faint: they are often studied statistically. Therefore, some additional studies of individual high redshift galaxy SED are required. It is thought necessary to find a very bright high redshift galaxy. Intermediate redshift ($z \sim 0.5$) galaxy clusters sometimes provide a high gravitational magnification of background sources up to a factor 40. Some high redshift galaxies magnified by a foreground galaxy cluster were already found (Koeser et al 2010, Smail et al 2006, Morisson et al 2012). These studies permit to determine the intrinsic properties of some high redshift galaxies. Nowadays, more and more high redshift galaxies are detected through gravitational lenses. Nearly 20 have been detected so far.

1.3 The Lyman break technique

The Lyman Break technique was first described in (Steidel & al 1992) and utilized in (Steidel & al 1995). In the later paper, the author is using AB magnitude system, claiming that “a galaxy with a smooth spectral energy distribution of the form $F\nu \propto \nu^\alpha \propto \lambda^{-\alpha}$ will have equal $U - G$ and $G - R$ colours in the absence of line blanketing.” Where $F\nu$ is the flux, ν the frequency, λ the wavelength and α a parameter.

Indeed, for such a galaxy:

$$\begin{aligned}
 U - G &= -2.5 \times (\log(F_\nu(\lambda_u)) - \log(F_\nu(\lambda_g))) \\
 &= -2.5 \times (\log(K \times \lambda_u^{-\alpha}) - \log(K \times \lambda_g^{-\alpha})) \\
 &= -2.5 \alpha \times (K \times [\log(\lambda_u) - \log(\lambda_g)]) \\
 G - R &= -2.5 \alpha \times (K \times [\log(\lambda_g) - \log(\lambda_r)])
 \end{aligned}$$

Where we used $F_\nu(\lambda) = K \times \lambda^{-\alpha}$ and λ_u, λ_g and λ_r equal 365 nm, 490 nm and 660 nm respectively. So, as $\log(\lambda_u) - \log(\lambda_g) = -0.12$ and $\log(\lambda_g) - \log(\lambda_r) = -0.13$,³ $U - G = G - R$ to a close approximation for this galaxy. However, using (Madau et al. 1995) models for IGM absorption and (Bruzual et Charlot 1993) for SED in the restframe, Steidel noticed that the $U - G$ colour drops very fast with redshift after redshift $z=3$ whereas $G - R$ doesn't.

The model of absorption of Madau consisted only of neutral hydrogen, so this feature is due to Lyman absorption and the first detections were made on $z \sim 3$ AGN in (Madau et al 1995). This technique was then employed to detect high redshift galaxies. As initially described by Steidel, the technique utilized 3 bands around the rest frame Lyman break and comparing the blue slope of the SED against its red slope. Meanwhile, one can use only 2 bands, one on each side of the rest frame Lyman break (1215 Å), and look for very red colour representing the Lyman absorption by neutral hydrogen of the IGM.

Note that the Lyman break technique can only be utilized if there is some neutral Hydrogen in the surrounding IGM of the galaxy. The drawback of this method employing only few filters is that one cannot accurately estimate the contamination rate. The main contaminants are galaxies with a strong Balmer break between the two filters: $z=2$ elliptical galaxies.

³Considering $\lambda_U, \lambda_G, \lambda_R = 370, 490$ and 660 nm and that the filters transmission curves have the same shape in a log plot.

Chapter 2

Data

Iñey no rume kimlay cheu amutual kimnolu cheu ñi, ñi kupalme.

“No one can know where he wants to go, if he does not know where he comes from.”

In this chapter, the four instruments utilised during this work and the observed objects are described. All the observations were performed in Chile between 2011 and 2012.

2.1 Detectors

2.1.1 FourStar

FourStar¹ is an infrared camera installed on the Baade 6.5m telescope, one of the two Magellan telescopes in Las Campanas Observatory. The camera has 4 Teledyne HAWAII-2RG detectors of $2k \times 2k$ pixels each. and it covers the J, H, K_s bands in a 10.8' x 10.8' field of view.

The observations of the RCS2² objects in the H band were obtained with FourStar on the 04th and 05th of September 2011. The seeing in the H band was 0.6 and 0.7 arcsec respectively during the 04th and 05th of September. The moon was in its first

¹FourStar manual is available at <http://instrumentation.obs.carnegiescience.edu/FourStar/FOURSTAR.html>

²see section 2.2.1

quarter. Each object was integrated for a total of about 1h. Each individual exposure was of 11.64 sec, and 8 exposures were taken between each offset. The integration time is limited by the high sky level in the H band. For 11s of integration, the sky level was around 20,000 ADU (the saturation limit is 50,000 ADU). About 40 offsets were taken for each field. The fields are described in section 2.2.

FourStar dataset consists of 8 exposures \times 40 offsets \times 4 chips \times 13 clusters = 16640 frames and around a total of 13h of science exposure.

2.1.2 IMACS

The Inamori Magellan Areal Camera and Spectrograph (IMACS³) is an image and spectroscopy optical camera also installed on the Baade telescope. The camera is composed of 8 chips of 4k \times 2k pixels procuring the equivalent of a 8k \times 8k CCD mosaic. IMACS covers the B , V , and I bands and has two different focal ratios. The f/4 mode provides a FOV of 15.4 \times 15.4 arcmin with a scale factor of 0.111 arcsec per pixel. The other mode, called f/2, has an actual focal ratio of f/2.5, corresponding to a scale factor of 0.200 arcsec per pixel. As the targets are distributed within few arcminutes around the RCS2 cluster centers, a better pixel resolution was preferred over a larger FOV, leading to the decision to operate in the f/4 configuration of IMACS.

The observations of the RCS2 objects in the I band were obtained with IMACS on the 30th of September 2012. The seeing during this night was 0.8 arcsec in this band and the moon in its full phase. These data overlapped with the data previously taken in I band. The read out time of the camera is of about 2 min. Consequently, it is preferable to take the longest exposures possible. It was decided to employ a 5 minutes integration times. Although the sky level was only 13,000 ADU (the detector saturates at 60,000), the bright stars began to saturate. Usually, 3 or 4 exposures were made per object and more for the last object which is alone at a right ascension interval of about 2h. This object, RCS2-0310_2399, was integrated for about a hour.

³ IMACS manual is available at <http://www.lco.cl/telescopes-information/magellan/instruments/imacs/user-manual/the-imacs-user-manual>

IMACS dataset consists of $4 \text{ offsets} \times 8 \text{ chips} \times 13 \text{ clusters} = 416$ frames for a total exposure of 6h.

2.1.3 HAWK-I

The High Acuity Wide-Field K-band Imager (HAWK-I⁴) is a NIR ($0.85 - 2.5\mu\text{m}$) wide-field imager. It is installed at the Nasmyth A focus of 8m UT4 of the VLT telescopes in the Paranal Observatory. HAWK-I was installed in 2007⁵. It covers the Y , J , H & K filters with a FOV of $7.5' \times 7.5'$ covered by the mosaic of four Hawaii-2RG chips separated by $15''$. The pixel scale is $0.1064''/\text{pixel}$.

Observations in IR are only performed by night because the star guider camera is an optical camera and cannot follow the guide star by day. Furthermore, by day atmospheric turbulences are higher. However, the sky IR background is as high at night as at day due to the thermal emission.

The observations of the SDSS⁶ objects in the H band were obtained with HAWK-I in queue mode from May 2011 to May 2012. The log of observation is given in Table 2.1. The integration time was set to 10 sec and 12 exposures were taken for each offset. These exposures were automatically combined and the four chip images were gathered in the same cube. This ESO procedure reduces the size of the raw data by a factor of 12. The total integration time is 48 min for every object.

HAWK-I dataset consists of $23 \text{ offsets} \times 4 \text{ chips} \times 13 \text{ clusters} = 1196$ frames for a total exposure of 10h.

2.1.4 FORS2

The FOcal Reducer/low dispersion Spectrograph 2 (FORS2⁷) is a very versatile optical instrument mounted on the Cassegrain focus of the 8m UT1 VLT telescope. It can be used for imaging, polarimetry, long slit and multi-object spectroscopy. It covers the

⁴ HAWK-I manual is available at <http://www.eso.org/sci/facilities/paranal/instruments/hawki/>

⁵ see <http://www.eso.org/public/news/eso0736/> for the press release.

⁶ see section 2.2.2

⁷ FORS2 manual is available at <http://www.eso.org/sci/facilities/paranal/instruments/fors/overview.html>

U , B , V , R , I & z bands and has two plate scales available: 0.250 "/pixel and 0.125 "/pixel. The lowest one: 0.125"/pixel was utilized. The camera system can operate with two 2 chips of $2k \times 4k$ pixels E2V CCDs⁸, but most of the time, FORS2 works with 2 chips of $2k \times 4k$ pixels MIT CCDs⁹.

The observations of the SDSS objects in the I band were obtained with FORS2 in queue mode from April 2011 to January 2012. The log of observations is given in Table 2.1. It was decided to use the red sensitive camera configuration (with the MIT CCD), because it is more sensitive for wavelengths longer than 620 nm. 30 and 12 dithered images were taken for the object SDSSJ1152+09 and all the other (11) objects respectively. All the images were integrated for 2 minutes.

Note that there was always fewer exposures for optical data than for the NIR data. This is because the thermal emission of the sky is so high in IR that exposures must be very short (of the order of 10s). Furthermore, the read out time in optical is always longer. So contrary to IR observations, a large exposure time is highly recommended in optical.

FORS2 dataset consists of 25 images x 2 chips x 13 clusters = 312 frames for a total exposure of 11h.

2.1.5 2MASS and USNO surveys

To calibrate the astrometry and photometry of the images (Chapter 4), some reference catalogues were utilized. 2MASS, an IR catalogue was employed to calibrate the H band images and USNO-B1 an optical catalogue was employed to calibrate the I and R band images.

⁸ E2V is the name of the company which created these CCD. The E2V CCDs provide much higher response in the blue and UV wavelength range below 600 nm, but suffer from strong fringing above 650 nm.

⁹ The MIT CCDs provide much higher response in the red wavelength range beyond 650nm, with impressively low fringe amplitudes. The response in the UV below 400nm drops however significantly

Object	HAWK-I day	Time	FORS2 day	Time
SDSSJ1002+20	2011-05-14	01h24m06	2011-04-20	23h45m52
SDSSJ1028+13	2012-05-13	01h09m01	2011-04-02	02h50m53
SDSSJ1050+00	2012-05-16	00h35m50	2011-04-02	02h16m11
SDSSJ1113+23	2012-05-16	23h52m32	2011-05-02	00h16m12
SDSSJ1152+09	2012-05-16	02h28m51	2012-01-17	08h29m28
SDSSJ1329+22	2012-05-18	02h19m15	2011-05-02	05h03m43
SDSSJ1336-03	2012-05-10	05h37m32	2011-05-02	06h44m53
SDSSJ1514+22	2011-08-07	00h27m36	2011-05-02	07h17m23
SDSSJ1604+22	2011-08-02	00h39m43	2011-05-02	07h50m29
SDSSJ1621+06	2011-06-30	06h03m35	2011-06-26	05h12m31
SDSSJ1622+10	2011-08-07	01h23m24	2011-05-02	08h24m00
SDSSJ2111-01	2011-06-12	08h26m57	2011-06-25	06h38m16

Table 2.1: The log observation of the SDSS objects. In column 1: the name of the cluster; column 2: the day of observation with HAWK-I (in year-month-day); column 3: the time of the beginning of the observation with HAWK-I; column 4 and 5: same as column 2 and 3 but for the observations with FORS2 camera.

Camera	FourStar	IMACS	HAWK-I	FORS2
FOV	10.8' × 10.8'	15.4'	7.5'	4.25' x 4.25'
Plate Scale	0.159"/pixel	0.111"/pixel	0.1064"/pixel	0.125"/pixel
Wavelength Coverage	1-2.5 μm	3900-10500 \AA	0.85-2.5 μm	330-1100 nm
Filter used	H	CTIO-I	H	I_BESS+77
Filter's Wavelength	1.62 \pm 0.15 μm	800 \pm 80 nm	1.62 \pm 0.15 μm	770 \pm 70 nm

Table 2.2: The basic characteristics of the used camera.

2MASS

The two micron all sky survey (2MASS¹⁰; (M.F. Skrutskie & al 2006) is a homogeneous whole sky survey in 3 infrared bands: J (1.25 μm), H (1.65 μm), and K_s (2.17 μm).

¹⁰ The 2MASS project is funding by the National Aeronautics and Space Administration (NASA) and the National Science Foundation (NSF). More information at: <http://www.ipac.caltech.edu/2mass/>

It was done 30 years after the previous infrared sky survey: Two Micron Sky Survey (TMSS; Neugebauer & Leighton 1969). 2MASS used two highly-automated 1.3-m telescopes, one at Mt. Hopkins (USA) and one at CTIO (Chile). Each telescope was equipped with a three-channel camera, each channel corresponded to a IR band and it consisted of a 256×256 array of HgCdTe detectors. The Infrared Processing and Analysis Center (IPAC) reduced the data. The magnitude limits for point sources are 15.8, 15.1 & 14.3 in the J , H & Ks bands respectively. The photometric and astrometric errors are 0.1 mag (10%) and 0.5" respectively. The magnitude were given by reference to Vega (ie: in the Vega system).

USNO-B1

The United States Naval Observatory (USNO¹¹, Monet & al 2003) is a whole sky catalogue in 5 optical bands. Objects of the catalogue were derived from 3,643,201,733 separate observations. The data were obtained from scans of 7,435 Schmidt plates taken for the various sky surveys during 50 years. The mean time of the observation is around 1975. The FOV of the plates is 20×10 *arcmin*².

USNO-B1 measured fluxes from Schmidt plates utilizing the Precision Measurement Machine (or PMM). 588 different exposures of 1312×1032 pixels with a pixel scale of 0.9 "/pixel were taken for each plate. The reduction of each exposure was performed in real time and then utilized to calibrate the next exposures (background compensation, distance from the plate to the CCD and focal distance).

The astrometry were calculated employing SLALIB (Wallace 1994) reference objects. The center of each object on the image was obtained with a fit of its profile assuming the circular profile shape of the Equation 2.1.

$$T(x, y) = B + \frac{A}{e^{\alpha(r^2 - r_0^2)} + 1} \quad (2.1)$$

Where $r^2 = (x - x_0)^2 + (y - y_0)^2$. The six free parameters are A (central amplitude), B (background), x_0 , y_0 (position), r_0^2 (saturation radius), and α (extent of image wings).

¹¹ <http://tdc-www.harvard.edu/catalogs/ub1.html>

Then, the detected centers were matched to the reference position in SLALIB with a least fit square method assuming a cubic image distortion. The astrometric error is around 0.2 arcsec at J2000

The photometry were calibrated with two references: the Guide Star Photometric Catalog 2 (Bucciarelli & al 2001) and the USNOFS CCD parallax program (Monet & al 1992). The photometric calibration lied only on faint stars, with magnitude between 14 and 22 in the Vega system. While 44% of the images could be calibrated directly with the reference catalogues, the other 56% were calibrated with other frames overlap zones. The solution combining all 632,827 calibration stars spread over 3,281 plates has a standard deviation of 0.25 magnitudes. The photometry of non-stellar objects is not reliable.

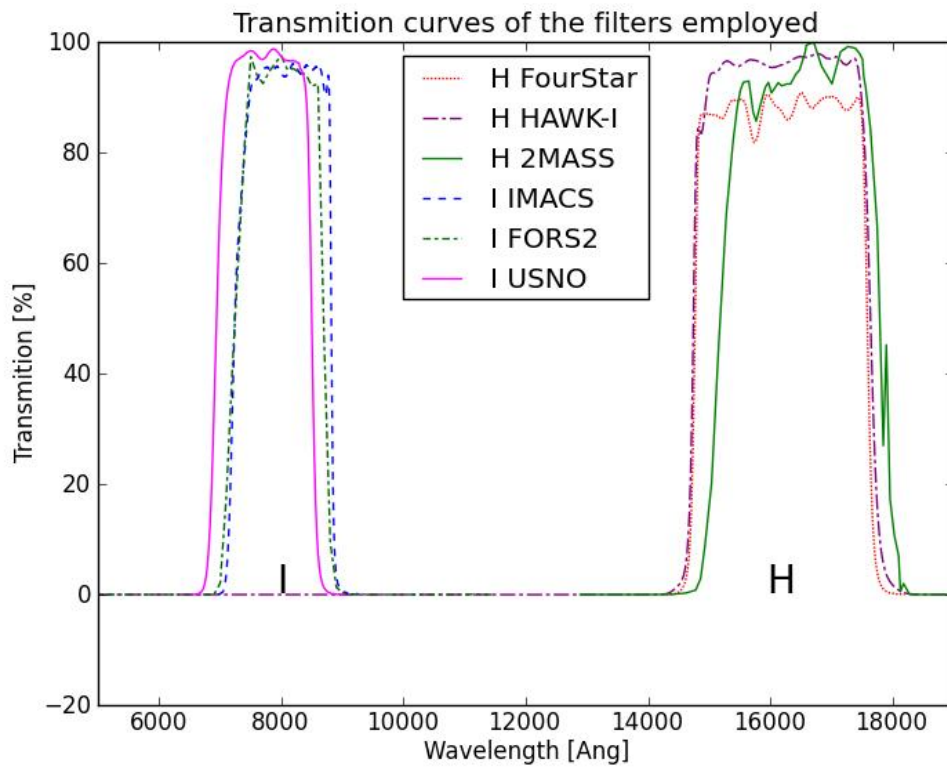


Figure 2.1: Transmission curves of the bands occupied throughout the work. 2MASS and USNO are surveys used for a reference ZPT in Section 4.2

2.2 Objects

The observed fields were around 24 galaxy clusters which are known to be strong gravitational lenses due to the presence of elongated arcs around them. These lenses have been previously discovered either from the RCS2 or from the SDSS (or both). The sky position of these clusters is shown in Figure 2.2.

2.2.1 The RCS2 Sample

The Red-sequence Cluster Survey 2 (RCS2¹², Gladders & Yee, 2000) is a 1000 square degrees multi-color imaging survey utilizing the square-degree imager MegaCam, on the 3.6m Canada-France-Hawaii Telescope (CFHT). The objective of the survey is to detect galaxy clusters over the redshift range $0.1 \leq z \leq 1$. This enables the study of galaxy clusters and their distribution. It also procures a catalog of strong gravitational lenses which provides a magnified window to the far universe. Furthermore, a survey of this size and quality is required to probe Dark Energy and measure its state equation parameter $w = P/\epsilon$ with an accuracy of 0.1, where P is the pressure and ϵ is the energy density.

The basic idea of the red sequence technique employed in the RCS is to select red galaxies belonging to a main sequence¹³ in the color-magnitude (R' vs $R' - z'$) diagram (Gladders & Yee, 2000). The RCS targets group of galaxies which are close spatially and aligned in the color-magnitude diagram (CMD). The selected galaxies are expected to be elliptical galaxies of the same redshift, so they are likely to belong to the same galaxy cluster. Elliptical galaxies are expected to be gathered at the center of the clusters and are brighter. Therefore an over-density of elliptical galaxies is easier to detect and likely to traces galaxy cluster. Figure 2.3 shows an illustration of the red sequence technique on a theoretical CMD.

RCS originally used only the CFHT images but later, these were combined with the Spitzer, VLT and Magellan observations. About 20 researchers are involved in this

¹²<http://www.astro.utoronto.ca/gilbank/RCS2/>

¹³

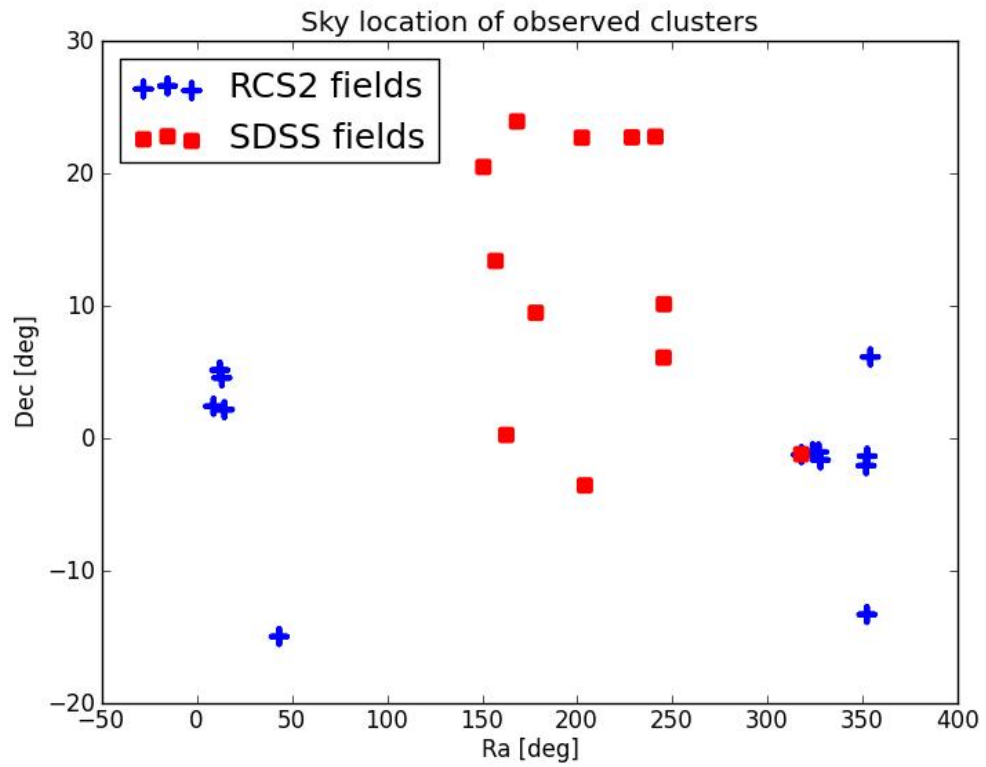


Figure 2.2: Sky position of the galaxy clusters observed. The RCS2 objects are represented by a blue cross and the SDSS objects by a red square. The object at $ra, dec \sim 317.8, -1.2$ is present in both RCS2 (RCS2-2111.21.18) and SDSS (SDSSJ2111-01) dataset.

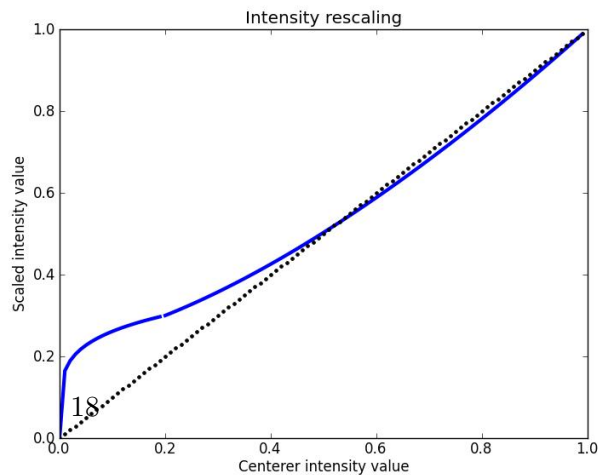
project. Additional observations are planned for the RCS in the future (X-ray, radio and spectroscopy). This project is now far from being only bi-chromatic as the perceptive reader may notice. The data from CFHT come from a wide survey aimed to find galaxy clusters (with the red sequence technique). The images presented in section 2.1 are focused on some of these clusters, therefore they are naturally much deeper than images provided by other surveys (from CFHT or Spitzer). Consequently, the survey images are disregarded and only the previously presented images are utilized throughout this work.

The RGB images of the objects of the RCS2 are showed in Figure 2.4 within a FOV of $1 \times 1 \text{ arcmin}^2$. The red, green and blue color correspond to the H , I and R bands respectively. Before merging the H , I and R band images in a RGB frame, each image was rescaled with a sigma clipping and linear transformation method in Equation 2.2.

$$\begin{aligned}
 Centered &= \frac{\frac{Image - Median(Image)}{RMS(Image)} - cmin}{cmax - cmin} \\
 Scaled &= Scale(Centered) \\
 Cutted &= \begin{cases} 0 & \text{if } (Scaled < 0) \\ Centered & \text{if } (0 < Scaled < 1) \\ 1 & \text{if } (Scaled > 1) \end{cases} \\
 RGB &= Cutted * 255
 \end{aligned} \tag{2.2}$$

Where Median and RMS are the median and the Root-Median-Square of the images in the region selected to create the RGB image. The regions are squares of 1 arcmin around the cluster center (visually estimated). Scale is an increasing bijection of the segment 0-1 represented in Figure 2.5. Cmin and cmax are user defined

Figure 2.5: The function used to rescale the intensity of the image



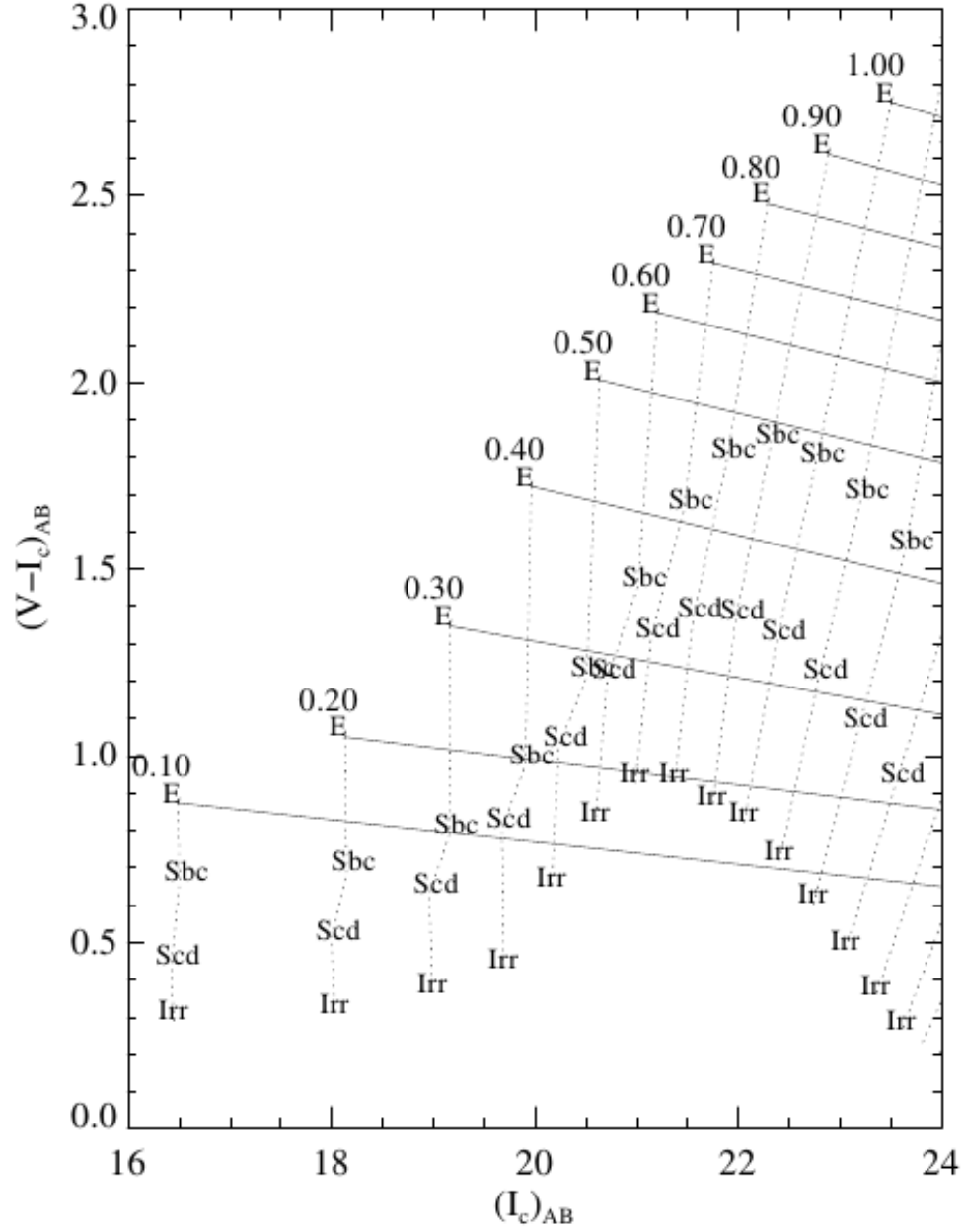


Figure 2.3: Theoretical galaxy color-magnitude diagram from (Gladders & Yee, 2000). The dotted lines connect galaxies of different type but with the same luminosity ($M_I = -22$) at the same redshift. Solid near-horizontal lines show the expected slope of the red sequence (i. e. the sequence of elliptical galaxies belonging to the same redshift).

Object	RA [deg]	Dec [deg]	H [mag]	I [mag]	R [mag]
RCS2-0047_0.95	14.365	2.157	23.5	23.9	24.6
RCS2-0047_18.79	13.043	4.559	23.1	23.7	26.7
RCS2-0047_2527	11.963	5.139	23.2	23.5	25.7
RCS2-0047_4381	8.617	2.423	23.2	24.2	24.7
RCS2-0310_2399	43.174	-14.992	23.1	24.6	N/A
RCS2-2111_21.18	317.831	-1.239	22.9	23.6	25.1
RCS2-2143_21.58	323.802	-1.048	23.1	23.6	24.4
RCS2-2143_21.79	326.904	-1.045	23.2	23.3	23.7
RCS2-2143_21.85	327.856	-1.648	23.3	23.5	23.6
RCS2-2327_0204	351.865	-2.075	23.3	23.7	N/A
RCS2-2329_5295	352.449	-1.347	23.3	23.9	N/A
RCS2-2338_23.48	352.290	-13.296	23.3	23.9	25.3
RCS2-2338_23.60	354.090	-6.140	23.3	23.8	24.5
SDSSJ1002+20	150.577	20.480	23.3	24.0	N/A
SDSSJ1028+13	156.984	13.384	23.3	24.5	N/A
SDSSJ1050+00	162.631	0.247	23.3	24.5	N/A
SDSSJ1113+23	168.267	23.910	23.3	23.6	N/A
SDSSJ1152+09	178.162	9.466	23.5	24.3	N/A
SDSSJ1329+22	202.364	0.226	23.2	24.3	N/A
SDSSJ1336-03	203.965	-3.562	23.5	24.1	N/A
SDSSJ1514+22	228.673	22.714	23.0	24.2	N/A
SDSSJ1604+22	241.065	22.763	23.3	23.5	N/A
SDSSJ1621+06	245.354	6.089	23.4	24.2	N/A
SDSSJ1622+10	245.535	10.120	23.2	23.7	N/A
SDSSJ2111-01	317.798	-1.207	23.3	24.7	N/A

Table 2.3: The clusters observed throughout this work. In column 1: the clusters name; column 2 and 3: the Right Ascension and Declination of their WCS position respectively; column 4,5,6: the detection magnitude limit of the images in the H , I and R band respectively. These limits are calculated for a completeness of 80% of the objects detected. The objects are simulated sources with Gaussian profile of the same FWHM as the FWHM of the stars present on the image. The ZPT of the images is given in Section 4.2. There are fields without image in the R band, for which a N/A is displayed.

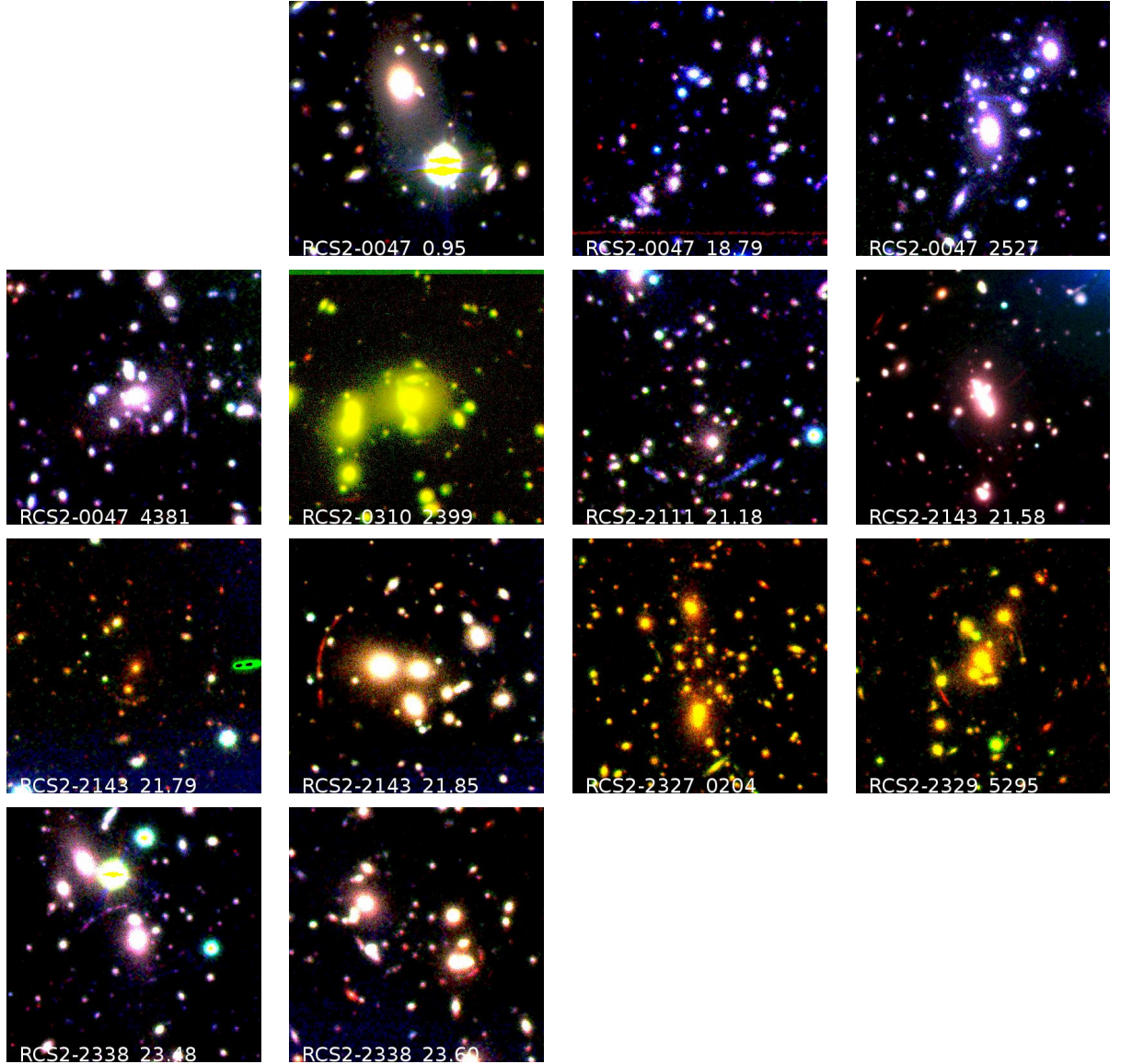


Figure 2.4: Color images of RCS2 clusters used in this study. The FOV is a square with a 1 arcmin large side. These Red,Blue,Green composite images are made with respectively the H , I , R band images. But RCS2-0310_2399, RCS2-2327_0204 and RCS2-2329_5295 have no R image. So it has no blue color in its RBG image.

values. For these color images, c_{\max} ranges between 20 and 5 and c_{\min} was set to 0.7. This means that we considered a color scale between 0.7 RMS and 20 RMS around the median. For example: if the value of the fits pixel is superior to $20 \text{ RMS} + \text{median}$, the color pixel has the maximum brightness and if the fits pixel is inferior to $0.7 \text{ RMS} + \text{median}$, the pixel is black. With $c_{\max} = 20$, the images are darker than with $c_{\max} = 5$ but we can see better the bright regions because they are not saturated any more. This procedure was established in order to get the same color scale estimation for the images of each band.

2.2.2 The SDSS Sample

The Sloan Digital Sky Survey (SDSS¹⁴, York & al 2000) is a multi-filter imaging and spectroscopic redshift survey named after the Alfred P. Sloan Foundation. SDSS is composed of three different surveys corresponding to different epochs : (SDSS-I, 2000-2005; SDSS-II, 2005-2008; SDSS-III, 2011-2014). It has made the largest sky color image ever made. This survey is using a dedicated 2.5-m wide-angle optical telescope at Apache Point Observatory. It takes images in 5 optical photometric bands (u, g, r, i and z). The telescope camera¹⁵ is made up of thirty CCD chips, each one contains 2048×2048 pixels. The CCD are arranged in six columns of five chips. Each column is encased in a vacuum-sealed chamber. In each row, an image is taken for 5 bands: one per chip. As the earth rotates and the telescope is parked in a given position, the objects fall successively on each filter (of the same column). Multiple observations of a given area are needed to fill the gaps between the CCDs.

The SDSS “new survey for giant arcs” Sample consists of strong lensing clusters which were identified in gband imaging of the most massive ~ 200 clusters selected by the red sequence from the SDSS photometry (Hennawi et al. 2008).

¹⁴<http://www.sdss.org/>

¹⁵<http://cas.sdss.org/dr4/en/sdss/instruments/instruments.asp>

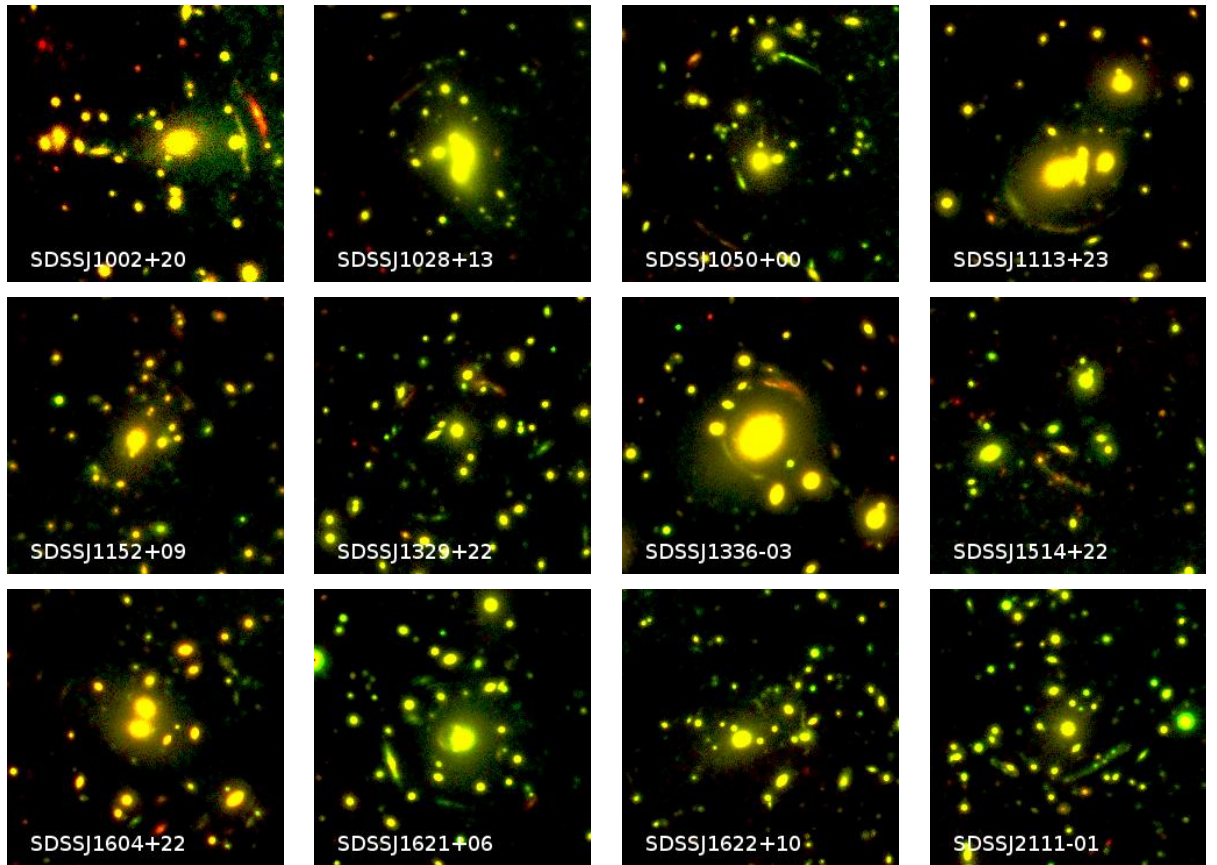


Figure 2.6: Color images of SDSS clusters. H is red and I is blue. Color scale and FOV (1 arcmin = 238 pixels) is same as Figure 2.4

The objects identified in the SDSS and utilized during this work are clusters visually selected as strong gravitational lenses due to the presence of arcs around them (Bayliss 2011).

Chapter 3

Reduction

Wuni femngei ta kuyen; Kuyen ta tripantu

“Just as today dawns, so the rest of the month will follow; and just as the first month,
so will be the rest of the year”

The reduction of FourStar and IMACS images were carried out with IRAF¹. The other dataset: HAWK-I and FORS2 images were reduced with ESO pipelines and its reduction will not be described in this work. IR reduction is generally more complex due to the high sky background. However, as only NIR images were processed, the principles of reduction were similar to the optical reduction steps.

3.1 FourStar *H* band images

3.1.1 Image sum

As a first step, an average of the individual exposures was made with the same offset (i. e., dither) thanks to the IRAF task “imcombine”. For the field objects, 8 equal exposures (with the same offset) were averaged without rejection. Each raw exposure had a name like: `fsr_1241_05_c1.fits`. Where `fsr` stands for “FourStar”, 1241 the name of

¹ IRAF (Image Reduction and Analysis Facility) is distributed by the National Optical Astronomy Observatories, which are operated by AURA, Inc., under cooperative agreement with the National Science Foundation.

the offset, 05 the (chronological) number of the exposure within this offset and c1 means this is the chip 1 (on a CCD of 4 chips). For each offset, a single image were generated reducing the number of images by a factor 8 (science frames) or 20 (dark frames). For example, all the `fsr_1241_i.c1.fits` (for `i` from 01 to 08) were averaged to create a single `fsr_1241_c1.fits`.

`fsr_1241_i.c1.fits -> fsr_1241_c1.fits`

3.1.2 Dark subtraction

Dark exposures were obtained in order to characterize the quantum noise of the detector and the read out noise. A dark exposure can be obtained closing the telescope or only the camera shutter and exposing while it is closed. It was done during the twilight with the same conditions as for the observations (exposure time and camera temperature). The dark subtraction has been done using IRAF routine “`imexpr`”. A master dark of the same exposure as the science image exposure (11.64s) were subtracted to every frame (science and calibration frames, see Equation 3.1).

$$\begin{aligned} raw - master_dark &= dark_corrected \\ cl > imexpr \text{ “}a - b\text{” } dark_corrected \text{ raw } master_dark \end{aligned} \tag{3.1}$$

This master dark was an average of 20 darks. The exposure times were short because of the high sky background (20,000 ADU in our case) in *H* band.

`fsr_1241_c1.fits -> dk_fsr_1241_c1.fits`

3.1.3 Non linearity correction

In IR arrays as in CCD detectors, the photons excite some electrons from their ground state. These electrons have then an energy enough to travel on the semi-conductor as on a conductor. Some electric fields block the electrons in their native pixel preventing it from jumping chaotically from one pixel to an other. These electric fields are always strong enough because the filters occupied prevent high energy photons from reaching the detector which would generate a super-excited electron able to cross the electrical border (between two pixel). However, when many electrons are trapped in the potential

well of a pixel, they electrically repel each other. Therefore, one of them can encounter a hole in the semiconductor (i. e., a position on the crystal that is positively charged). This electron may, enter the hole emitting a photon. This is exactly the same mechanism of the detection but in the other direction. It is popularly called “emission” it may also be called “crystal’s electron recombination due to the electric pressure of his brothers”. Recombination is more likely in IR than in optical detector due to the reading mode of the IR arrays : the reading is made behind the semiconductor in IR arrays (Joyce & al 1992). The unbound electrons must thought cross all the semiconductor thickness before being read out and the semiconductor cannot be made arbitrary thick because it would be thick to light.

The obvious problem of recombination is that the recombined electron is missing during the lecture of the detector charge and so the photon flux is underestimated, underestimation for which the non-linearity factor aims to correct. It is called “non-linearity” because this factor increases with the number of electrons read. This factor can be obtained from the FourStar instrument manual. As the linearity correction factor is a function of the intensity in ADU, the FourStar team provides the result with a polygonal fit (Equation 3.2).

$$exptime = A[0] \times raw + A[1] \times raw^{2.5} + A[2] \quad (3.2)$$

Where *exptime* is the exposure time scalar (in seconds) and *raw* is the flat field image measured in order to estimate the linear correction factors. $A[0]$, $A[1]$, $A[2]$ are scalar parameters estimated by a least square method over a range of exposure with the same dome illumination but different exposure times. Each parameter of the fit is specific to one pixel because it depends on the microscopic geometry of the pixel. Therefore these coefficients are given in the form of images. The linear correction method cannot be easier but may be, in the future, more accurate (i. e., more parameters on the polygonal fit). Equation 3.2 shows that : $A[0]$ is a linear coefficient, proportional to flat illumination and to the inverse linear gain of the pixel in units of [s/ADU], it represents the pixel linear response, the flat correction; $A[1]$ is a non-linearity factor and $A[2]$ is a constant term, representing the read out noise. FourStar team provides a cube of 3

images: $A[0], A[1]/A[0]$ and $A[2]/A[0]$. Note that the two last terms are independent from the flat field luminosity. Non-linearity were corrected employing FourStar non-linearity parameter images and IRAF “imexpr” routine (Equation 3.3).

$$\begin{aligned} \text{Truecounts} &= \text{exptime}/A[0] = \text{raw} + A[1]/A[0] * \text{raw} * *2.5 + A[2]/A[0] \\ \text{cl} > \text{imexpr} & \text{“}a * (1 + a * b * \text{sqrt}(\text{abs}(a)))\text{” } \text{lc_dk_imagedk_imagedlc_??_?}[* , * , 2] \end{aligned} \quad (3.3)$$

Where the last string is the expected non-linearity image $A[1]/A[0]$. As the bias and flat corrections were not performed², the $A[2]/A[0]$ and $A[0]$ terms were not considered. In the last image name, lc means linear correction, “??” represents the gain mode FullWell (fw) or LoNoise³ (for low noise [lo]) which can be read out from the image header. For the images reduced, the gain mode was FullWell. Finally, “?” refers to the chip, it takes values from 1 to 4. These linear correction images can be downloaded from FourStar website⁴. A typical input was `dk_fsr_1241_c1.fits`, the corresponding linear correction image was `lc_fw_1.fits[* , * , 2]` and its output was called `lc_dk_fsr_1241_c1.fits`.

`dk_fsr_1241_c1.fits -> lc_dk_fsr_1241_c1.fits`

3.1.4 First sky subtraction

In NIR bands, a careful estimation of the sky background is indispensable. A first sky subtraction was made to the images. The quality of this sky subtraction was bad as explained below. It still made possible to see some stars which were previously hidden in the background. The sky is subtracted from each image in the following way:

1. Combine⁵ the 6 images closest in time and having an offset from the current image

²The bias correction was neglected and the dark correction was previously performed. And the sky subtraction is corrected from the pixel response so the flat correction was not performed either.

³ FourStar has two different gain modes: FullWell and LoNoise (means low noise). FullWell has a gain of 2.59 [e-/ADU] and a RON of 21 electrons (e-). It is the default mode and is recommended for high background in broad-band and median-band filters. Because it has a higher dynamic range. LoNoise has a gain of 1.35 [e-/ADU] and a RON of 16 electrons. It is less noisy and recommended for narrow-band filters where the background count rate is low. For more information about the gain modes: http://www.mirametrics.com/tech_note_ccdgain.htm

⁴ <http://instrumentation.obs.carnegiescience.edu/FourStar/calibration.html>

⁵The combination is an average using a 3 sigma rejection and masking bad pixels (which is very important for the following work). 1 high and 1 low value pixels maximum could be rejected.

- to create the sky image corresponding to the current image.
2. Obtain the sky value for the sky image and the current image. This value is the median of the image masking the objects above 3 sigma. It is setted utilizing “imstat” routine with a maximum of 20 iterations.
 3. Normalise the sky image: divide it by its sky value and then multiply it by the current image sky value. Next, subtract the normalised sky image to the current image. This task is performed utilizing the “imarith” routine.

In other words, the combination of the nearest images in time were subtracted to the current image. For example, the pixel (200,312) of the image taken at 2h35 were subtracted by the pixel (200,312) of the combination of the images taken between 2h30 and 2h40 excluding the current image (2h35), because this combination represents the sky value at this pixel and at this time. An illustration of this method is given in Figure 3.1. Indeed, the sky value was calculated at a distance of the order of the dither distance from the current pixel and at a moment of the order of 5 minutes around the time of the current frame.

With this sky subtraction method, in addition to the sky value, the pixel response was corrected. Even if this estimation may be done before with the flat correction⁶, this sky subtraction can minimise some residual calibration errors. Actually, in this work, the flat correction was not performed considering that the sky subtraction procedure is properly rectifying the non-homogeneous pixel response.

Usually, the sky background is calculated on the same image, at a certain distance from the star. In this work, a new simple but precise method is employed. Considering the same pixel on different images, this method is faster, considers each pixel as unique (which is true) and, using more than one image for the sky estimation, it relies on more information. The only drawback is the need of reasonable dithers (see below). Anyway, dithers are usually established small enough to permit a wide area with the maximum weight map (i. e., to have a large sky area common in all the frames). This method works because the IR sky background, mainly thermal, can be considered as constant

⁶ remember that the bias can be neglected in IR

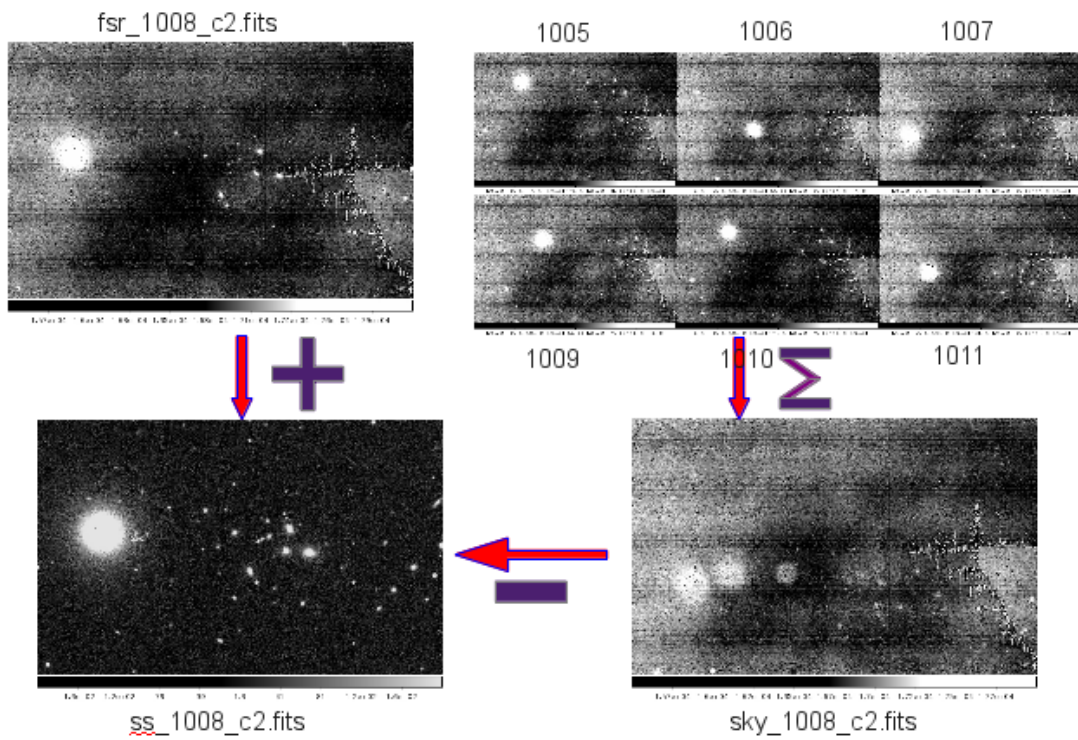


Figure 3.1: The sky subtraction method applied to the image with offset number 1008 (top left). The sky (bottom right) image were produced with a combination, represented here by a Σ symbol, of the 6 closest exposures (top right) and then subtracted to the current image to get a sky subtracted image (bottom left).

for 10 minutes.

Note that if the dithers are too small, some objects will be located in the background estimation near these own objects. And if the dithers are too large, the estimation of the sky here is calculated from the sky which is there. Also note that even if the dither angle is not too small, some large objects remain in the average of the sky estimation. Thus to prevent bright stars from overestimating the sky measure, objects must be masked before the sky subtraction.

The sky subtraction procedure “`irskysub.cl`” created for each image a corresponding sky subtracted image.

```
lc_dk_fsr_1241_c1.fits - > ss_lc_dk_fsr_1241_c1.fits
```

3.1.5 Masks construction

Objects must be masked in each image. These objects could just be found according to their signal to noise on each image. This was actually included in the sky subtraction routine by a 3 sigma rejection. In other works (Willis & al 2008), the masks are made in array regions containing objects above a specified ADU level. But, an other way to mask objects is to combine the images and get a higher signal detection. By this way, more objects were detected and though masked.

Thanks to IRAF routine “`imexamine`” and a visual detection of some reference stars, the center of these stars, and thus the offset between each image, was obtained. Then, the sky subtracted images were shifted and combined⁷ to get a better S/N image and detect more sources. The pixels containing sources were masked to do a better sky subtraction, which takes into account only the sky without the sources. In this combined image,

⁷ The combination was an average with a 3 sigma rejection and a maximum of 1 low and 1 high pixel rejected.

sources were detected if their S/N exceed 2.5. It was done with `imexpr` routine.

$$\begin{aligned}
 \text{object_map}[i, j] &= \left| \begin{array}{l} 1 \quad \text{if } \left(\text{Image}[i, j] > \text{Mean} + 2.5 \times \text{RMS} \times \sqrt{\frac{\text{max}(N)}{N[i, j]}} \right) \\ 0 \quad \text{else} \end{array} \right| \\
 \text{cl} &> \text{imexpr}(\text{"(a} > \text{c} + 2.5 * \text{d} * \text{sqrt}(e/\text{b})) ? 1. : 0. \text{"}, \text{object_map}, \text{image}, \\
 &\text{weight_image}, \text{sky_background}, \text{sky_rms}, \text{weight_max})
 \end{aligned} \tag{3.4}$$

Where *Image* is the previously combined image; *Mean* and *RMS* are the sky value and its deviation respectively; *N* is the weightmap of *Image*. `Object_map`, the created image, was supposed to have a value of 1 where there was an object and 0 otherwise. Then the object map image was smoothed within a box of 11×11 pixels. Each pixel got the value of the average of the $11 \times 11 = 121$ pixels around it. Pixels out of the image, were considered with 0 value. This tasks was done with “`boxcar`” routine.

$$\begin{aligned}
 \text{mask_smoothed}[i, j] &= \frac{1}{121} \sum_{i-5}^{i+5} \sum_{j-5}^{j+5} \text{mask_in} \\
 \text{cl} &> \text{boxcar}(\text{mask_in}, \text{mask_smoothed}, 10, 10, \text{bound} = \text{"constant"}, \text{contant} = 0.)
 \end{aligned} \tag{3.5}$$

Where `mask_in` is the previously obtained object mask, `mask_smoothed` is the new smoothed masks. This smoothed object masks contains real values between 0 and 1. The values higher than 0.08 were setted to 0 (i. e., masked) and the others were setted to 1 (i. e., not masked).

$$\begin{aligned}
 \text{mask_out} &= \left| \begin{array}{l} 0 \quad \text{if } (\text{mask_smoothed} > 0.08) \\ 1 \quad \text{else} \end{array} \right| \\
 \text{cl} &> \text{imexpr}(\text{"(a} > \text{b)?0 : 1"}, \text{"mask_out"}, \text{"mask_smoothed"}, 0.08)
 \end{aligned} \tag{3.6}$$

This procedure created masks for sources in the combined image: an “object map”. For each image and its corresponding offset, the masks were shifted with the opposite offset: an object map corresponding to this image was created. As a result, a set of object map was generated, one for each image.

`ss_lc_dk_fsr_1241_c1.fits` -> `msk_lc_dk_fsr_1241_c1.pl`.

3.1.6 Second sky subtraction and image stacking

The header of the images (ex: `lc_dk_fsr_1241.c1.fits`) were edited and a BPM were defined as the corresponding object map (`msk_lc_dk_fsr_1241.c1.pl`) instead of the true BPM image (`badpixel.c1.pl`). Then, sky subtraction was accomplished another time⁸. But this time, the sky estimation for each pixel did not take into account the flux from the sources in the object map. In other words, objects were more carefully removed before the second sky estimation than before the first one. So new sky subtracted images were computed. Their header were edited once more to put the true BPM (and not the object map any more). Next, the twice sky subtracted images were combined⁹ to obtain only one image for each field. The *I* band images were combined with the same task as the *H* band images, which were printed before performing the IMACS observations in *I* band in order to try and get the maximum overlap between the fields of the two bands.

3.2 IMACS *I* band images

IMACS is a optical wide field camera in Baade, Magellan telescope, Las Campanas, Chile. It has 8 chips of 4 arcmin per 8 arcmin. The observation was done during one night in October 2012 with the *I* filter. Afterwards , the reduction was processed with IRAF tool. Before a more detailed description of the numerical method used, the theory of the calibrations is described.

The calibrations are made to correct the images from the noise internal to the telescope. The detection noise can come from: thermal emission of the telescope, CCD noise, pixel to pixel response variation, read out noise. To correct from the:

1. Read-out-noise, the bias is employed. The RON is present in each image and is

⁸ The second sky subtraction was performed on the same image inputs to the first sky subtraction, just masking more sources. Note that the second sky subtraction was not performed on the once sky subtracted images.

⁹The combination was an average with a 3 sigma clipping and maximum rejection of 1 low value and 1 high value pixel.

due to the noise while reading the CCD (i. e., from the current amplification and the analogical to numerical conversion). The bias is a reading of the CCD with a closed buffer and a “fast exposure” (i. e., many readings with short time between themselves).

2. Thermal noise, the dark-exposure is used. It is an exposure with the same exposure time as the science image but with the shutter closed.
3. Pixel response, a flat field is employed. This exposure must be homogeneous on the detector. Usually, a unfocused light on the dome of the telescope is utilized. It is supposed to be fast enough to minimise the dark current but not too fast to avoid shutter effects.

In order to correct the images from the bias, dark and flat currents, they were modified by the following equation:

$$Cor = \frac{Raw - M_{dark} - M_{bias}}{M_{flat}} \quad (3.7)$$

Where Cor and Raw are the corrected and raw images respectively and M_{dark} , M_{bias} and M_{flat} are defined by :

$$\begin{aligned} M_{bias} &= \sum Bias \\ M_{dark} &= \sum (Dark - M_{bias}) \\ M_{flat} &= \sum (Flat - M_{dark} - M_{bias}) \end{aligned} \quad (3.8)$$

Where the sum represents an combination. The exposure time of the dark frames must be equal to the exposure time of the flat frames. This time is short so the dark subtraction to the flat can be ignored for optical images, only the bias subtraction may be performed.

3.2.1 Flat and bias

The calibrations were performed the day before the observations just after the leaving of the day team. First flat and bias, then dark during the twilight. The dark exposure is negligible compared to the bias, so this correction was not done. IRAF routine

“noao.imred.ccdred” was utilized for reduction. The procedure followed is described below :

1. Create the master bias with the function zerocombine and parameters : combine = median, reject = minmax, nlow=nhight=1, ccdtype = “” .
2. Remove bias from flat with the function ccdproc and parameters: trim =yes, zerocor=yes, all other booleans are set to “no”.
3. Create the master flat with the function flatcombine and the same parameters as zerocombine but also: scale=mode and “process”, “subsets”, “delete”, and “clobber” set to “ no”.
4. Correct raw (science) data with the function ccdproc using the master flat and master bias. The dark current is neglected in optical because thermal noise is low in comparison to the RON. Especially because the images were taken with only 5 minutes exposure.

3.2.2 Standard

As in FourStar images, the standards where reduced following the same way as the science images. Note that it was much easier to reduce the optical images as no sky subtraction were made. The corrected dithered image combination was performed with the same parameters as the IR combination even if only 4 optical images were combined whereas 40 IR images were combined. These standard images were expected to be used in order to determine the zero point (ZPT) of the night. But the ZPT was finally determined directly from the science images.

3.3 Stack chip

The small difference of ZPT between each chip was a motivation to combine the images of each chip in order to make a single large image. Indeed, the dithered offset was measured previously for the single chip images combination, and the distances (in pixels)

Camera	Chip Size (pixels)	Hole Size (pixels)
IMACS	4k × 2k	57 (short side) and 92 (long side)
FourStar	2k × 2k	120

Table 3.1: The size of chips and hole in pixel for the 2 cameras. $1k = 2^{10} = 1024$. For IMACS, the detector contains two different hole sizes, the ones that are separating the chip between their long side (4k pixels) and the one between their short side (2k pixel).

between each chip on the detector had to be determined. These distances are the sum of the chip size and the size of the hole between each chip. These data are exposed in Table 3.1.

For FourStar, a direct combination of all the dithered sky subtracted images was performed. The dither offset previously determined for one chip was used as the offset of the reference chip. And for the other chips, an other shift were added. The shift corresponds to the distance in pixel between the chip considered and the reference chip. Finally, the images for every exposure and every chip were combined with the following imcombine function:

```
cl>imcombine("@paris.list","paris_IR",expmask="paris_IR_wm",combine="average",reject="sigclip",offsets="shift_paris.txt",masktyp="none",blank=0.,scale="none",zero="none",weight="none",nlow=2,nhigh=2,mclip+,grow=0.,statsec="",expname="60",lthresh=INDEF,hthresh=INDEF)
```

Notice that the rejection utilized was a “sigclip” and no an “avsigclip”. Furthermore nlow and nhigh were chosen to be 2 instead of 1 because otherwise, lots of bad pixels appeared in the image.

On the newly created composite image, the astrometric solution were derived with the same procedure employed for individual chips (see section 4.1): SExtractor was used to extract the flux of objects from the composite image to a catalogue. Then the catalogue

was filtered (i. e., select bright stars) and SCAMP compared the filtered catalogue to 2MASS references.

The WCS matching always converged because the field of view was now 4 times bigger because composed of 4 chips. The convergence of SCAMP was a good test to see if the chip combination was good. The problem was that the WCS projections was not good enough to be able to compare sources together on different images.

For IMACS, there was a trap: on the camera, the reading of the “upper” chips (i. e., 5,6,7, and 8) is performed in the other side than the “lower” (1,2,3,4) chips reading. And thus, the images from the chips 5,6,7, and 8 are rotated by 180° . So, these images were rotated again by an other 180° . This was done using “imrot” routine from WCStools. This software is in an archive in “Theli” or “Scisoft”. Just untar it and use a compiler (GCC) to create some binary executable. One of these executable, called “imrot” is rotating the image. The following commands were employed:

```
for i in $(ls 1_*c{5,6,7,8}.fits) ; do mv $i $i"_old" ; done
for i in $(ls *fits_old*) ; do $PATH/wcstools - 3.8.3/bin/imrot -r 180 $i ; done
for i in $(ls *r180*) ; do tmp = ${i%_old}; mv $i $tmp%r180.fits".fits ; done
```

(3.9)

The first command changed the name of the FITS images (to have a backup). The second rotated the images by 180° and rename it. And the third changed the name of the rotated images to the original name. The name of the rotated images contained r180 because it is a string automatically added by imrot task. Thanks to this little script, it was not needed to change the name of the frames in the list of images to combine.

After this rotation, the images were combined. The imcombine parameters were not exactly the same employed for the IR data because there were only 3 to 10 exposures to combine. This nhigh and nlow were setted to 1. The astrometric solution was calculated for optical images with the same method as for the IR composite images.

Chapter 4

Calibration and photometry

Paju kieke mew montulcefegey.

“The poisonous spider sometimes saves people”

From the comparison between the reduced images and catalogues from some international database, it is possible to provide a referenced position and brightness. This permits to relate the images to works already done or in process. Observational works like the luminosity function or colour-colour diagram and theoretical works like stellar dynamics or galaxy evolution. And from the comparison between images among themselves, it is possible to deduce some independent informations from spatial distribution (correlation function) and relative detectability (dropout, variable objects), shape (concentration) or abundances (number count). Of course the informations deduced without any reference, comparison or modelling are more limited because its are based on less information (observational or theoretical).

Both images in H and I band were aligned to the world coordinate system (WCS) with the help of two programs: SExtractor (Bertin & Arnouts 1996) and SCAMP (Bertin et al 2006). The first one detects sources and extracts their fluxes from a 2D image to an ASCII catalogue. The second compares catalogues and estimate a WCS projection in order to align images to the WCS or between themselves with an arbitrary coordinates system. This procedure doesn't need an established photometric calibration (i. e., ZPT) because it is comparing source positions together independently from their magnitudes.

Moreover, for each band these sources are detected without considering the other band. Actually, the images were first deformed in the plane of WCS and then their magnitudes were scaled. These two deformations may have been done simultaneously from the same software. But apparently, today's SCAMP is not able to determine the photometric solution. This may be a future improvement.

4.1 WCS

From both optical and infrared images, SExtractor detected sources with a S/N higher than 1.5 on more than 5 adjacent pixels. And it returned, for each source, the CLASS_STAR, FLUX_AUTO and of course the its position on the image. CLASS_STAR takes a value between 0 and 1 and indicates the probability of being a star (i. e., a point source) according to the shape of the source. A Gaussian point spread function (PSF) was assumed¹. FLUX_AUTO is the flux of the object measured in a Kron aperture (Section 4.3).

Both CLASS_STAR and FLUX_AUTO values permitted to select only sources which are bright and likely to be stars. This decreased the number of sources which were aimed to be matched together. It is recommended to detect on the image the same number of sources as there are on the reference catalogue to match. In that way, the image deformation is more accurately calculated. Therefore it is better to keep only bright sources, likely to be both on the science images and on the reference database. It is also better to select stars because their astrometry, their center is better determined than the center of galaxies.

The initial selection included sources with CLASS_STAR upper than 0.8 and which belongs to the 20% brightest sources. Sometime the selection had to be relaxed. But while including faintest sources, lots of newly selected sources actually belonged to the noise in the borders of the images. This could be noticed by displaying the selected sources on ds9 software. At the borders, the weightmap of the image is lower (i. e., border are regions of the image which are combination of only few exposures). In addition, the

¹ This PSF seems to be reliable since the images were taken without adaptive optic.

detector sometimes had defects in its extremities: there is more noise and ghosts on the sides of the chips where spurious detections were expected. To avoid that, the objects located in the extrema of the images were excluded from the selection while including fainter sources.

To extract only the wanted source, it was actually faster to run SExtractor twice. The first time, it only returned the few parameters making the selection possible. Next, once the objects selected, a second run was performed in association mode to get informations from only the selected sources. This run returned parameters occupied later by SCAMP such as RA,Dec (and not only x,y), Flux, Flag and its errors.

The image needs to be roughly positioned and oriented in the WCS for SCAMP to find an astrometric solution. It is necessary to fill the image header with some keywords known by SCAMP (See table 4.1). This can be seen as a first guess of a least square fit method or as a selection of a sub-catalogue in the large reference catalogue. It is actually both. The astrometric approximation of each image was done according to the “RA”, “DEC” and “SCALE” keywords, present in the header of the image. The orientation was also written in the log of the observation night but in this work, the north were often pre-positioned by comparison with some image database thanks to Aladin² interactive sky atlas (Bonnarel & al 2000).

To compute the WCS solution SCAMP was utilized with a cross identity radius of 3 pixels. This means that SCAMP was looking at a transformation leading the maximum number of the image stars closer than 3 pixels away from some reference stars. A polygonal WCS distortion of order 2 was employed.

Sometimes SCAMP converged but the astrometric solution wasn't good, in this case some warnings were outputted. Anyway a visual check was always performed with ds9 by loading on the image the positions of the objects present in the reference catalogue. An other possibility to check the astrometric solution would have been to write a software which shows the chip positions on the WCS: if the chips are well positioned on the WCS, they should be aligned between each other as they are on the camera.

With the selected bright stars on the image and a WCS reference catalogue USNO-B1,

²<http://aladin.u-strasbg.fr/>

Key	Possible Value	Explanation
CTYPE1	'RA—TAN'	Type of projection of image axe X on the WCS plane Should be of 8 characters
CTYPE2	'DEC—TAN'	Same with Y
CUNIT1	'deg '	Units of CTYPE1: here pixel/degree
CUNIT2	'deg '	Same with CTYPE2
CRVAL1	8.5665	WCS value of a reference point in Ra
CRVAL2	2.3677	Same in Dec
CRPIX1	0.0	Pixel value of the reference point in X
CRPIX2	2200.0	Same in Y
CD1.1	-4.5E-05	Rotation matrix CD
CD1.2	0	from the reference point
CD2.1	0	WCS-CRVAL = CD(pixel-CRPIX)
CD2.2	4.45E-05	

Table 4.1: The header keywords necessary as initial guess for SCAMP. These keywords are stored in the first column. There is, in the second column, an example value, and the third is an explanation of this keyword.

SCAMP always found an astrometric solution for optical images. Some optical images needed a relaxed selection but all were aligned directly to the catalogue UNSO-B1. Meanwhile, the IR images could not always be directly matched with their 2MASS catalogue. This was partly due to the FOV of the chips utilized in *H* band which is twice smaller than the FOV of the chips utilized in *I* band. Moreover, the 2MASS catalogue contains fewer objects than USNO-B1 catalogue.

To determine the astrometric solution with only half of the IR images, it was helpful to employ the optical images as references. This allowed to select sources even in the reference catalogue. The objects in the reference catalogue were selected as the objects in the catalogue to match: objects with *CLASS_STAR* > 0.8 and belonging to the 20% brightest objects were selected and utilized as a astrometric references.

There were 8 chips in the IMACS mosaic and 4 in the FourStar mosaic. And IMACS chips didn't have the same FOV as FourStar chips. So objects from only one optical chip couldn't be setted as the only astrometric references to align an IR image. Therefore, for each pointing, the 8 optical chip catalogues were merged to get a single catalogue for this pointing. The catalogues were produced and merged in ASCII format and then converted to LDAC_FITS format, a format necessary to run SCAMP. The command to convert a catalogue from ASCII to LDAC_FITS format is described below:

```
asctoldac -i ASCII_catalog -o LDAC_catalog -c asctoldac.conf -t OBJECTS
```

Where *i* stands for input, *o* output, *c* configuration file (shown in appendix C) and *t* table name. Putting "OBJECTS" as table name works fine for the catalog to be read by SCAMP. Asctoldac is a binary task present in Theli (Erben, T. & al 2005) for example. Once the catalogues merged, they could be used in SCAMP as reference by setting the SCAMP parameters `-ASTREF_CATALOG FILE -ASTREFCAT_NAME LDAC_catalog`. Where LDAC_catalog is the name of the LDAC catalog, the output of asctoldac function. The keys for astrometry defined by the asctoldac configuration file (asctoldac.conf) and present in the LDAC catalogue header must match the ones in SCAMP configuration file. A configuration file with SExtractor keys can be utilized.

To resume, the astrometric solution was done automatically, without manually selecting

stars in the images and catalogue. This manual method could have been done using IRAF, but as many images were processed, the automatic method resulted to be faster.

4.2 Zero point

The flux of the objects in the sky is proportional to the value (in ADU) they have on the image. The factor of proportionality is given by a conventional parameter called “the zero point (ZPT)” which is the the magnitude a star would have if its arbitrary flux was 1 ADU for 1 sec of exposure (Equation 4.1).

From some standard sources, the absolute photometry can be calibrated by comparing the referenced flux (in Vega magnitude) and the relative flux in the images (in ADU). The standard images were reduced like the science images. A special care was taken to correct for the dark current due to the shorter exposure time of the standards. With IMACS, The exposure time of the standard stars could not be shorter than 1 second. This is due to the time necessary to open and close the camera shutter. Unfortunately, with 1 second exposure, most of the standard stars were saturated. So the science images themselves were taken as references for the photometric calibration. The method to determine the ZPT from one image is described hereafter:

1. Load the reference catalogue : Take the coordinates of the standard stars of the catalogue (2MASS for IR and USNO-B1 for optical). In ds9, load the image, press Analyse>Catalog and select the desired catalogue. Then save the catalogue in ASCII format: File>Export>Starbase in the catalogue window. And save the region in the coordinates of the image: in the catalogue window, File> Export as region and in ds9: Regions>Save regions. Choose coordinate type “image” and file type “XY”. Note that ds9 can be easily scripted³.
2. Extract flux from the wanted sources : Use the x and y position of the regions to extract the corresponding objects flux on the images with SExtractor in association mode. Here, the flux was measured with MAG_AUTO SExtractor parameter.

³ <http://hea-www.harvard.edu/RD/ds9/ref/command.html>

Maybe the association radius must be increased higher than the default value (2 pixels): here 4 was established. This procedure gives the relative flux (in ADU) of the regions.

3. Compare the fluxes: The ZPT is conventionally defined as below :

$$ZPT = MAG + 2.5 \times \log(f) + 2.5 \times \log(t) + c_a \times a \quad (4.1)$$

Where MAG is the referenced magnitude of one object, f is the flux of this object in the image (in ADU), t is the exposure time (in second), c_a is the extinction correction (in magnitude) and a is the airmass (no unit).

The ZPT can be calculated with Equation 4.1. If a Gaussian statistic is assumed, the error on the ZPT is the square root of the sum of the square of its constituents. It appeared that the dominating error was on the referenced MAG. In the *H* band, the typical error was 0.1 for a 15 mag (Vega) object in the 2MASS catalogue. In the *I* band, the photometric error of one object is described to of the order of 0.25 mag in the USNO-B1 catalog. The flux of the object on the images (in ADU) was well determined, much better than the referenced magnitude, the error can be neglected. The error on the exposure time was not defined. But the time term vanished while measuring magnitude with this ZPT, employing the same equation 4.1 and isolating the MAG term. The atmospheric extinction coefficient, the airmass and its errors could also be neglected as explained below.

The error in the ZPT determined from one object was about 0.15 mag. This is higher than the difference of zero point encountered for different airmass. Actually, the airmass varied typically from 1 to 1.3 between fields. The values of atmospheric absorption can be found in the documentation or calculated on the science images drawing a function of ZPT according to the mean airmass of the observation. The extinction coefficient is 0.04 mag in *H* in Paranal (Lombardy et al 2011) where the *H* band images were taken. This value is coherent with a theoretical calculation (Manduca & Bell 1979). And for the *I* band, the extinction coefficient is 0.03 mag in La Silla (Matilla et al 1996), just next to las Campanas where the *I* band images were taken. This value is

the same as the I band atmospheric extinction derived in Paranal (Patat et al 2010). These coefficient, led to a maximum difference of ZPT due to the change in airmass of $0.04 \times (1.3 - 1.0) = 0.012$ in the H band and 0.009 in the I band. Therefore the change of mean airmass for each object, can be neglected in the estimation of the ZPT.

To neglect the airmass permits to estimate the same ZPT for all the night if there is no atmospheric variations (clouds or temperature variations). While measuring the ZPT for different pointing and different mean time, it was noticed that the ZPT was actually constant over the night. Consequently, for each chip, all the observations were gathered: all the objects detected in one chip and their corresponding fluxes were considered together.

The ZPT was then determined statistically. Objects with a referenced magnitude brighter than 10 were rejected because they are saturated on the image. Objects with a referenced magnitude fainter than 15 were also rejected because their referenced magnitude is inaccurate. For each of the selected objects, the ZPT was determined with Equation 4.1. An illustration is given in Figure 4.1. A first median of the ZPTs estimated with the selected objects was calculated. Next, objects which had a corresponding ZPT father than 0.5 mag from the median were rejected. Finally, a second median was calculated again without taking into account the rejected objects. The values obtained are shown in Tables 4.2, 4.3 and 4.4. The 0.15 mag RMS in the ZPT is higher than the difference between the ZPTs of each chip. Therefore, it was decided to use the same ZPT for all the chips. The resulting ZPT chosen for all the RCS2 images was 25.81 mag (Vega) in H band and 27.25 mag (Vega) in I band. The error of this ZPT is of the order of 0.1 mag. The Vega magnitudes were transformed to AB system⁴ (Blanton & al 2007) and the ZPT was recalculated assuming a 1 second exposure time.

$$\begin{aligned}
 \text{In } H & : ZPT = 25.81 + 1.39 + 2.5 \times \log(11.64) = 29.86 \pm 0.1 \\
 \text{In } I & : ZPT = 27.25 + 0.45 + 2.5 \times \log(300) = 33.89 \pm 0.1
 \end{aligned}
 \tag{4.2}$$

Where the first term is the ZPT in Vega mag and calculated using the true exposure time; the second term is the magnitude (AB) of Vega in this band and the last term

⁴ See the transformation coefficients at: <http://www.astronomy.ohio-state.edu/~martini/usefuldata.html>

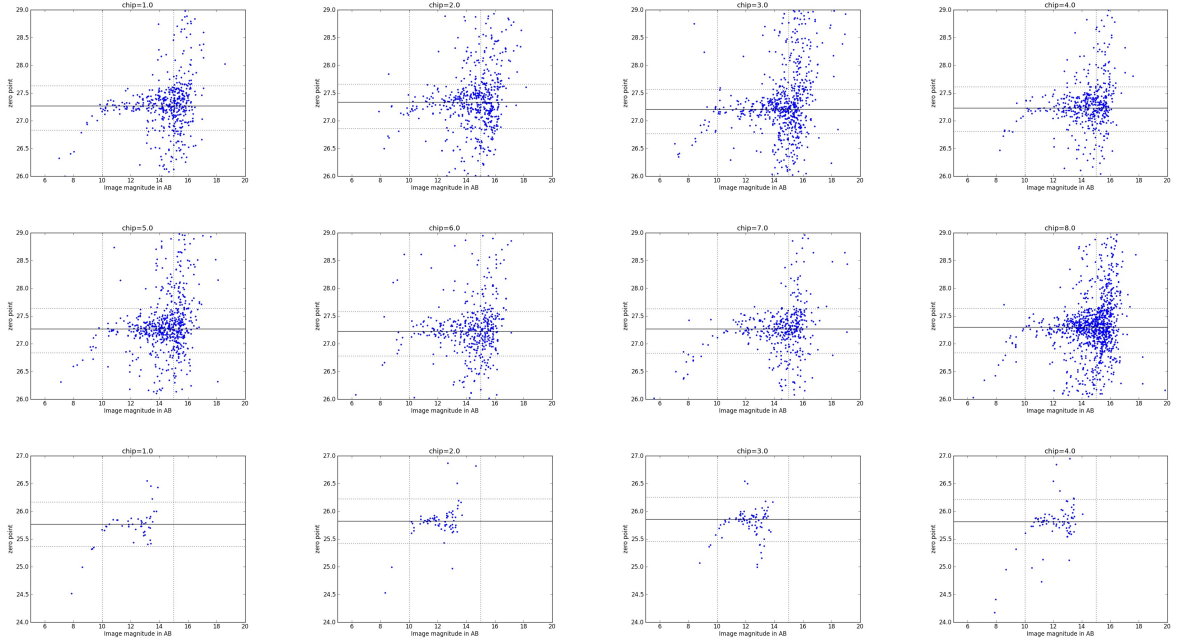


Figure 4.1: ZPT vs Mag. In the top 8 panels: the I band chips and in the bottom 4 panels: the H band chips. The horizontal filled line represents the median of the whole distribution and the dashed lines represent the selection: stars inside the dashed rectangle were utilized to determine ZPT of the chip.

is the correction to get a ZPT which suppose that the image was taken in a 1 second exposure. This ZPT was easier to use than a ZPT calculated for the true exposure time because the time term vanished while measuring the true magnitudes of the objects.

During this work, some reduced images of the RCS2 clusters in R band were obtained. The ZPT and its error of these fields were calculated with the same method of the median. An independent ZPT were calculated for each image. The ZPT of each image are shown in Table 4.4.

Chip	Median 1	Median 2	Mean	RMS
1.0	27.23	27.26	27.27	0.16
2.0	27.26	27.33	27.31	0.17
3.0	27.16	27.20	27.20	0.16
4.0	27.21	27.23	27.23	0.16
5.0	27.23	27.26	27.26	0.15
6.0	27.17	27.22	27.21	0.17
7.0	27.22	27.26	27.26	0.17
8.0	27.23	27.29	27.28	0.16

Table 4.2: The ZPT calculation for each R band chip. The first column represents the chip number; the second and third column are the median of the ZPT calculate with and without the 0.5 magnitude clipping respectively; the fourth column is the mean of the ZPT estimated for each object in the selection and the last column is the standard deviation of the selected objects from the second median.

Chip	Median 1	Median 2	Mean	RMS
1.0	25.77	25.76	25.74	0.14
2.0	25.82	25.82	25.82	0.13
3.0	25.85	25.85	25.84	0.13
4.0	25.81	25.81	25.82	0.13

Table 4.3: The ZPT calculation steps for each H band chip. Columns have the same meaning as Table 4.2

Object	Zpt	err_zpt
RCS2-0047_18.79	33.87	0.12
RCS2-0047_2527	33.89	0.08
RCS2-0047_4381	34.05	0.13
RCS2-0310_2399	33.91	0.12
RCS2-2143_21.58	33.84	0.14
RCS2-2143_21.79	32.24	0.10
RCS2-2143_21.85	32.22	0.12
RCS2-2338_23.48	33.94	0.13
RCS2-2338_23.60	33.83	0.12

Table 4.4: The ZPT for each image in R band.

4.3 Pixel matching and Photometry

Once the images calibrated in position and photometry, they were compared together. In this work, the detection was done on the H band images. The flux of these objects was then measured in H , I and R band. All these images were aligned in WCS by SCAMP (Section 4.1). They were reshaped using SWarp (Section 4.3.1). The photometry was then done occupying Sextractor in dual mode (Section 4.3.2). This mode enables to detect objects in one image (H) and to measure their flux in others (I or R). All these 3 softwares (SExtractor, SCAMP and SWarp) were created by the same person Emmanuel Bertin.

4.3.1 Pixel matching (SWarp)

SWarp⁵ (Bertin et al. 2002) is a software which interpolates an image to the specific shape of an other. In other words, it is modifying the pixel structure of one image. This modification aims to get the same pixel position in two or more images : for the same pixel position on the image, the same WCS position in the sky so the same source

⁵<http://www.astromatic.net/software/SWarp>

present (or not) there. The images inputs to SWarp need to be previously aligned to the WCS. Then images are deformed in two steps:

1. One of the images (the reference image) is passed as a single argument to SWarp. In this way, the software modifies its shape and its header to remove the rotational (CD1_2 and CD2_1) and the polygonal (PV1_1,PV1_4,PV2_5...) distortions of the image.

```
SWarpref_IR.in.fits-IMAGEOUT_NAMEref_IR_SWarp.fits-WEIGHTOUT_NAME
Eparis.cum.SWarp_IR.weight.fits
```

2. Once the reference image straighten, the other images are deformed to the reference image structure. The reference image header is copied to an ASCII file (im_opt_SWarp.head) with the same name as the output of the second command, replacing .fits by .head. To conceive this file, copy paste the header of the reference image thanks to ds9 because IRAF task imheader does not copy the first fields of the header (NAXIS1 and NAXIS2). Finally, the following command line deforms the images.

```
SWarp im_opt_in.fits-IMAGEOUT_NAME im_opt_SWarp.fits -COMBINE_TYPE
E AVERAGERESAMPLE Y -RESAMPLING_TYPE NEAREST -RESAMPLE_SUFFIX
.resamp.fits-WEIGHT_THRESH 0. -RESCALE_WEIGHTS N -BLANK_BADPIXELS
YRESAMPLE_DIR /temp_sw -DELETE_TMPFILES Y -FSCAL_ASTRO_TYPE
FIXED-SUBTRACT_BACK N -VERBOSE_TYPE NORMAL -WEIGHTOUT_NAME
im_opt_SWarp.weight.fits
```

Where the first parameter is the name of the input image to modify and IMAGEOUT_NAME is the name of the output image. -RESAMPLE is setted to Y (yes) in order to resample the input image: this is actually the goal of this task.

-BLANK_BADPIXELS is setted to Y value in order not to consider the bad pixels of the input. Actually, in this work, there were not any have bad pixel masks in the dithered and co-added images. This parameter was just employed to keep a good and versatile command line. The background was not subtracted and a weight map (im_opt_SWarp.weight.fits) were outputted.

In order to perform this task, the polygon deformation of the WCS matrix should not be of an order higher than 2, otherwise SWarp cannot recognise the WCS transformation. SWarp generated images with the same shape and thought SExtractor could then be employed in dual mode as follows.

4.3.2 Photometry (SExtractor)

To detect sources and measure their photometry, SExtractor was employed in dual mode imaging which permitted to detect sources in one image and to measure photometry in an other. This method provides 2 advantages : first it makes possible to extract photometry from sources that may not be detected in the image of measure and then it ensures to have the same aperture in all the bands preventing from some color shape dependences in the photometry. In fact, if the photometric apertures are the same for all bands, fluxes are measured from the same region whatever region lies behind the aperture. The command line employed to extract fluxes with SExtractor in dual mode is the following:

```
sex $detection,$measure -CATALOG_NAME Sex/sex1_${detection%%fits}cat -CATALOG_TYPE ASCII -DETECT_THRESH 2.00000 -PARAMETERS_NAME Sex/sexy.param -DETECT_MINAREA 5 -PIXEL_SCALE 0 -SEEING_FWHM 0.8 -BACKPHOTO_TYPE LOCAL -FILTER_NAME Sex/default.conv -STARNNW_NAME Sex/default.nnw
```

Where a directory called Sex was previously created. It contained the files default.conv and default.nnw which are the SExtractor default filter and neural network.

The filter employed is a pyramidal function, it was used to smooth the image and get a better detection but it was not used for the photometry. The neural network defines how to determine the separation star-galaxy.

Detection and measure variables were previously defined, they represents the detection and measure images respectively. In H band detection and measure images were setted as the same H band image. This permitted to have the same H band detection images for all flux measures (in H , I and R band). A detection threshold (-DETECT_THRESH parameter) of 2 (i. e., $S/N > 2$) were chosen and 5 adjacent pixels above the threshold were required for a detection (-DETECT_MINAREA parameter). The FWHM (0.8 arcsec) was included in the input. Then SExtractor returned the FWHM of the points, the FWHM of point-like objects was setted as the pic of lowest value in the FWHM histogram of the sources. Then SExtractor was runned once more with this true FWHM as the input FWHM. SExtractor read the pixel scale in the header of the FITS images. A set of catalogues of fluxes in different band was obtained. An other advantage of this method is that the catalogues for different band matches together line by line, So they are easy to read, merge together.

The flux of each source was measured with MAG_AUTO output parameter which means that the flux was integrated in a Kron aperture (Kron 1980). The procedure is explained below:

1. The number of pixels above the threshold are selected. They represents the “isophotal area” which is an area in number of pixels. Note that, as defined in SExtractor inputs, the isophotal area must be larger than 5 pixels for a detection. An isophotal radius is defined as $R_{Iso} = \sqrt{A_{Iso}}/\pi$. Where R_{Iso} and A_{Iso} are the isophotal radius and area respectively.
2. The ellipticity ϵ and position angle θ of the source are derived from the Kron second order moments defined in Equation 4.3.

$$\bar{X} = \frac{\sum I(r) * x^2 dr}{\sum I(r) * x dr}; \bar{Y} = \frac{\sum I(r) * y^2 dr}{\sum I(r) * y dr} \quad (4.3)$$

Where the sum is performed in a circle of radius $2R_{Iso}$ around the gravity center of the object. The parameters r is the distance of the pixel from the gravity center of the object; x and y are the projections of r on the x and y axes respectively and $I(r)$ is the value of the pixel.

3. The Kron radius⁶ or Kron first order moment is derived by Equation 4.4.

$$R_{Kron} = \frac{\sum rI(r)}{\sum I(r)} \quad (4.4)$$

Where the sum is performed on the same circle of radius $2R_{Iso}$. The Kron radius is noted R_{Kron} and the other parameters have the same meaning as before.

4. The flux of the image is integrated in an elliptical aperture. The ellipse major and minor axes are $R_{Kron} \times k/\epsilon$ and $R_{Kron} \times k\epsilon$ respectively. The parameter k can be set in the input; its default value, 2.5, was employed here. For faint sources, the Kron radius may be very small, that is why a minimum Kron radius can be setted in the input, its default value: 3.5 was employed here. The sky background is subtracted from the Kron aperture photometry. Here the sky was estimated with 64 pixels around the Kron aperture.

4.4 Detection Limit

In this section, 3 ways of estimating the detection limit are presented. The first one is the fastest and relies only on a mathematical S/N estimation. The second one is to see where the luminosity histogram begins to drop. It gives a higher (in mag) limit of the detection limit. The last one is the most time consuming but the most reliable. This method consists of drawing Gaussian PSF of a certain magnitude on the image and then trying to detect them. The ratio of the number of stars generated by the number of stars detected is the completeness for this magnitude.

⁶ Kron defined his aperture radius as the second order moment of the radius (i. e., $\bar{X}^2 + \bar{Y}^2$). But here the Kron radius is defined as its first moment.

4.4.1 Signal/Noise

The theoretical 5 sigma detection limit in I images is calculated below. The RMS of I images is 75 ADU (28.5 mag_{AB}). So 5 sigma detection is $5 \times 75 = 375$ ADU. But as 5 pixels above the threshold are required, The flux of an object must be at least $375 \times 5 = 1875$ ADU. This is in mag :

$$33.149 - 2.5 \times \log(1875) = 24.97 \quad (4.5)$$

Because 33.149 is the ZPT for the I filter.

The RMS of H is typically of 5 ADU (28.1 mag_{AB}). And the ZPT is 29.85. So the 5 sigma detection limit in H band is

$$29.85 - 2.5 \times \log(5[\text{pixel}] * 5[\text{ADU}] * 5[\text{sigma}]) = 24.61 \quad (4.6)$$

In the same way, the detection limit of a R band image if an image is present in the database, is:

$$33.83 - 2.5 \times \log(5 * 5 * 100[\text{ADU}]) = 25.33 \quad (4.7)$$

But a galaxy, or even a star of a certain magnitude will not spread all its light over only 5 pixels. So this detection limit must be considered as a fainter limit for the detection, because some brighter objects may not be detected.

4.4.2 Luminosity Function

Figure 4.2 represents the luminosity histogram of all sources in all fields in H and I bands. The histogram of the number of sources of certain flux begins to drop from a perfect Schechter distribution. This is mainly due to incompleteness. So it seems that after mag 23 in H and mag 23.5 in I , not every object can be detected. This is a stricter result than the utopic 24.6 and 25 previously calculated. But the degree of incompleteness for a certain magnitude is not given by this method.

4.4.3 Fake stars

100 fake stars of a certain magnitude were generated, putted on the image and then detected or not. The number of stars detected represents the degree of completeness.

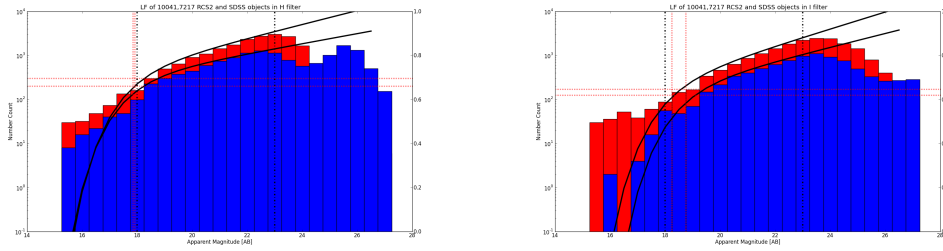


Figure 4.2: The luminosity function of all sources. Left: in *bandandright* : *in band*. The dashed vertical lines represent the limits of the Schechter fit which is draw as continuous curves. The SDSS histogram is the blue (bottom) one. The other, the red one is for RCS2 sources.

This was performed for a range of magnitude and the completeness degree was obtained for each magnitude.

How to create fake stars ? They were just drawn on the images with their shape and position. First a black image (only pixels with a zero value) with the same shape as the science image was created. 100 sources of 1 pixel were putted on this black image. The sources have a flux in ADU corresponding to their magnitude utilizing ZPT equation (Equation4.1). After that, the image with 100 pixel-star were convolved to a Gaussian pattern, in order to have star with a true FWHM and not just 1 pixel stars. A 20 pixel square image was employed as a Gaussian pattern. The FWHM of real point like sources varied between 5 and 7 pixel. It was noticed, while detecting the fake sources with SExtractor that it estimates very well the FWHM (to a 0.05 pixel error) and this was a way to check if the generated fake stars actually had the desired FWHM. Finally, the fake star image was summed to the true image to get the noise of the true image. An illustration of these fake images is given in Figure 4.3.

How to detect the fake stars ? With the same extraction method employed to detect the true object in order to be coherent. Figure 4.4 shows the detection completeness in functions of the magnitude of a star. Note that for a galaxy, the detection is harder because the angular size is larger: the light pattern is not as dense as for a star. For example, in the 2MASS documentation, it is said that the detection limit for galaxies is 0.8 mag brighter than for stars. So, once again, this is an upper limit of detection but

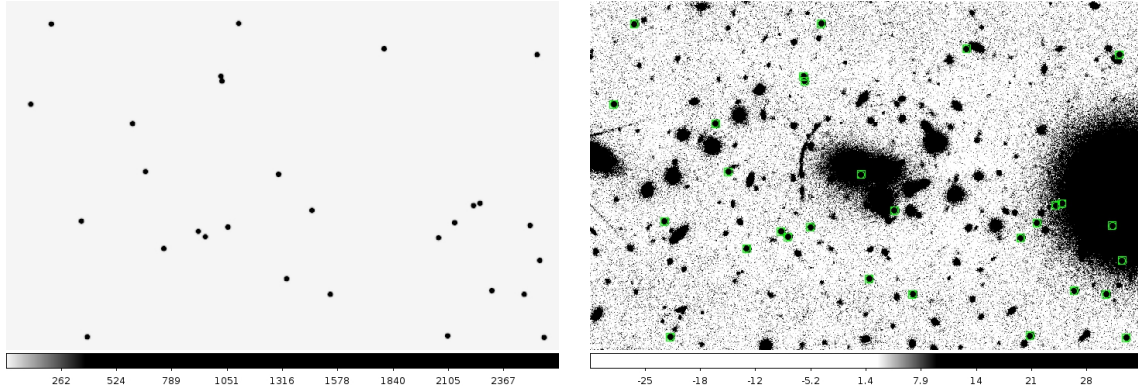


Figure 4.3: Fake Stars: left side the fake star image, for 100 stars of magnitude 18. These stars were computed with a Gaussian pattern of 20×20 pixel and then putted on an image with a background of 0 ADU. And in the right side, the fake star image summed with the true image, The fake stars are located in the regions selected with a green square.

still, very close to reality if compact sources are considered. Let's consider the detections limits defined above. Looking for dropouts with $I - H > 2.5$ and $R - I > 2$, the I and R images were the limitations of the dropout detections : an object can be detected in H band and not in I or R band without having the desired color criterium because this object may have a I and R flux faintest than the detection limit. A possible solution is to combine the I and R images to go deeper. One can cleverly add the image taken in I band and the image taken in R band to make a composite $I + R$ band image.

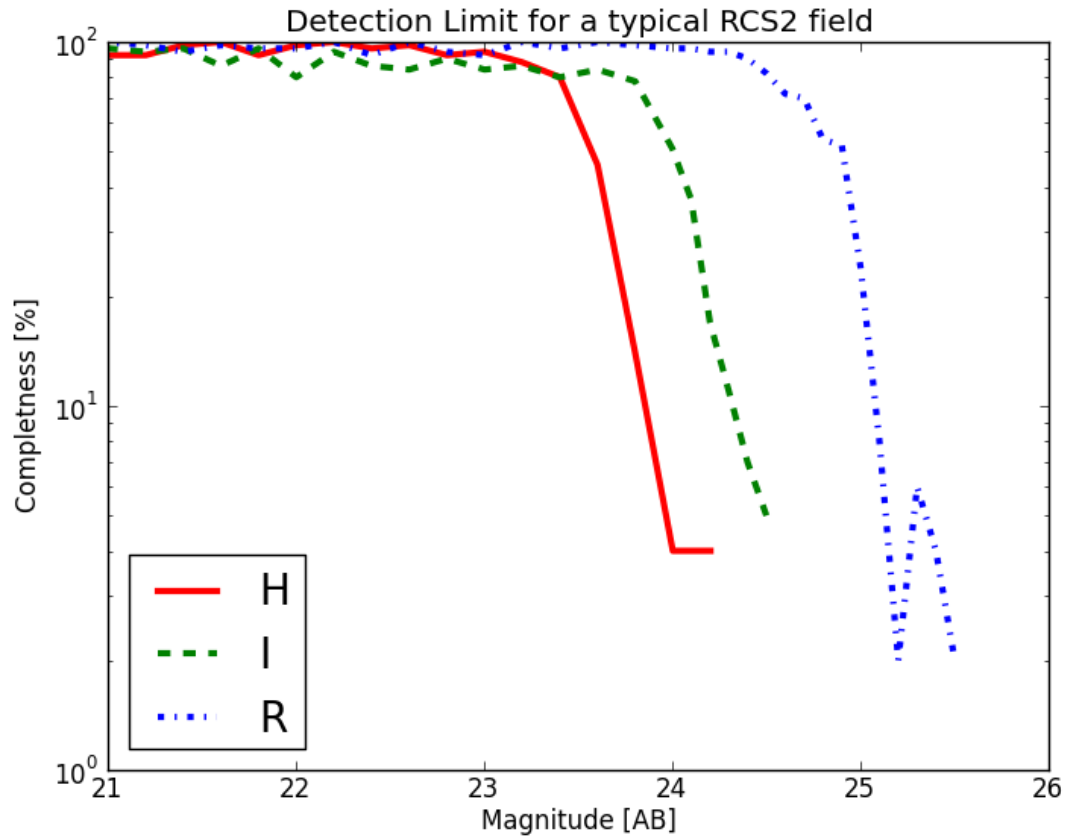


Figure 4.4: Completeness: The completeness in function of the magnitude of a typical RCS2 field. In red filled line: H band ; in green dashed line: I band and in blue dashed dotted line: R band. The detection limits are 23.5 , 24 and 25 mag_{AB} for H , I and R images respectively. Note that even at high luminosity, not all the stars are detected. This is due to a statistical overlapping with background true objects. That is why a completeness of 80% were chosen to define the detection limit.

4.5 Composite band

Looking for objects of color $I - H > 2.5$ and $R - I > 2$ (see Chapter 5) , the *or* band detection limit will be the flux limitation.

To go deeper in the optical images, it was decided to combine the *I* and *R* band images. In (Finlator & al 2013) two images of different bands (*J* and *H*) were also combined. To do so, the two images were scaled to match the same zero point. And then the images were combined with a weight proportional to the inverse of the variance (i. e., RMS^2) of each image. The method is described below.

- **Scaling** : Scale the *R* images in order to match the *R* images zero point. In this way, if one objects has no $I - R$ color terms, the flux of this object (in ADU) is equal in *I* and *R* band images. In other words: the conversion factor between ADU and mag_{AB} should be the same for both images. This seems necessary to make an average : if this scaling is not performed, two images may be combined, one with a 30 000 ADU flux and an other with 10 000, for the same object. Therefore, this average would have no sense.

In order to scale the *R* image, its zero point is acquired. For example, for one image, ZPT=33.94. This ZPT is an effective zero point calculated if the exposure time was 1 sec because the exposure time wasn't given in the header of the *R* images. Furthermore, it is easier then to recover the magnitude of objects supposing an exposure time of 1 sec to estimate the zero point. The effective zero point of the *I* image is also acquired, for example 33.15. So, in the example described, the zero point of the *R* image is $33.94-33.15=0.79$ mag higher than the *I* image one. This means that there are, for the same object the number count is: $10^{0.4 \times 0.79} = 2.07$ higher in the *R* band than in the *I* band. Think: the higher the zero point, the more ADU one gets for the same mag, see Equation 4.1. Therefore, to get the same ZPT on each image assuming the same 1 sec exposure, the *R* band image is divided by 2.07 thanks to the IRAF tasks "imarith".

- **Weighting** : Before combining the images, it is necessary to find the weight corresponding to each image in the weighted average. Maybe an image is much deeper

than the other and thus it will be more weighted in the average because it contains more signal. The deepness of one image is proportional to its S/N. So for the same signal and the same ZPT, this weight is proportional to the inverse of the variance (i. e., $\propto 1/RMS^2$). As SWarp previously aligned the images, lots of pixel values are zero. So if the IRAF tasks “imstat” is utilized, the mean will be underestimated, and thought the RMS overestimated. A solution is to assign the value -32000 to pixels with a zero value and then to clip the values inferior to -31999 in “imstat” routine. An other solution is to make a Python routine to consider only the non null pixel. To be correct, one should also remove the objects. An iterative way of removing objects with fluxes with a high S/N can be written. Or, instead of calculating the Root Mean Square (which will too high due to the presence of objects) one can, as done in this work, calculate the Root Median Square. The variance of a image compose of several dithered images is not constant along the image : it is higher in the border, where the weight map is higher. Therefore, one should compute the variance only in the central region or consider that the variance is proportional to $1/\sqrt{N}$ where n is the number of exposure stacked at this pixel position. In this work, the central variance was considered.

Next, each image gets a weight proportional to the inverse square of this value (the root median square). Usually, in this work, the *R* image were twice deeper than their corresponding *I* images. Note that one can also weight by the inverse size of the band to make a true composite filter. Or, one can consider that for example one narrow band carries as much information of one broad band. Whatever, then, this operation need to be consistent with the model of galaxy color one computes.

- Combining : Take the images with the same ZPT and combine its with a weight proportional to its deepness (previously calculated) using the IRAF tasks imcombine and putting in arguments for weight: a list of numbers (the respective weight of each image in the input list). Combine with an average without rejection. Don't subtract background of the images subtracting the mean of each image to

this image. This task is obviously useless because it can be done later and more properly.

Chapter 5

Model

Trewa ta trewa

“A dog will always be a dog”

Some models were constructed to determine which color cut permits to select Lyman break galaxies (LBG) at $z \sim 6$ excluding the maximum number of lower redshift interlopers. As a $z \sim 6$, the Lyman break redshifts into the I band, some images were taken in the H and I band. Some additional images in R band were also obtained.

A range of galaxy SEDs were synthesised, redshifted properly and passed through the H , I and R filters utilized. This allowed to determine the $I - H$ and $R - I$ criterium to employ to select $z \sim 6$ galaxies.

Gravitational magnification is independent from wavelength, so it does not modify the color of lensed galaxies. Therefore, gravitational magnification was not considered in the galaxy color.

The software PEGASE.2 (Fioc et al. 1997¹) constructed the rest-frame SEDs of the galaxies and the software LePHARE², translated the SEDs in redshift and passed them through the filter to get their color.

¹ PEGASE.2 can be downloaded at <http://www2.iap.fr/pegase/>

² LePHARE can be downloaded at <http://www.cfht.hawaii.edu/~arnouts/LePHARE/LePHARE.html>

5.1 Softwares employed

5.1.1 PEGASE.2

“Project d’Etude des Galaxies Par Synthese Evolutive ” (Fioc et al. 1997) is a Software constructing restframe SED. It must be employed following these steps :

1. Choose an IMF and create some SSPs.
2. Choose a scenario of star formation (i. e.,SFH).
3. Synthesise the spectra.

PEGASE.2 is based on the stellar evolutionary tracks from the “Padova” group, extended to the thermally pulsating asymptotic giant branch (AGB) and post-AGB phases (Groenewegen & de Jong 1993). It is written in Fortran and uses the BaSeL 2.2 library of stellar spectra and can synthesize low resolution ($R = 200$) ultraviolet to near infrared spectra of Hubble sequence galaxies, as well as starbursts. The nebular component (continuum and lines) due to HII regions is roughly calculated and added to the stellar component. Depending on the geometry of galaxy (disk or spheroidal), the attenuation of the spectrum by dust is then computed using a radiative transfer code. PEGASE.2 takes into account light scattering from dust and gas.

5.1.2 LePHARE

“PHotometric Analysis for Redshift Estimate” (Arnouts S. & Ilbert 2011). Is a software initially created to estimate galaxies photometric redshift thanks to a SED fitting. In order to do this tasks, LePHARE needs to translate galaxy templates (here the PEGASE.2 outputs) in redshift and multiply them to the transmission curves of the utilized filters. Then a least square fit procedure compares the observed flux (F_{obs}) and its corresponding uncertainty (σ) with the flux from the template (F_{temp}). The χ to minimise in the algorithm is defined as:

$$\chi^2 = \sum_i \left(\frac{F_{obs,i} - sF_{temp,i}}{\sigma_i} \right)^2 \quad (5.1)$$

Where i refers to the band occupied for the analysis and s is the scaling factor. Usually s is defined as the mass of the galaxy in units of F_{temp} mass ($1M_{\odot}$ in PEGASE.2). But the user may define the relation between s and the galaxy mass. The factor s is chosen to minimize the χ^2 values ($d\chi^2/ds = 0$), which leads to:

$$s = \frac{\sum_j \frac{F_{obs,j} - F_{temp,j}}{\sigma_j}}{\sum_j \frac{F_{temp,j}}{\sigma_j}} \quad (5.2)$$

Where j refers to the band used for the scaling. Note that j can be different from i but by default, $i=j$. Once installed, LePHARE must be utilized as follows :

1. Read the SED input [run ./sedtolib -t G -c zphot.para].
2. Read the transmission curves of the filters employed [run ./filter -c zphot.para].
3. Translate in redshift the galaxies and pass through the filter [run ./mag_gal -t G -c zphot.para].
4. Make a SED fitting of some input catalogue with the previously computed templates, this task was not occupied in the present worked [run ./zphot -c zphot.para].

LePHARE can automatically read PEAGSE.2 output. Otherwise, it can read a spectrum of 2 columns : the wavelength (λ in Angstroms) and the corresponding flux $F_{\nu}(\lambda) = dF(\lambda)/d\nu$. It translates galaxies in redshift using the IGM opacity in (Madau et al 1995). The opacity were previously integrated in redshift and stored as IGM transmission curves in the restframe of the emitting galaxy³. These IGM transmission curves were synthesised up to $\lambda = 1215$ and to redshift 8. They are expected to be multiplied (after wavelength interpolation) to the rest-frame spectrum of the galaxy. An example of an IGM transmission curve is visible in Figure 5.1.

³ The opacity curves are stored in LePHARE_dev/opa repertory

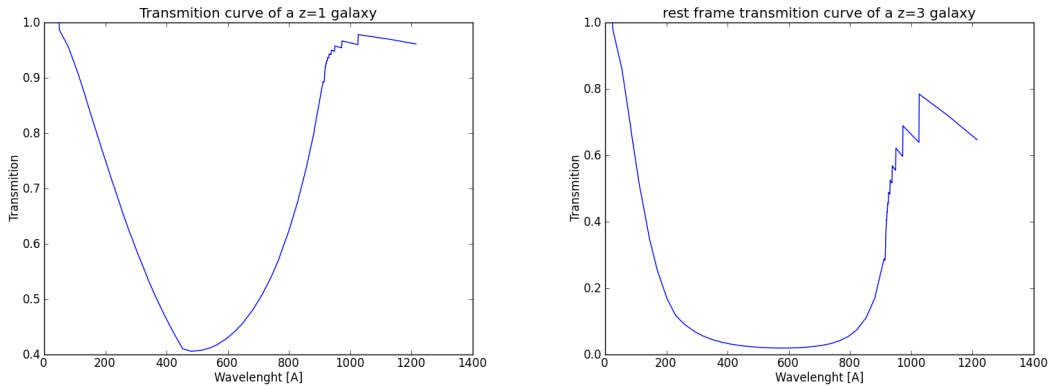


Figure 5.1: The IGM transmission spectra for a source located at $z=1$ (left) and $z=3$ (right). This spectra is the neutral Hydrogen absorption integrated along the line of sight and translated into the galaxies restframe. Is was computed using (Madau et al 1995) as a model for absorption. Note that for $z<1$, the DLAs dominate the absorption (Khare et al 2007) but they are not considered here.

5.2 Models

5.2.1 Galaxies evolving with redshift

With PEGASE.2, galaxy theoretical SEDs were constructed with a Salpeter IMF for all epochs. Four exponentially decaying SFHs were considered, each one with a different characteristic time. The characteristic times employed were 0.5, 1, 2 and 20 Gyr. The 0.5 Gyr simulates a starburst and the 20 Gyr imitates a constant SFH. Actually, true starburst and constant SFR galaxies were modelled and, as expected, their colors looked very similar to the models with a characteristic time of 0.5 and 20 Gyr respectively. The galaxy SEDs were computed assuming a spherical extinction, all the other parameters utilized were the default ones:

- Close binary system fraction : 0.05
- Metallicity : starting from 0 and evolving in time.
- Infall : No

- Substellar object : No
- Galactic wind : No
- Nebular emission : Yes

PEGASE.2 synthesised for each SFH a set of SED for different ages. The modelled galaxies began to form stars at redshift 10, and then, they evolved with time according to their input SFH. For each redshift, the age of the galaxies was determined as difference between the age of the universe at this redshift and the age of the universe at redshift 10 (480 Gyr). Using a higher redshift would result in a redder color for high redshift galaxies because their stars would be older and it would not change the color term for $z \lesssim 3$ because the small difference in age redshift does not matter any more. The PEGASE.2 spectra of the closest age was occupied as the rest-frame spectra of the galaxy for this redshift.

Then the galaxies rest-frame SED were translated in redshift by LePHARE utilizing the IGM opacity defined in (Madau & al 1995). The colors of the galaxies were measured by LePHARE passing the observer frame SEDs through the transmission curves of the occupied filters previously given as inputs. This procedure gave, according to their redshift, the colors of 4 galaxies born at $z = 10$. These colors are shown in Figure 5.2.

The Balmer and Lyman break shifts between the two filters and at $z \sim 2$ and $z \sim 6$ respectively. According to this figure, the color selections $I - H > 3.5$ and $R - H > 5$ permit to reject $z < 6$ interlopers which likely to be at redshift 2. However, a galaxy with a starburst at $z=10$ and without star formation after (i. e., with a SFH characteristic time of 0.5 Gyr), is highly improbable. Therefore, it can be assumed that such a galaxy would not be present for $z < 3$ because it would have evolved passively, without forming stars for 12 Gyr. It is like a instantaneous formation of the galaxy and no star formation afterwards.

Without considering this galaxy (the red curve with circles in Figure 5.2), the new color selection to exclude lower redshift interloper galaxies is thought $I - H - > 2.5$ and $R - H > 3.5$. Nevertheless, not all galaxies have an exponentially decaying SFH and overall, not all are born at $z=10$. The assumption of the exponentially decaying

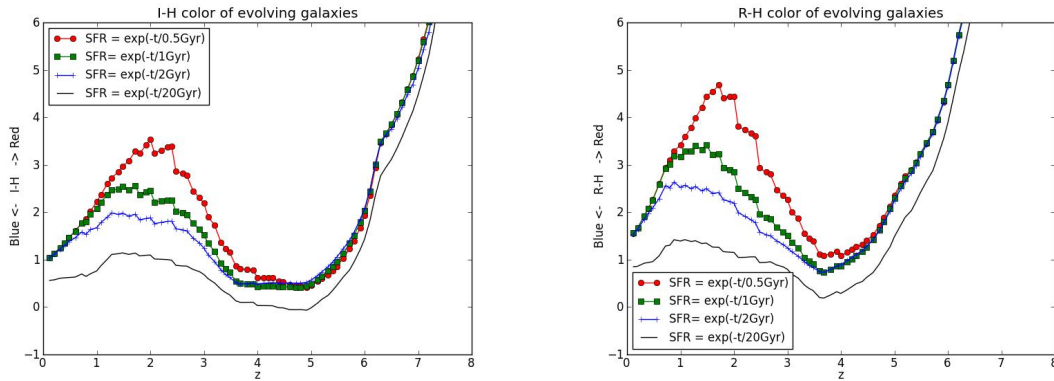


Figure 5.2: In function of redshift, the $I - H$ (left) and $R - H$ (right) colors of 4 galaxies with a different SFH but all born at $z=10$.

SFH shows the range of $I - H$ and $R - H$ colors of all the existing galaxies if galaxies initiating their SFH at all redshift are modelled. That is why more SEDs and colors were modelled considering for each redshift and SFH galaxies of different ages. The set of models evolving with redshift were computed to know the color of $z > 6$ galaxies, because these are very young : it is impossible to find a $z=6$ galaxy of 500Myr old which is the youngest age of the next model set.

5.2.2 Galaxies of different ages for each redshift

For each SFH presented above, 5 ages were considered : 0.2, 1, 2, 5 and 10 Gyr. This represented a total of 20 rest-frame SEDs. Then the 20 SEDs were translated in redshift from 0 to 8 by steps of 0.1 with LePHARE. For each redshift bin, LePHARE computed the $I - H$ and $R - H$ color of the observed frame SED. Figures 5.3, 5.4 and 5.5 show, as a function of redshift, the $I - H$ color without extinction, with extinction, and the $I - H$ color with extinction respectively. The extinction is computed by PEGASE assuming that gas and dust distribution is spherically symmetric. A good idea would have been to assume no dust extinction with PEGASE.2 and then to add attenuation with different E-B to get a good view of what happens: maybe attenuation from PEGASE.2 is not so representative of $z > 6$ target galaxies or $z < 6$ contaminant galaxies.

The models including extinction were always redder than the models not including

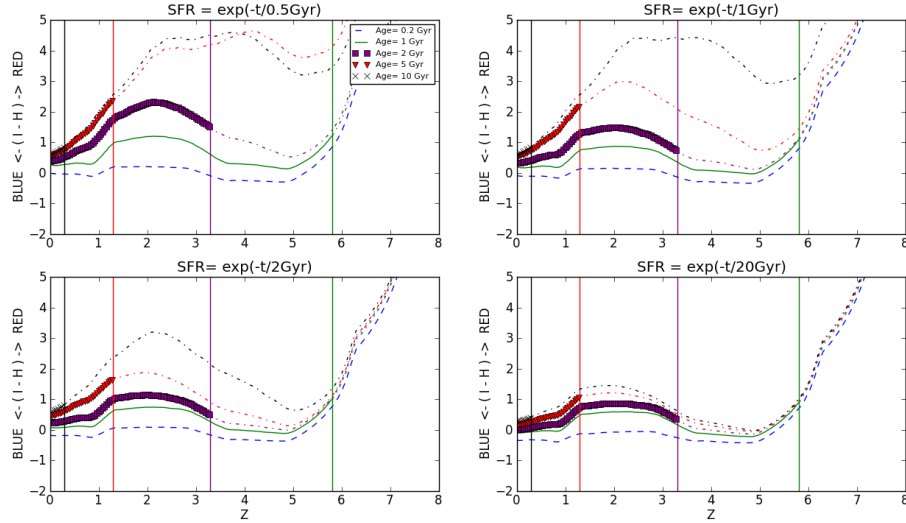


Figure 5.3: $I - H$ color versus redshift without extinction. For 4 different SFH models (sub-graph) and 5 different ages (color). The vertical lines is the redshift at which the age of the universe correspond to the age of the modelled galaxy. So for a younger universe (ie: higher redshift), such a galaxy cannot exist that is why it will be draw in a dotted line in these redshift. The SFH are: Up-Left: $\text{SFR} = \exp(-t/0.5\text{Gyr})$, Up-Right: $\text{SFR} = \exp(-t/1\text{Gyr})$, Down-Left: $\text{SFR} = \exp(-t/2\text{Gyr})$, Down-Right: $\text{SFR} = \exp(-t/20\text{Gyr})$. And the ages are 0.2, 1, 2, 5 and 10 Gyr. The older galaxies are always redder (i. e., higher curves in the plots).

extinction, especially for old galaxies because they have had much feedback yet and thus contain significant amount of dust. Dust and gas affect the bluer part of the spectrum and thermally emit photons in FIR. Therefore, extinction was expected to make colors redder. Moreover, dust can absorb in a wavelength range much wider than Hydrogen Balmer lines, and it has lot of energy levels (rotational, vibrational, electron levels) in which it can cool. That is why it is said that dust is an efficient cooler. Consequently, metals are making colors even redder. It was therefore expected to get models with extinction redder than dust-free models after feedback processes (i. e., after a certain age). Galaxies with extinction always appears redder than those without extinction at

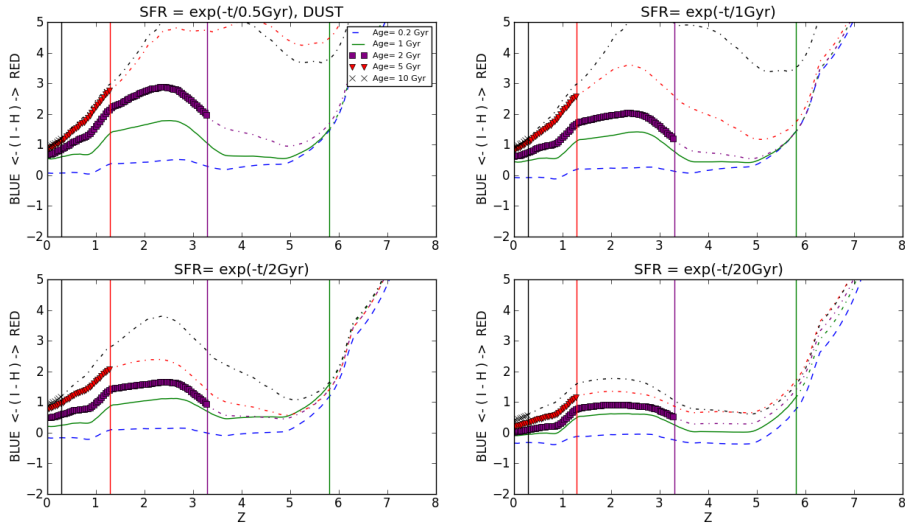


Figure 5.4: Same as 5.3 but with dust extinction.

least for wavelengths shorter than the dust thermal emission peak [$\sim 300K \sim 10\mu m$]. As the wavelength range considered is far from the dust and gas thermal emission, the main effect of extinction is to attenuate the blue side, making steeper the UV slope. The dusty models were employed to define the color selection because they are assuming redder contaminant galaxies and thus give a stricter selection and minimise the contamination from lower redshift galaxies.

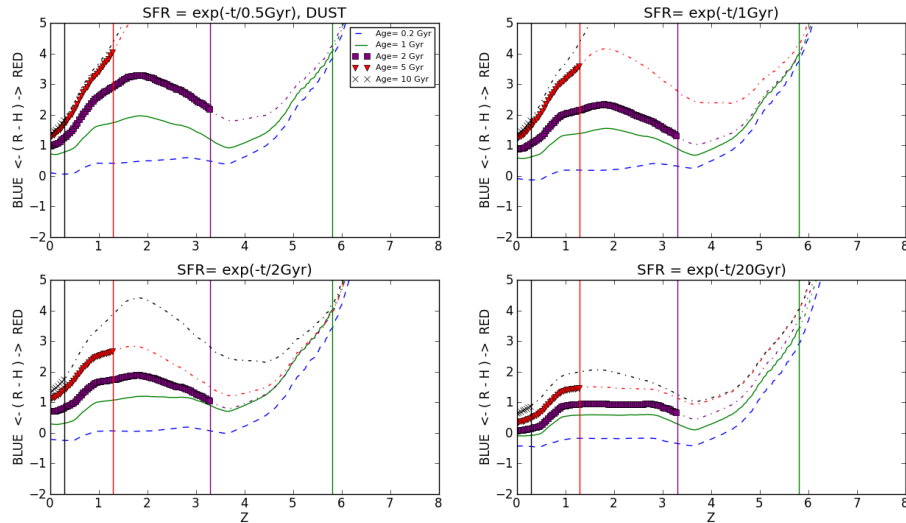
Note that metallicity changes the stellar state equation because it is increasing the mean molecular weight. In a star :

$$P = \frac{\rho}{\mu m_p} \quad (5.3)$$

Where P, ρ, μ, m_p, n are the pressure, density, mean molecular weight, mass of one proton and number density respectively. The mean molecular weight, μ is linked to Z, Y and X : the Hydrogen, Helium and metal fraction respectively with:

$$\mu \equiv \frac{\rho}{n m_p} \approx \frac{1}{2X + 0.75Y + 0.56Z} \quad (5.4)$$

Where a mean charge of 8 is assumed for metals. Higher metallicity decreases pressure, contracting the stellar core. An other main effect of metallicity is to increase the opacity



[!h]

Figure 5.5: Same as Figure 5.4 but for $R - H$.

of the stellar content and consequently, for the same core operating power, and hence, luminosity, higher metallicity makes the star colder (redder), but bigger.

Old galaxies have passed through many feedback processes and hence, they have a higher metallicity. Metallicity makes stars appear redder and increases the extinction. In addition, old galaxies have an old stellar population intrinsically red.

It is clear that while considering high z objects to select $z \sim 6$ galaxies, lower redshift contaminants are likely to be old metal rich galaxies, which are expected to be ellipticals.

According to the color-redshift dusty figures: Figure 5.4 and 5.5, objects with $I - H > 2.5$ and $R - H > 4$ are expected to be galaxies at $z > 6$ without too much contamination from lower redshift interlopers. These contaminants are likely to be $z \sim 2$ galaxies with a low characteristic time of SFH (i. e., a fast decaying SFR), and a high age. They are thought to be elliptical galaxies. Other works (Bouwens et al 2006; Overzier et al 2007) also found elliptical (old) galaxies with $z = 2$ as major contaminants for the dropout search technique even if they utilized different bands. Note that, 5 Gyr galaxies with a SFH characteristic decaying time of 0.5 Gyr is highly improbable to exist as explained

because it would mean that these galaxies formed lots of stars at the beginning of their life and evolve passively, without forming any significant star afterwards. If they would exist, these galaxy would be, of course, very red and they would be low redshift interlopers. But as they are unlikely to exist, the major source of contamination remains the elliptical galaxy with a fast SFH but not starbursts.

Figure 5.6 aims to explain the tendency of the color curves in Figure 5.3: it presents the SED of typical spiral galaxy ⁴, translated in redshift without evolution. The typical feature of this SED is the strong break at 4000 Å. This break is shifted around I filter at $z \simeq 2$. That is why we see an empty region in $I - H$ or $R - H$ color in Figure 5.3. This 4000 break is caused by the blanket absorption of high energy radiation from metals in stellar atmospheres, from the H_∞ absorption of Hydrogen atoms and from a deficiency of hot, blue stars in the galaxy. In this break, the Ca H and K lines (3934Å and 3969Å), the G-band (4304Å), and Mg (5175Å) and Na (5894Å) lines are present. These are absorption lines due to metals. The Balmer lines are also present : $H\alpha$: 6563 Å; $H\beta$: 4861 Å; $H\gamma$: 4340 Å; $H\delta$: 4103 Å and the Balmer break at 3650 Å. These lines are seen in absorption in old stellar population. A closer look on the restframe 4000 Å break is illustrated Figure 5.7.

With only 2 bands, the LBG selection is likely contaminated. But as 3 bands were considered, a color-color diagram were computed in Figure 5.8. It shows that a stricter selection in $I - H$ or $R - I = (R - H) - (I - H)$ can be setted. Selecting galaxies with $R - I > 2$ does not exclude any $z=6$ galaxies and kicks out some early-type $z=2$ galaxies from the selection. Some red stars may also disappear from the selection thanks to this stricter selection. With 3 filters, the selection seems to be safer. Indeed, at $z=6$, the Balmer break is shifted to $1215 \times (1 + 6) = 8505\text{Å}$ and the Lyman break to $912 \times 7 = 6384\text{Å}$. So the R_{650} flux vanishes and the I_{800} flux drops because of IGM neutral Hydrogen absorption.

⁴7 Gyr old; $A_v=0.3$; $Z=0.02$

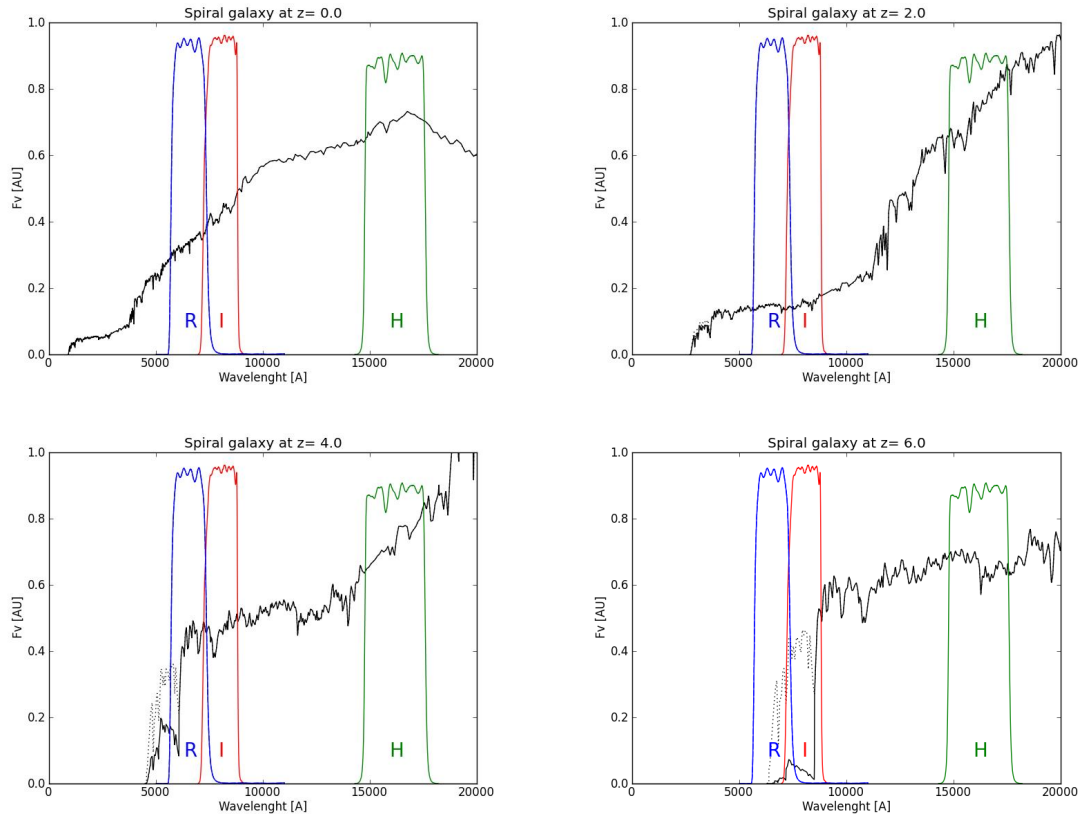


Figure 5.6: The SED of a 7 Gyr Spiral galaxy with $Z=0.02$ and $A_v=0.3$ from GISSEL 96. It is redshifted without evolution at redshift 0 (top left); 2 (top right); 4 (bottom left) and 6 (bottom right). In dashed line, the SED is drawn if no extinction for IGM is applied. Extinction is calculated from (Madau et al 1995). You can see that at redshift 0, the SED slope is steeper in the neighbourhood of I than in the neighbourhood of H : the galaxy is getting redder in $I - H$ while increasing the redshift. Whereas around $z=2$, the slope around I band is quite flat although it is very steep around H . It is steep around H due to the 4000 \AA that is redshifted to the H band. So while increasing the redshift, the $-$ color is decreasing, the galaxy becomes bluer while being redshifted.

5.2.3 Galaxy angular size

From the modelled color, discriminating between a I dropout at $z \sim 6$ and a red galaxy at $z \sim 2$ is not an obvious task. A basic idea comes to mind: the farther, the fainter and

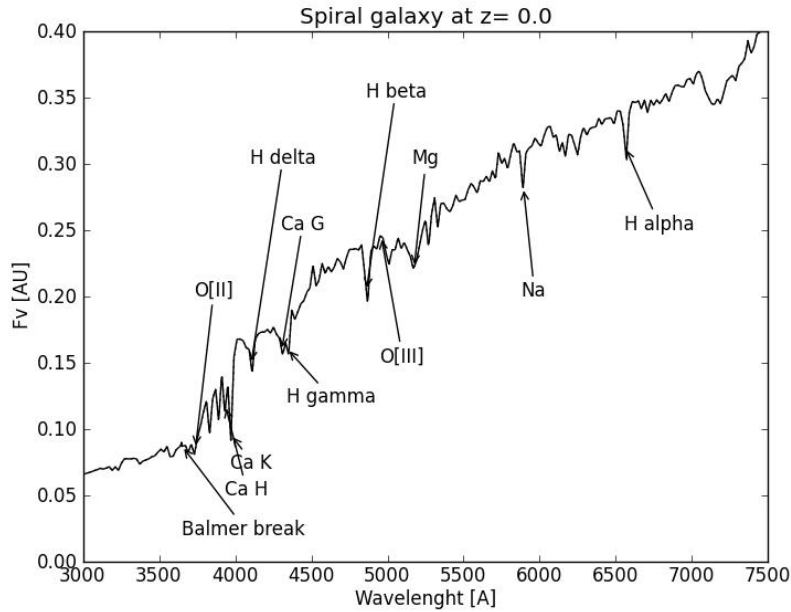


Figure 5.7: The 4000 Å for the same SED as 5.6 (Spiral galaxy). Most of the lines are seen in absorption. And we have strong metal absorption lines demonstrating the old stellar content of this galaxy.

smaller. So, both the apparent size and luminosity of a typical galaxy were estimated. Figure 5.9 exposes the apparent size of a galaxy of 10 kpc and an absolute magnitude of -20 in function of its redshift. Calculating the rest-frame absolute magnitude of a galaxy from its observed fluxes is a procedure commonly performed. The redshift observed in one band can be shifted to the rest-frame corresponding band, like in (Bouwens et al. 2006). The absolute magnitude is estimated with Equation 5.5. It enables to compare the measured fluxes to other works and other redshifts.

$$M_i = m_j - DM(z) - K(i, j) \quad (5.5)$$

Where M_i is the absolute magnitude in i band; m_j is the apparent magnitude in j band; $DM(z)$ is the distance modulus representing to the attenuation of the flux due to the distance between the source and the observer; and $K(i, j)$ is the K-correction, a color term due to the mismatch between the the observer frame and the rest frame band

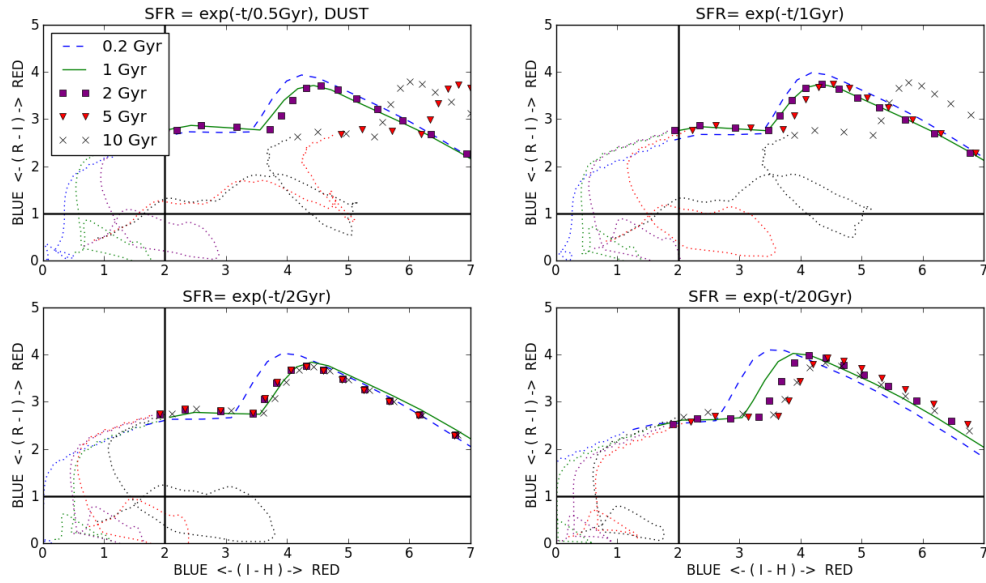


Figure 5.8: Color color diagram of the same galaxies as previous color redshift diagram. The track is following the galaxy in redshift. For $z < 6$, the color of the galaxies are drawn in dotted line. Colour and symbol convention are the same as Figure 5.3. The horizontal and vertical line represents the initial color selections. $R - H$ can be increased to values as high as 2 without losing $z=6$ galaxies.

shape.

Figure 5.9 represents the apparent magnitude and size of a typical galaxy. The magnitude were estimated neglecting the k-correction because this factor depends on the assumed spectral slope of the the object near the observed band and on the corresponding rest frame band depending on the redshift.

The angular size of a $z=6$ galaxy is not even the double of a $z=1$ galaxy. Considering that $z=6$ young star forming galaxies are expected to be smaller than old red galaxies ($\sim 0.75kpc$, Finlator et al 2010), it is impossible to select $z=6$ galaxies according to their angular size. However, this information (the apparent size) may permit to discriminate galaxies from stars.

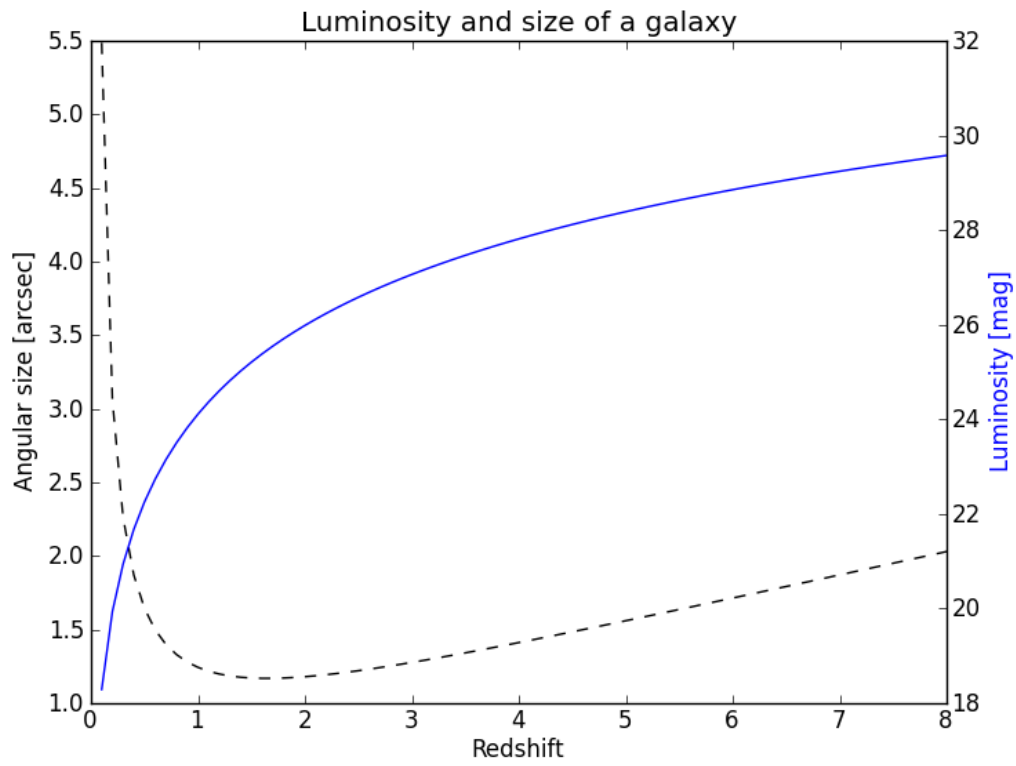


Figure 5.9: Apparent size and luminosity of a 10 kpc galaxy of absolute magnitude -20 mag. This luminosity does not take into account the k-correction.

5.2.4 Stars

The colors of some nearby stars were also determined to assess the possible contamination rate from stars if the selection is independent from the shape of the object. The reference SEDs employed were taken from (Pickles 1998⁵). They were constructed with stacked spectroscopy: the best quality spectra of objects with the same spectral type, luminosity class, and metal abundance were combined to get a high S/N composite SED. The SED dataset is composed of 131 spectra encompassing all spectral types (from O to M) and luminosity class (from V to I) at solar metallicity. The dataset also contains metal weak and metal rich F,K dwarf and G,K giant components. The absolute bolometric luminosity is also given with each SED.

The magnitude in each band were computed from the SED and the filter transmission curve⁶. The difference of magnitude gave the color of each objects. These colors are displayed with the bolometric luminosity of the SED as a CMD in Figure 5.10.

Over the variety of stars considered, the stellar $I - H$ and $R - I$ color remains inferior to 2.5 and 2 respectively. Furthermore, only few objects are redder than $I - H = 1$ and $R - I = 1$. Consequently, the color selection, $I - H > 2.5$ and $R - I > 2$ excludes all the stars supposing that there is no disk around them.

There is a faster way to see which stars may be red enough to contaminate the selection: stars can be approximated to black bodies. The measured flux of a star at a certain wavelength is proportional to the spectral radiance defined by the Planck law :

$$B_{\lambda}(T, \lambda) = \frac{2hc^2}{\lambda^2} \frac{1}{e^{\frac{hc}{\lambda k_B T}} - 1} \quad (5.6)$$

$$B_{\nu}(T, \lambda) = \frac{\lambda^2}{c} \times B_{\lambda}$$

Where λ , T , k_B , c , and h are the wavelength, effective temperature, Boltzman constant, light velocity, and Planck constant respectively. As a first approximation, the flux in

⁵ article presents at <http://www.jstor.org/stable/10.1086/316197>

⁶ After being interpolated to the filter wavelength vector, the SED were multiplied by the transmission vector. The components of the resulting vector were summed. Next the previous sum was divided by the sum of the components of the transmission vector. This gave an arbitrary flux.

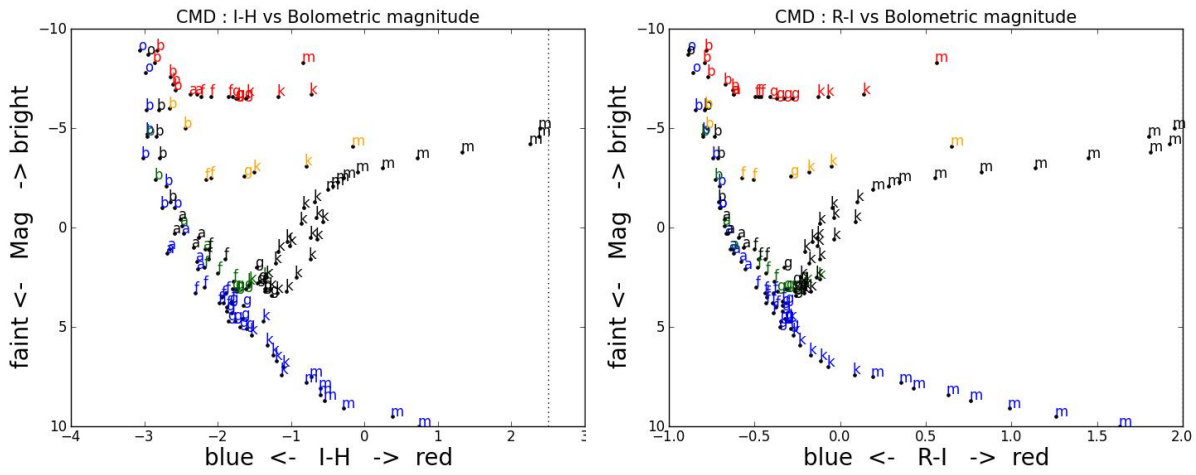


Figure 5.10: CMD : The color $I - H$ (left) and $R - H$ (right) of the composite stellar SED from (Pickles 1998) against their bolometric magnitude. The letter of each star represents its spectral type and the color represents its luminosity class: blue, green, black, orange, red for V, IV, III, II, and I respectively.

a band is considered as the flux in its central wavelength. So the color between two wavelength λ_1 and λ_2 is :

$$mag(\lambda_1) - mag(\lambda_2) = -2.5 \times \log \left(\frac{B_\nu(T, \lambda_1)}{B_\nu(T, \lambda_2)} \right) \quad (5.7)$$

A star with effective temperature: $T=3000^\circ$ has a spectral radiance:

$$\begin{aligned} B_\nu(3000, 1.60[\mu m]) &= 5.4 \times 10^2 \frac{erg/Hz}{s/m^2} \\ B_\nu(3000, 0.80[\mu m]) &= 2.1 \times 10^2 \frac{erg/Hz}{s/m^2} \\ B_\nu(3000, 0.65[\mu m]) &= 1.0 \times 10^2 \frac{erg/Hz}{s/m^2} \end{aligned} \quad (5.8)$$

And so this stars has colors $I - H = 1.03$ and $R - I = 0.81$. Actually, to have $I - H = 2.5$, a black body needs an effective temperature of 2000° K, and to have $R - I=2$, its effective temperature needs to be 1600° K. Therefore these stars do not contaminate the color selection. However, brown draft and extinguished stars (with an accretion disk for example) are not modelled. Therefore a careful visual check were performed to determine if the source is resolved on the $0.5''$ images.

Chapter 6

Results

Pichintu mongel paniewllelaiai.

“Time is so short, will we meet again ?”

In this section, the main results are described. The reader should remember that the goal of this work was to find some LBG at redshift 6 according to their $I - H$ color. Some fields contained R band photometric data. For these fields, the selection was better constrained using both $I - H$ and $R - H$ color. Some color magnitude diagram (CMD) were computed, to have a view of the full data set. The objects selected from their color were examined visually and some of them were discarded, due to their low S/N in the detection image, or because of their star-like, satellite or camera defects. A correlation function of the distance between the selected objects and the cluster center were computed.

6.1 Color Magnitude Diagrams

CMD were computed for both the $I - H$ and $R - H$ colors versus the H magnitude. Figure 6.1 and Figure 6.2 show the $I - H$ Vs H diagrams with $R - H$ as the displayed color of each data point. The diagrams are plotted for colors < 5 because then, the color is not well determined. In case of a non-detection, SExtractor returned a magnitude of 99. For each object detected, angular the distance to the foreground cluster center

determined by eye, was also measured and displayed in the diagrams in order to show the red sequence.

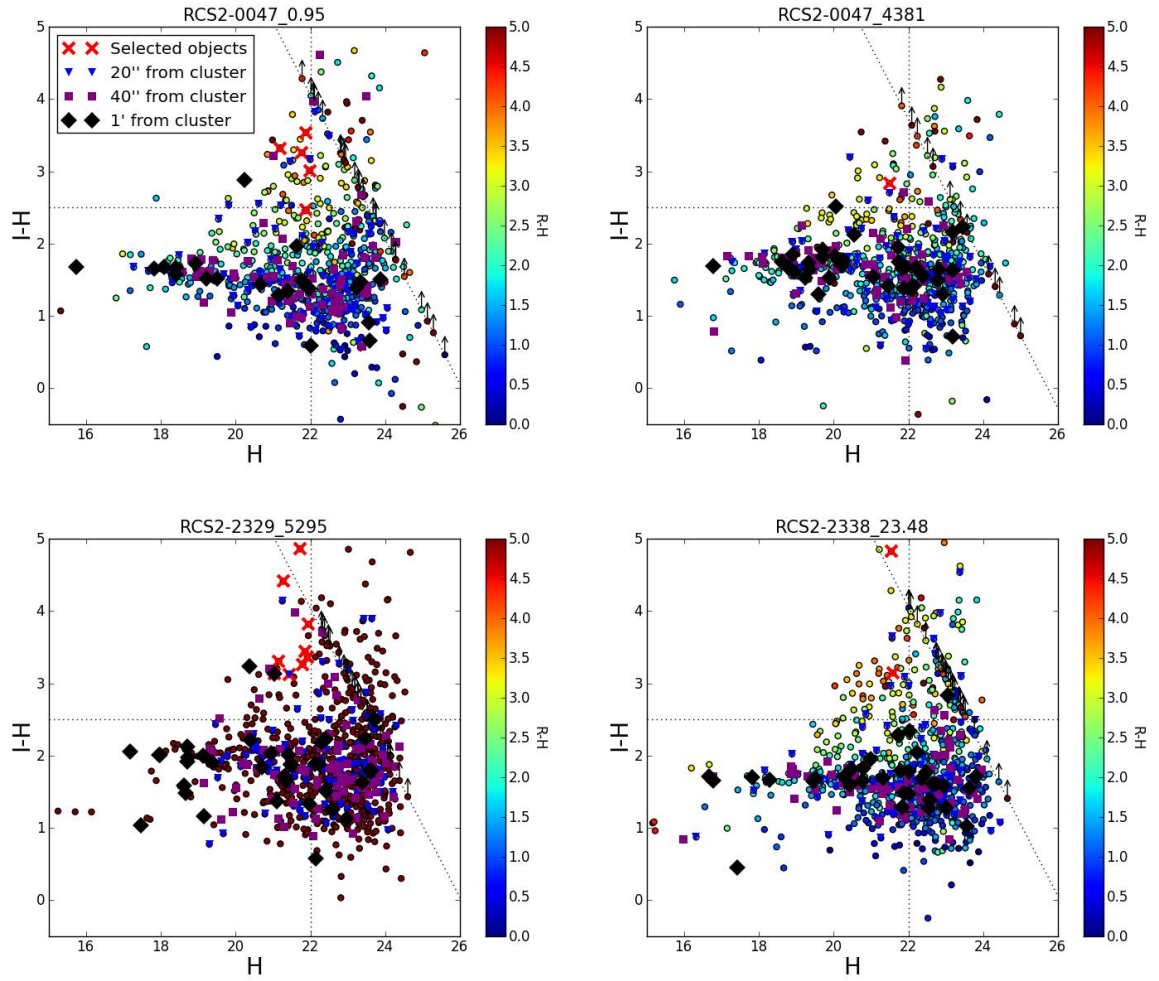


Figure 6.1: CMD of 4 RCS2 pointings: $I-H$ color versus H mag. The $R-H$ color is represented by the displayed color of each point: from blue ($R-H=0$) to red ($R-H=5$). The selected objects are marked with a red cross. The horizontal and vertical dashed lines represent the color and magnitude limits respectively. The diagonal line represents the I band 80% detection limit and the data points with arrows are objects with a I band flux not determined. To show the red sequence, some symbols are over-plotted to each data point: a black diamond for object closer than 20'' from the cluster center, a purple square for objects between 20 and 40'' away from the cluster center and a blue triangle for objects between 40'' and 60'' away from it. Note that the black diamond are mostly aligned: this is the “red sequence”.

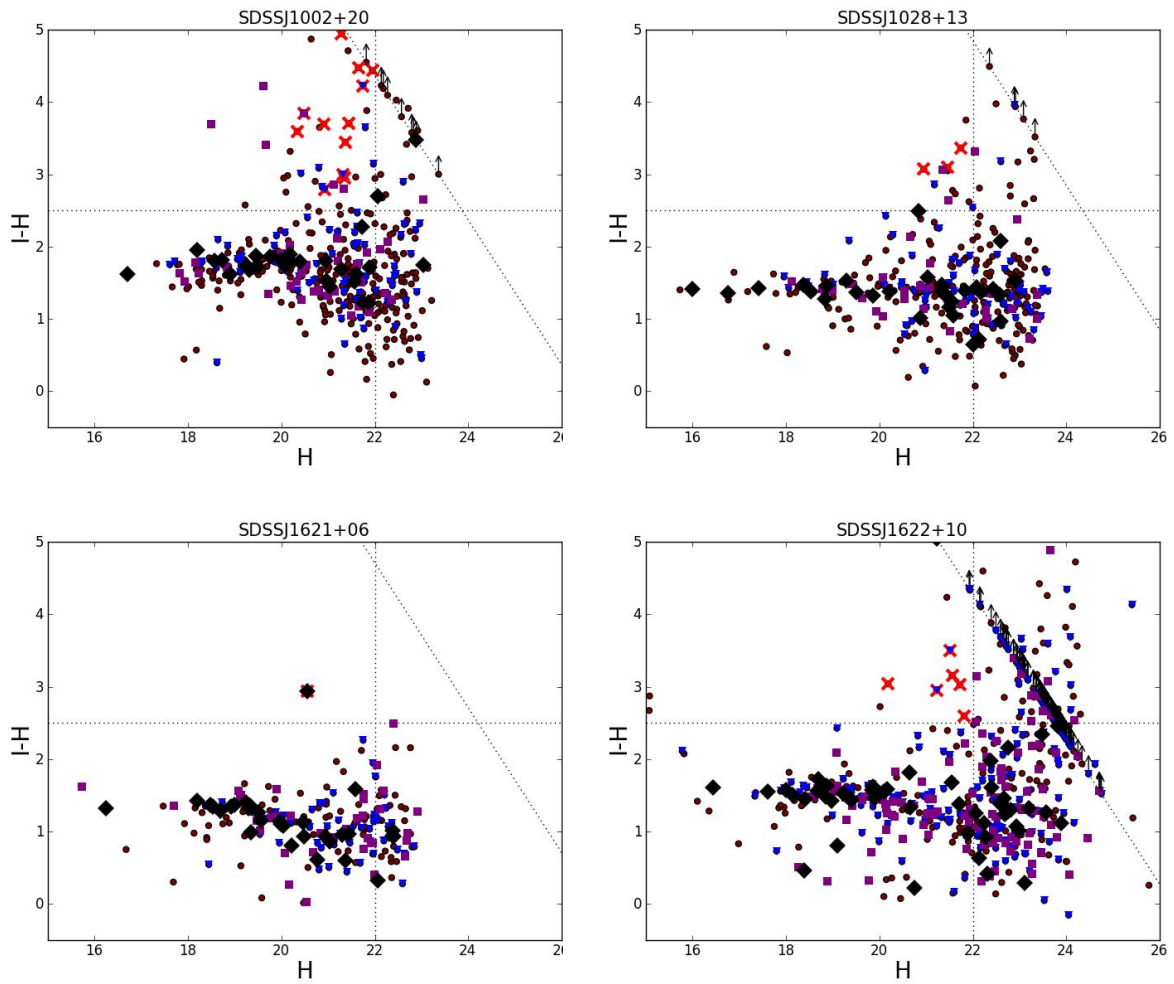


Figure 6.2: Same as Figure 6.1 for 4 SDSS pointings. There is no color scale because the photometric dataset of SDSS pointings only contains H and I band data.

6.2 Candidates

Snapshots of the $z \sim 6$ galaxies detected with the Lyman break technique are presented below. And then, tables with the coordinates and the magnitude in each band of the candidate is exposed. The magnitude was not measured from HST images due to a lack of time.

6.2.1 RCS2 objects

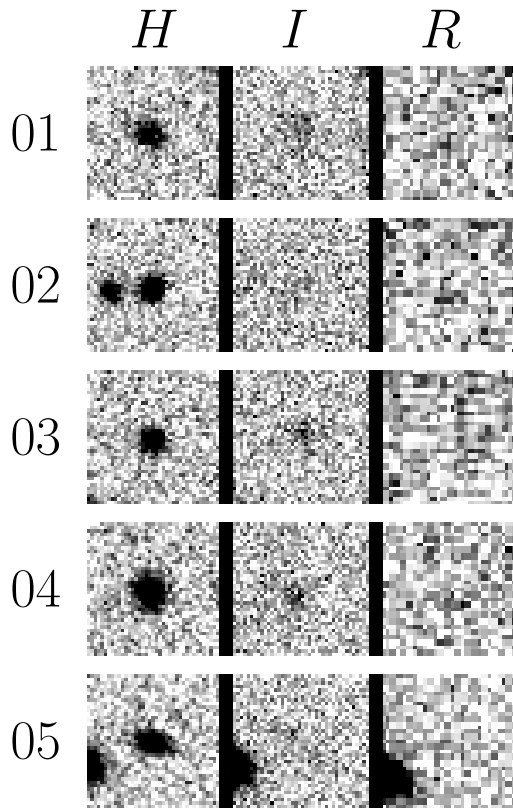


Figure 6.3: RCS2J0057.3+0209

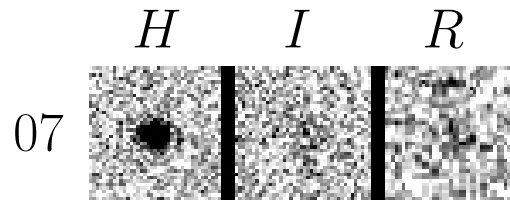


Figure 6.5: RCS2J0047.5+0508

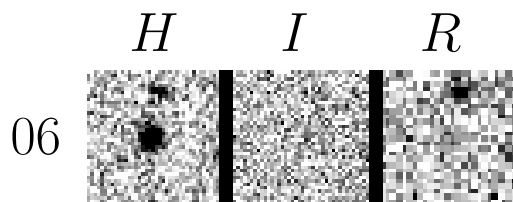


Figure 6.4: RCS2J0052.1+0434

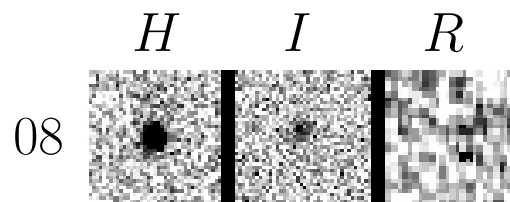


Figure 6.6: RCS2J0034.3+0225

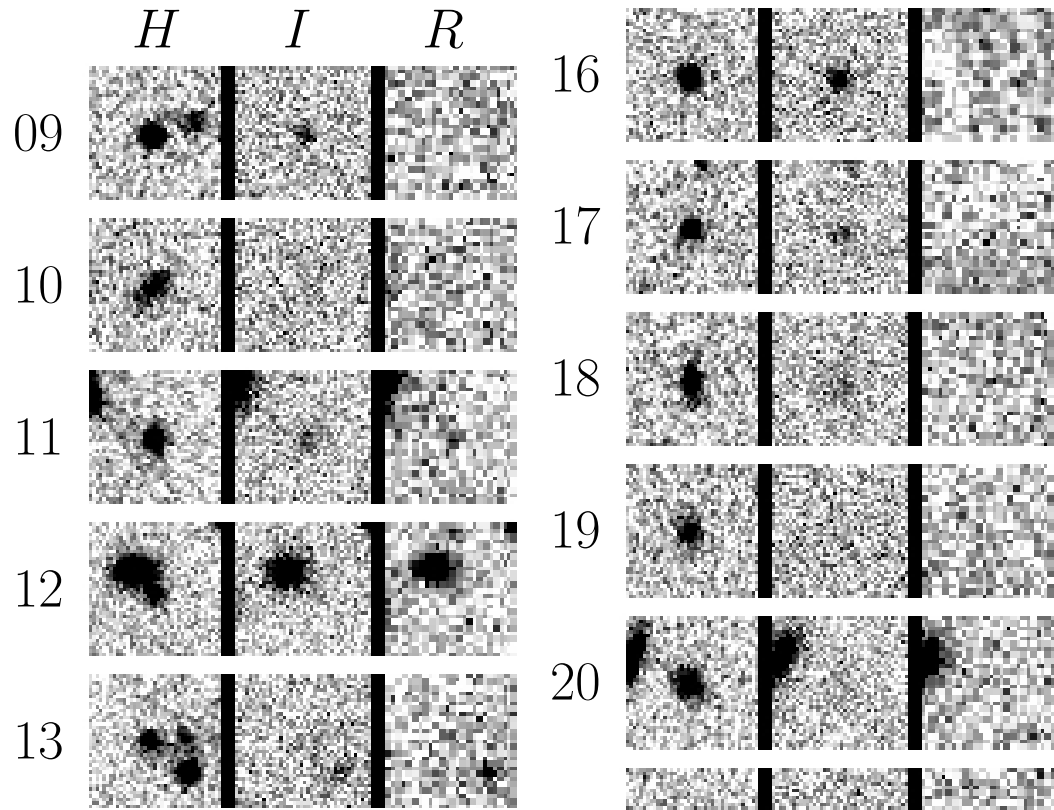


Figure 6.7: RCS2J2111.2-0114

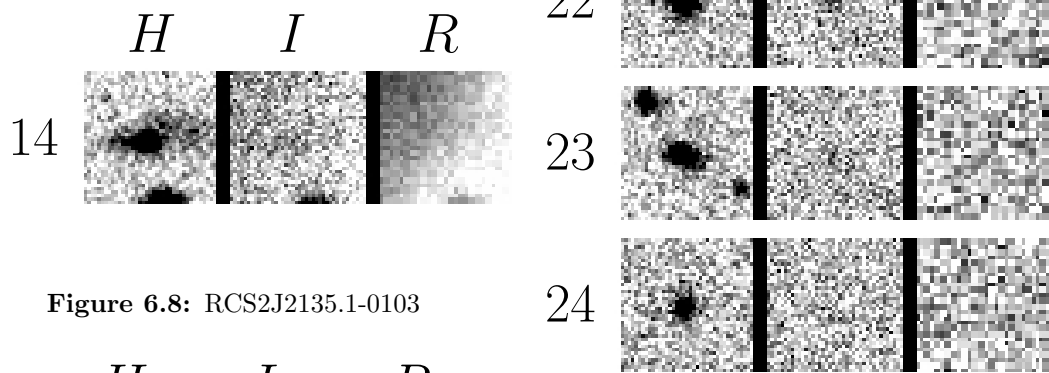
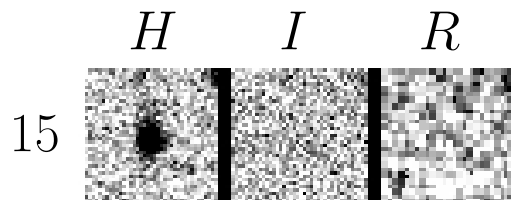


Figure 6.8: RCS2J2135.1-0103



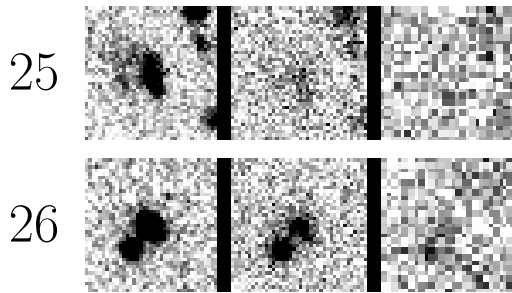


Figure 6.9: RCS2J2147.4-0102

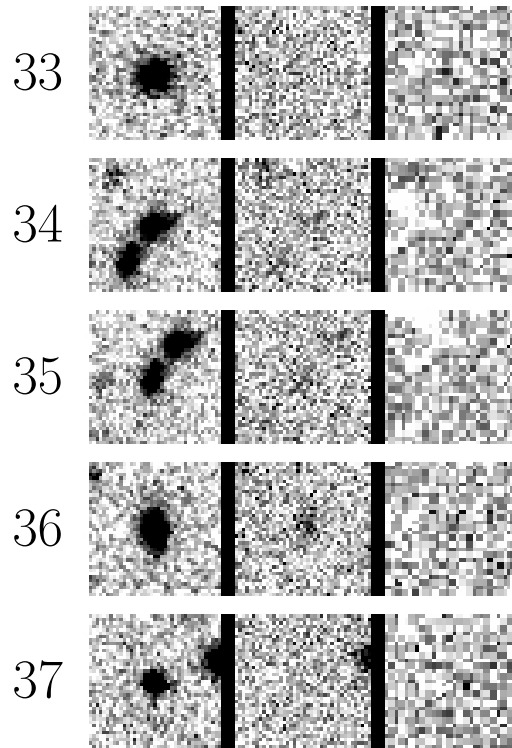
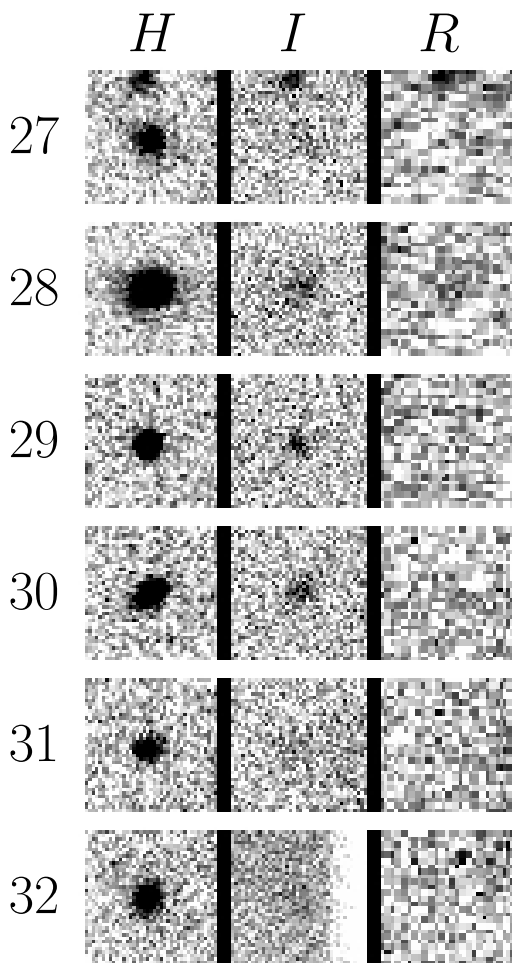
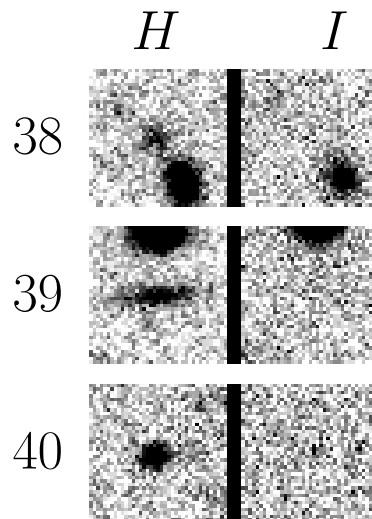
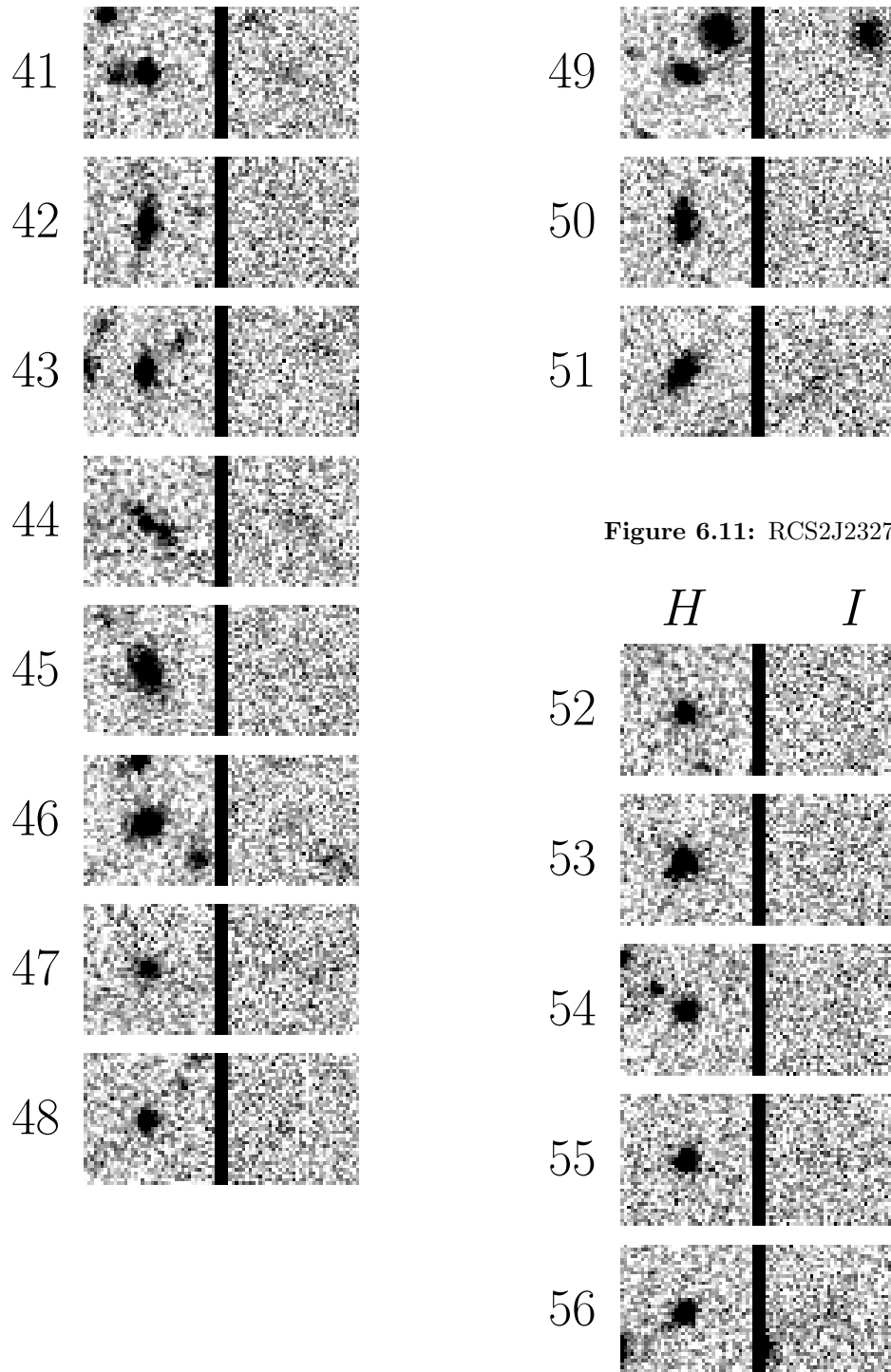


Figure 6.10: RCS2J2151.3-0139





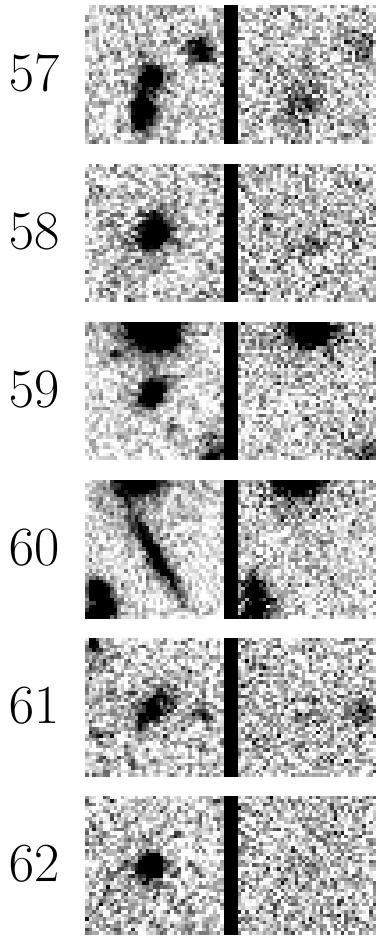


Figure 6.12: RCS2J2329.5-0121

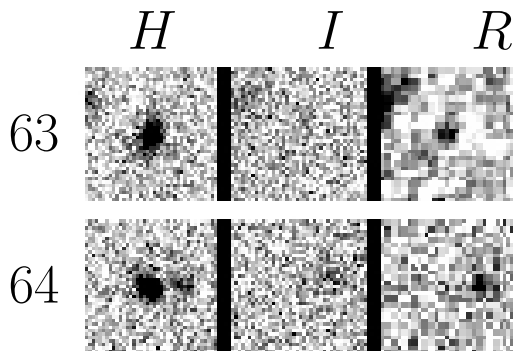


Figure 6.13: RCS2J2329.1-1318

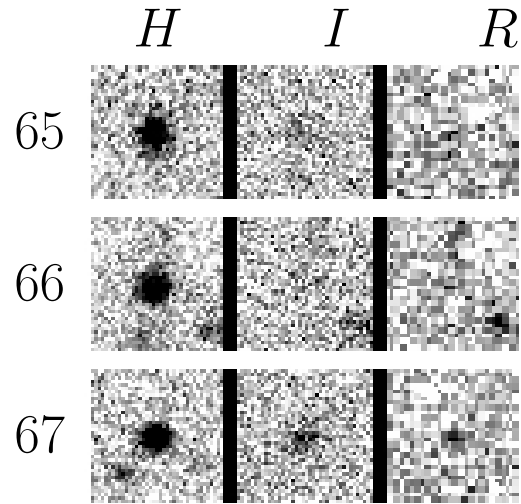


Figure 6.14: RCS2J2336.2-0609

N	RA (J2000)	Dec	H	I	R	Distance ["]	Priority
01	14.37853	2.11621	21.9	24.4	26.7	153	A
02	14.36064	2.12789	21.9	25.4	132.9	104	B
03	14.36277	2.13304	22.0	25.0	132.9	85	A
04	14.34780	2.17351	21.2	24.5	29.7	87	A
05	14.36281	2.17354	21.8	25.0	132.9	61	A

Table 6.1: RCS2J0057.3+0209: Each line describes a LBG candidate. The first column represent its sequence number, corresponding to the snapshots displayed above; the second and third columns give the sky position of the candidate in degrees J2000; the 4th, 5th and 6th columns are the magnitude in AB system in the H , I and R band respectively, a magnitude brighter than 99 means that the magnitude could not be measured; the 7th column is the measured distance to the foreground center (located by eye) in arcsec. and the last column informs the priority of observation (A for high priority C for low priority) based on a personal judgement relying only brightness, colour and angular distance to foreground cluster.

N	RA (J2000)	Dec	H	I	R	Distance ["]	Priority
06	13.04827	4.56189	21.7	25.4	27.7	25	A

Table 6.2: RCS2J0052.1+0434

N	RA (J2000)	Dec	H	I	R	Distance ["]	Priority
07	11.98170	5.17218	21.2	24.6	27.0	139	A

Table 6.3: RCS2J0047.5+0508

N	RA (J2000)	Dec	H	I	R	Distance ["]	Priority
08	8.63670	2.39797	21.5	24.3	26.4	113	A

Table 6.4: RCS2J0034.3+0225

N	RA (J2000)	Dec	H	I	R	Distance ["]	Priority
09	317.85330	-1.23302	21.2	24.5	27.5	80	A
10	317.84681	-1.23311	21.5	24.4	27.1	57	A
11	317.84559	-1.23785	21.2	24.3	26.3	51	B
12	317.84582	-1.21611	21.8	24.4	27.4	90	B
13	317.85312	-1.21160	21.8	132.9	132.9	119	B

Table 6.5: RCS2J2111.2-0114

N	RA (J2000)	Dec	H	I	R	Distance ["]	Priority
14	323.78183	-1.03941	20.5	132.9	132.8	76	A

Table 6.6: RCS2J2135.1-0103

N	RA (J2000)	Dec	H	I	R	Distance ["]	Priority
15	326.89298	-1.07333	21.3	24.6	131.2	106	A
16	326.89167	-1.05630	20.9	23.4	26.7	58	B
17	326.89674	-1.04893	21.3	24.5	27.7	29	B
18	326.89816	-1.04092	21.7	24.0	27.2	29	A
19	326.90686	-0.99548	22.0	25.0	131.2	183	A
20	326.89057	-1.02694	21.6	24.3	131.2	85	B
21	326.89595	-1.02784	21.4	25.1	131.2	73	A
22	326.87851	-1.03265	21.1	23.8	25.9	105	A
23	326.89629	-1.02935	21.2	24.6	131.2	67	A
24	326.91516	-1.00375	21.9	26.4	131.2	158	A
25	326.90175	-1.02942	20.9	23.1	131.2	61	A
26	326.89196	-1.01056	20.6	22.6	24.8	136	C

Table 6.7: RCS2J2147.4-0102

N	RA (J2000)	Dec	H	I	R	Distance ["]	Priority
27	327.85831	-1.66401	21.7	24.9	131.2	62	A
28	327.85720	-1.66118	20.4	22.7	131.2	51	A
29	327.85497	-1.66011	21.3	23.3	131.2	47	A
30	327.85525	-1.59566	20.9	23.3	25.9	185	B
31	327.87722	-1.59565	21.9	24.2	131.2	200	B
32	327.83051	-1.60152	21.7	23.8	131.2	187	B
33	327.86660	-1.62958	21.3	24.1	131.2	74	A
34	327.86952	-1.63221	21.6	24.2	131.2	73	A
35	327.86985	-1.63266	21.7	24.2	131.2	72	A
36	327.86039	-1.62185	21.2	23.6	27.0	92	A
37	327.84669	-1.60803	21.9	26.7	131.2	144	B

Table 6.8: RCS2J2151.3-0139

N	RA (J2000)	Dec	H	I	R	Distance ["]	Priority
38	351.87642	-2.10362	21.8	25.1	99.9	114	C
39	351.86425	-2.10237	21.3	132.9	99.9	102	A
40	351.86285	-2.09925	21.8	25.7	99.9	91	A
41	351.89635	-2.09895	21.5	25.6	99.9	144	B
42	351.84920	-2.07956	21.8	25.4	99.9	60	A
43	351.89565	-2.07683	21.7	132.9	99.9	110	A
44	351.86078	-2.06535	21.8	23.9	99.9	34	B
45	351.83924	-2.06444	21.1	25.5	99.9	98	A
46	351.88687	-2.06010	21.2	28.6	99.9	92	A
47	351.86974	-2.00782	21.7	25.1	99.9	238	A
48	351.89320	-2.02934	22.0	25.8	99.9	189	A
49	351.87631	-2.03260	22.0	132.9	99.9	153	B
50	351.83870	-2.03923	21.8	26.0	99.9	156	B
51	351.88556	-2.04631	21.5	24.5	99.9	123	B

Table 6.9: RCS2J2327.3-0204

N	RA (J2000)	Dec	H	I	R	Distance ["]	Priority
52	352.45272	-1.39484	21.8	29.1	99.9	173	A
53	352.43439	-1.37830	21.3	25.7	99.9	125	A
54	352.43361	-1.37661	21.9	25.8	99.9	120	A
55	352.42856	-1.37648	21.7	26.6	99.9	129	A
56	352.45411	-1.36272	21.4	24.6	99.9	59	A
57	352.47685	-1.36106	21.9	25.3	99.9	112	B
58	352.41924	-1.34038	21.2	24.5	99.9	110	B
59	352.43421	-1.34675	21.4	26.8	99.9	54	A
60	352.45192	-1.34915	21.0	24.2	99.9	12	A
61	352.43060	-1.33136	21.9	25.3	99.9	88	B
62	352.41733	-1.32169	21.8	25.1	99.9	147	A

Table 6.10: RCS2J2329.5-0121

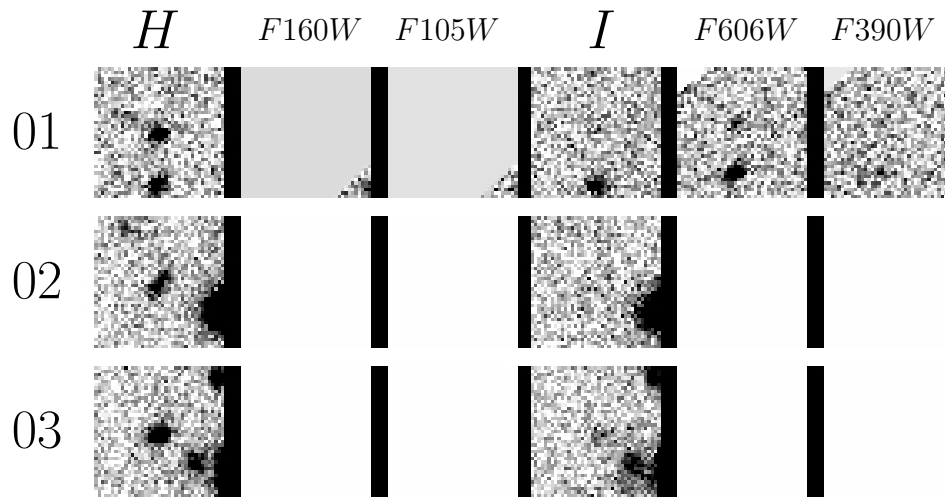
N	RA (J2000)	Dec	H	I	R	Distance ["]	Priority
63	352.26895	-13.31845	21.6	24.7	27.0	108	C
64	352.27698	-13.27563	21.5	26.4	132.9	88	B

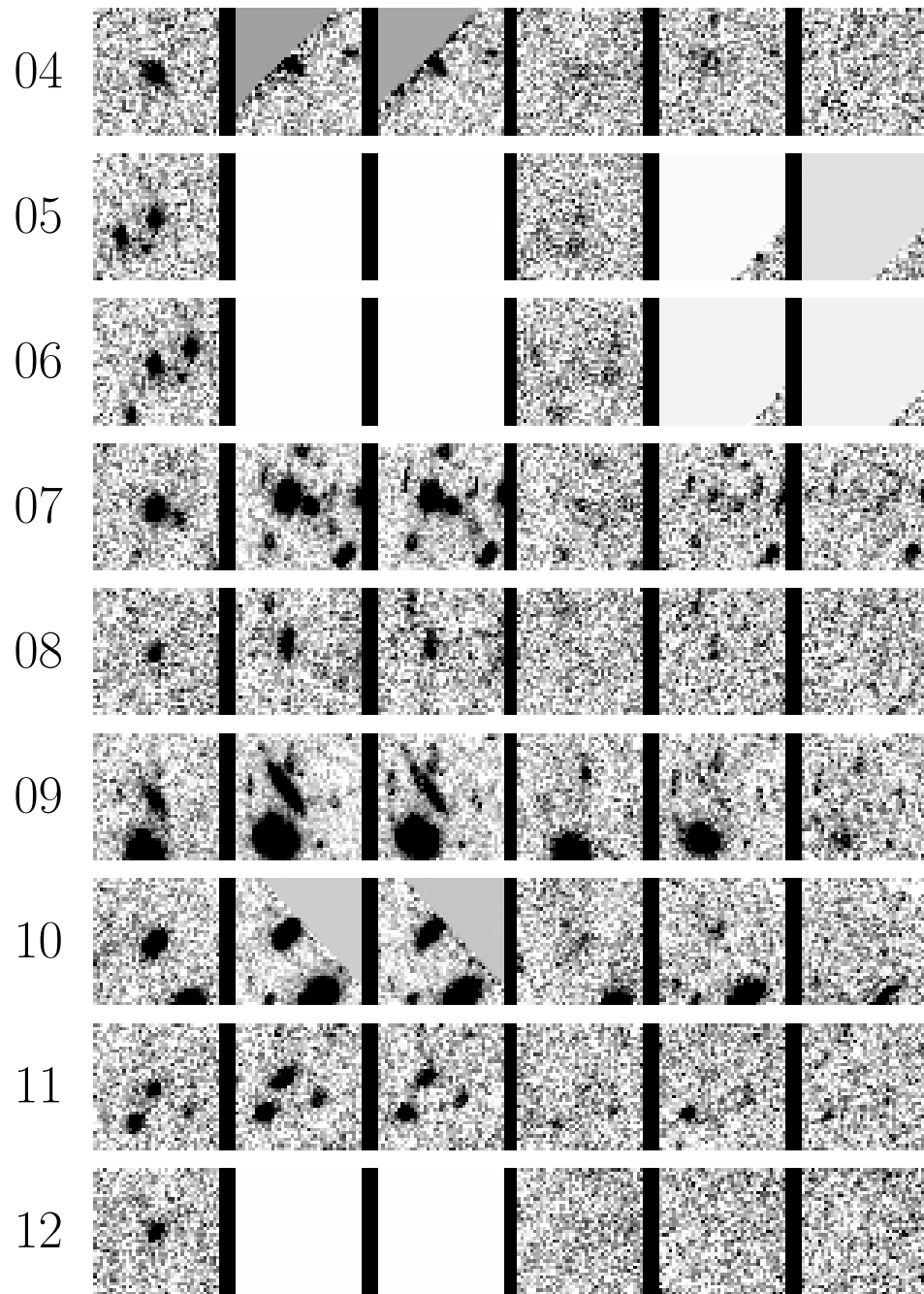
Table 6.11: RCS2J2329.1-1318

N	RA (J2000)	Dec	H	I	R	Distance ["]	Priority
65	354.09502	-6.09267	21.1	24.1	26.6	176	A
66	354.10698	-6.12996	21.2	26.6	132.8	75	A
67	354.10392	-6.10680	21.4	23.7	26.6	134	C

Table 6.12: RCS2J2336.2-0609

6.2.2 SDSS objects





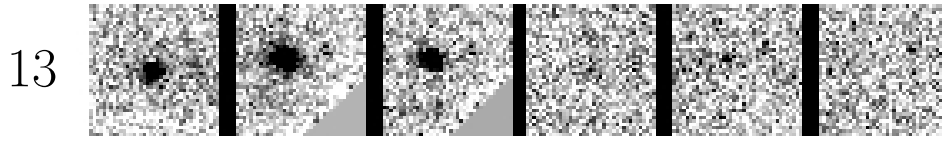


Figure 6.15: SDSSJ1002.3+2031

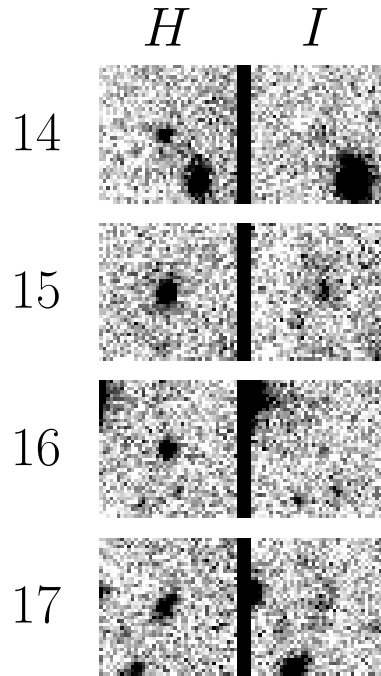
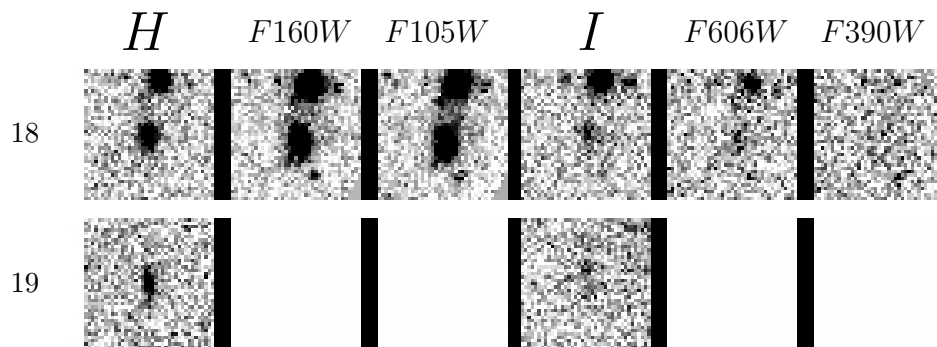


Figure 6.16: SDSSJ1028.0+1325



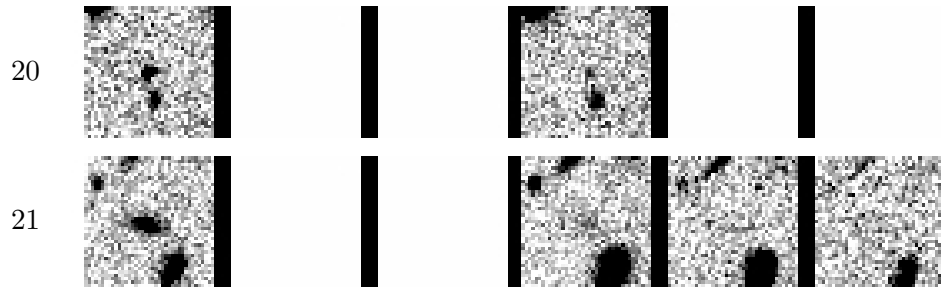
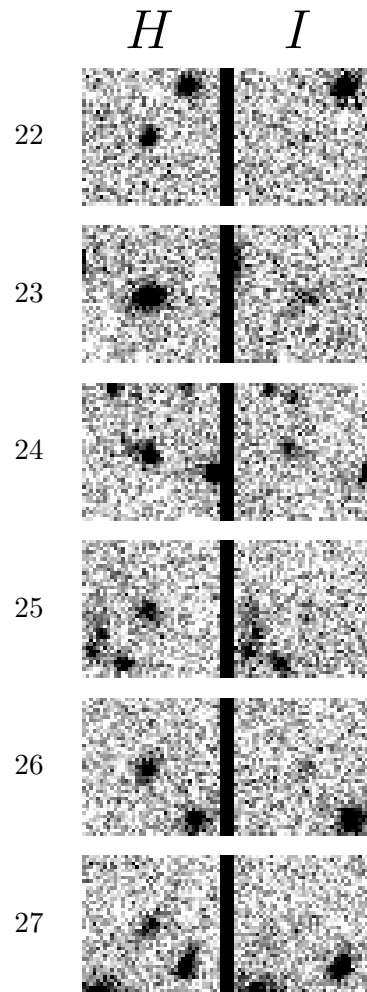


Figure 6.17: SDSSJ1050.4+0017



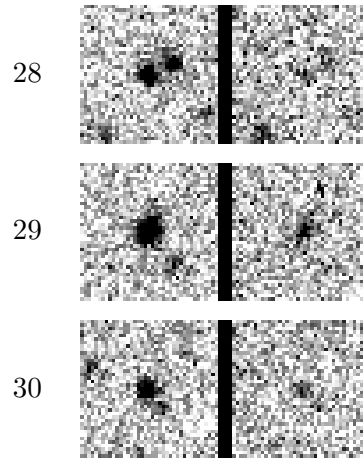
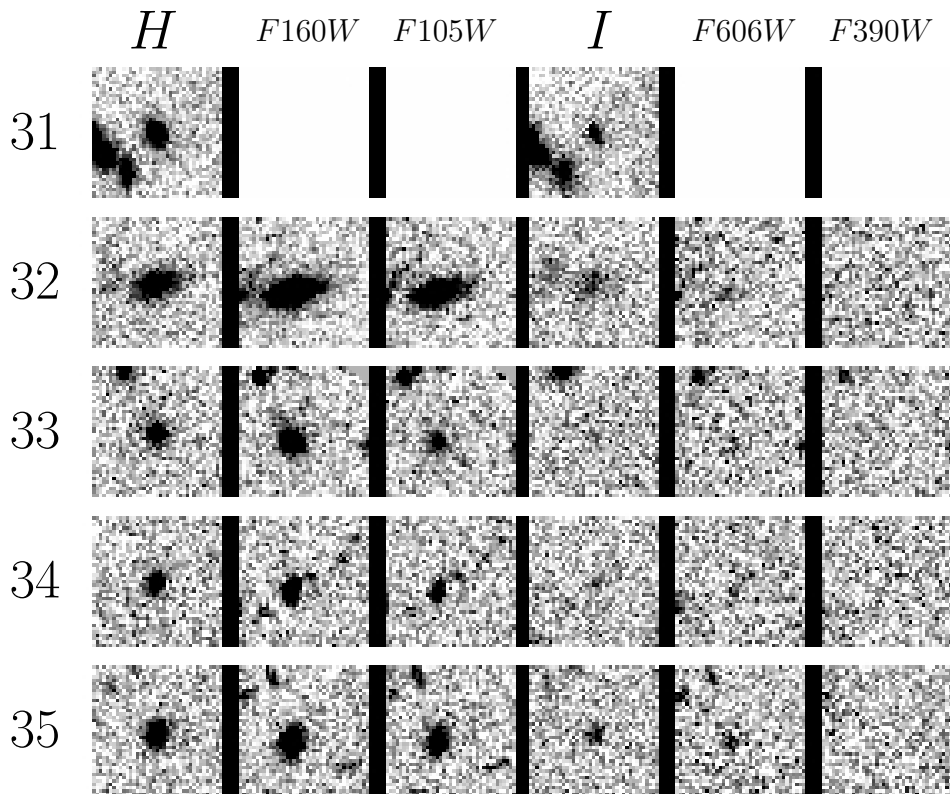


Figure 6.18: SDSSJ1113.1+2356



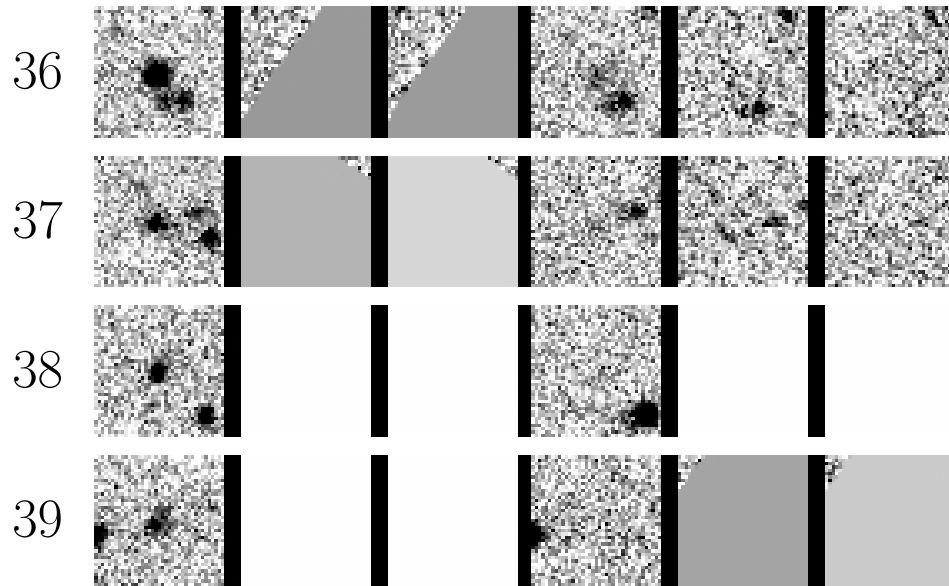
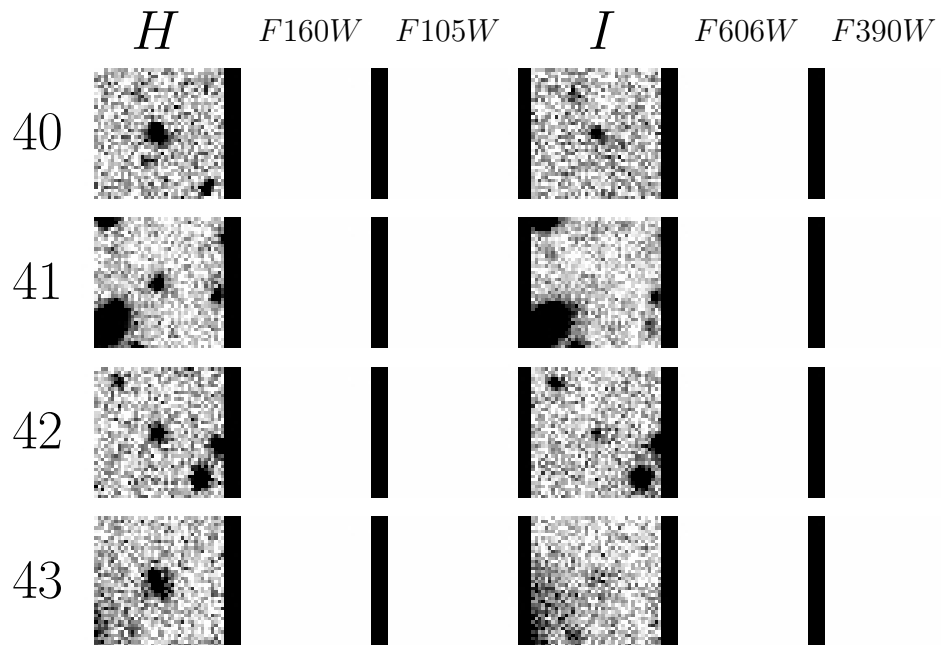


Figure 6.19: SDSSJ1152.5+0930



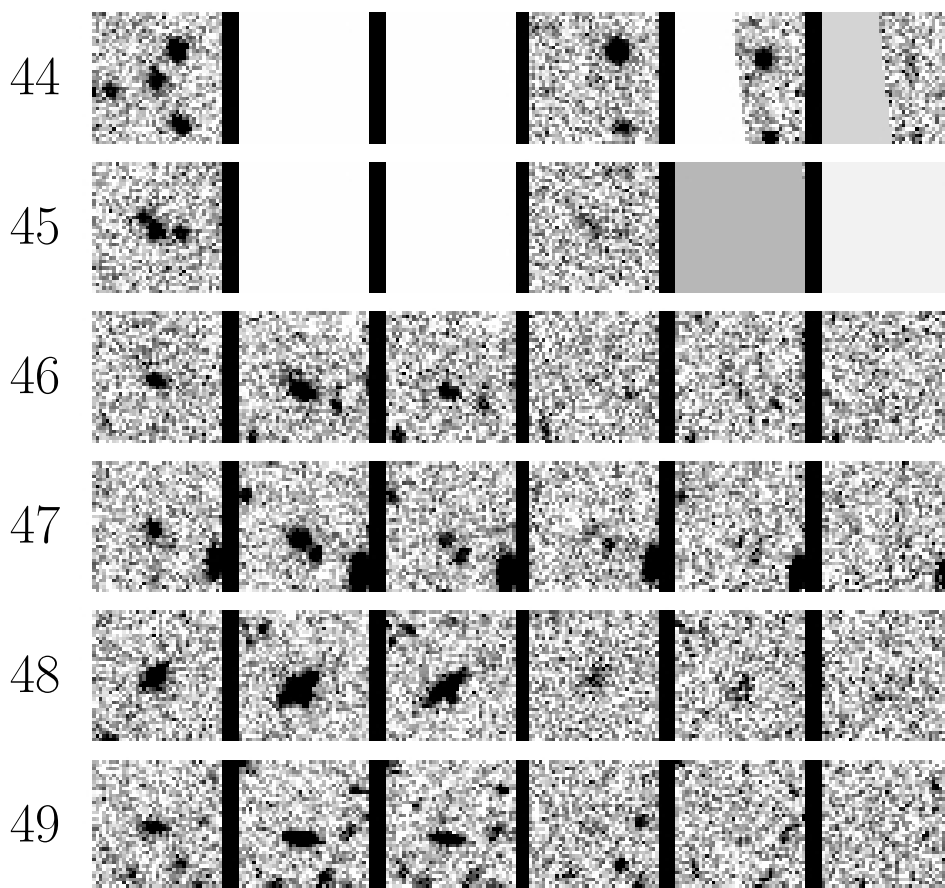


Figure 6.20: SDSSJ1329.3+2243

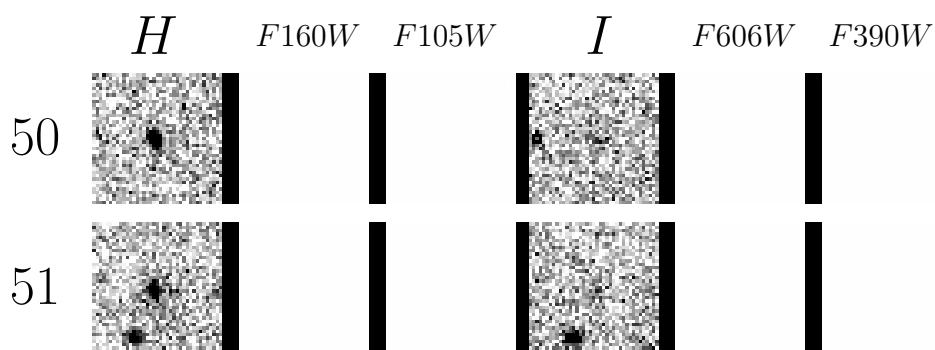
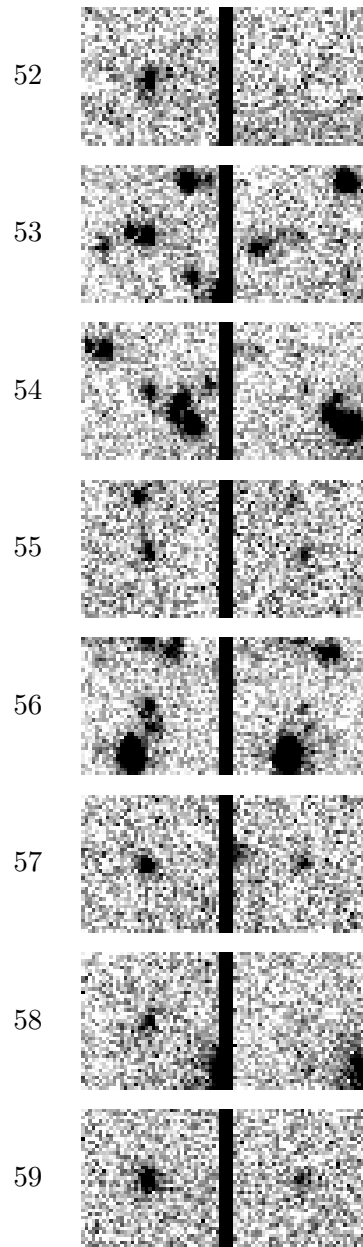


Figure 6.21: SDSSJ1336.0-0331

H *I*



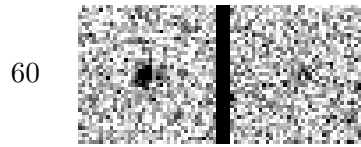


Figure 6.22: SDSSJ1514.5+2245

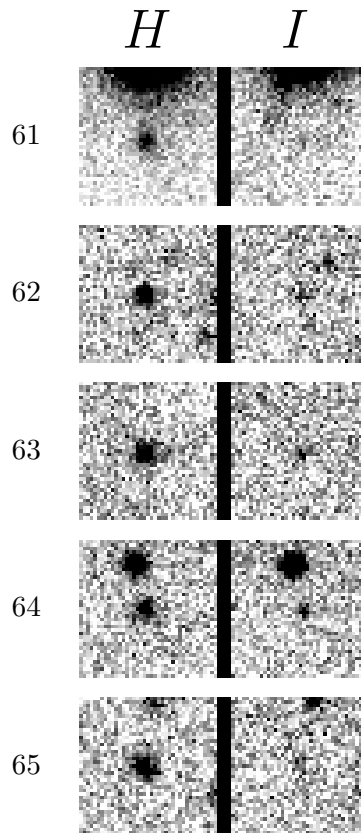


Figure 6.23: SDSSJ1604.1+2244

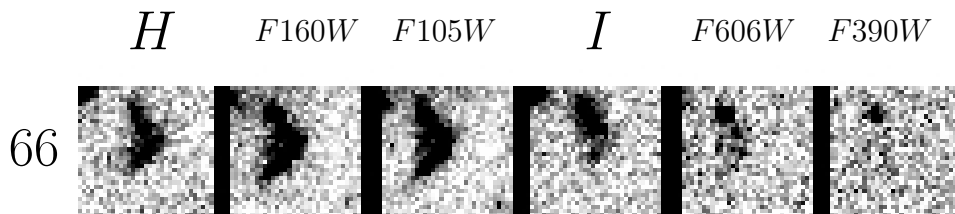


Figure 6.24: SDSSJ1621.3+0607

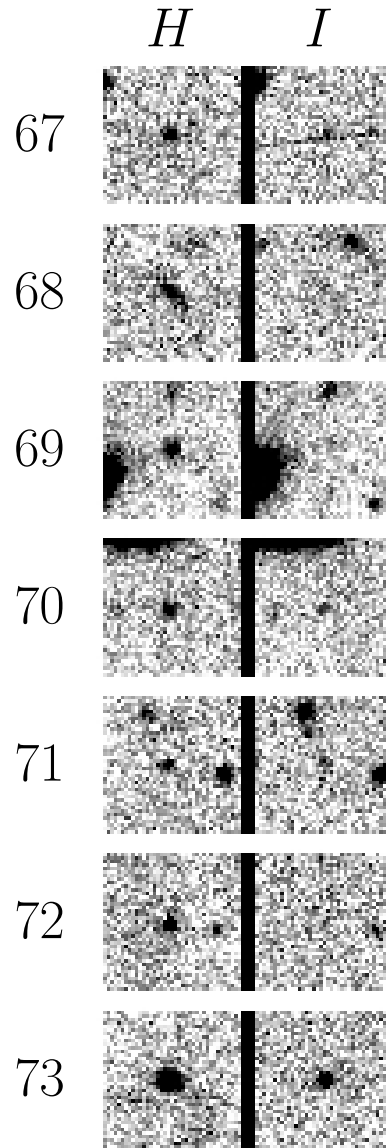


Figure 6.25: SDSSJ1622.2+1006

N	RA (J2000)	Dec	H	I	R	Distance ["]	Priority
01	150.62283	20.53647	21.9	26.4	99.9	76	A
02	150.58711	20.53220	21.6	26.1	99.9	106	A
03	150.63493	20.53160	21.3	24.3	99.9	88	B
04	150.62882	20.52863	21.3	24.3	99.9	65	A
05	150.63661	20.52811	21.4	24.8	99.9	86	B
06	150.63742	20.52775	21.3	26.2	99.9	88	B
07	150.62066	20.52295	20.5	24.3	99.9	31	B
08	150.63144	20.52273	22.0	27.9	99.9	62	A
09	150.59878	20.51642	20.9	23.7	99.9	52	A
10	150.59258	20.51315	20.3	23.9	99.9	74	A
11	150.60069	20.50467	21.7	26.0	99.9	63	A
12	150.63500	20.49309	21.4	25.1	99.9	111	A
13	150.61261	20.49237	20.9	24.6	99.9	89	A

Table 6.13: SDSSJ1002.3+2031: LBG candidates, column have the same meaning as Table 6.1

N	RA (J2000)	Dec	H	I	R	Distance ["]	Priority
14	156.99524	13.43874	21.7	25.1	99.9	116	B
15	157.04442	13.43305	20.9	24.0	99.9	110	B
16	157.02591	13.41038	21.8	28.2	99.9	33	B
17	156.99602	13.39444	21.5	24.6	99.9	110	A

Table 6.14: SDSSJ1028.0+1325

N	RA (J2000)	Dec	H	I	R	Distance ["]	Priority
18	162.64898	0.27978	20.9	23.7	99.9	67	B
19	162.64182	0.27455	21.8	24.8	99.9	98	A
20	162.64877	0.26418	22.0	26.1	99.9	102	B
21	162.67406	0.25966	20.9	24.3	99.9	100	A

Table 6.15: SDSSJ1050.4+0017

N	RA (J2000)	Dec	H	I	R	Distance ["]	Priority
22	168.32990	23.96288	21.9	25.6	99.9	133	A
23	168.29564	23.95865	20.8	23.5	99.9	46	B
24	168.28362	23.95131	21.5	24.9	99.9	38	C
25	168.30507	23.94927	21.9	25.7	99.9	39	B
26	168.31681	23.94850	21.8	25.4	99.9	76	B
27	168.32212	23.94389	21.9	132.2	99.9	93	A
28	168.32250	23.93734	21.6	24.1	99.9	99	A
29	168.31812	23.92665	20.6	23.1	99.9	106	B
30	168.31632	23.92558	21.7	24.3	99.9	105	B

Table 6.16: SDSSJ1113.1+2356

N	RA (J2000)	Dec	H	I	R	Distance ["]	Priority
31	178.18001	9.52059	20.6	23.3	99.9	83	B
32	178.20541	9.51777	20.3	22.8	99.9	57	B
33	178.17879	9.50223	21.4	25.3	99.9	65	A
34	178.18582	9.50007	21.9	25.9	99.9	42	A
35	178.19312	9.48855	21.1	24.4	99.9	59	B
36	178.18402	9.48849	20.8	23.5	99.9	73	A
37	178.20926	9.48165	21.9	25.1	99.9	93	A
38	178.17652	9.47775	21.5	26.1	99.9	120	A
39	178.18582	9.47816	21.4	25.4	99.9	102	A

Table 6.17: SDSSJ1152.5+0930

N	RA (J2000)	Dec	H	I	R	Distance ["]	Priority
40	202.41818	22.73976	20.7	24.2	99.9	104	B
41	202.39158	22.73633	21.5	26.6	99.9	56	B
42	202.38401	22.73388	21.8	24.6	99.9	58	B
43	202.41336	22.72770	20.9	24.8	99.9	68	A
44	202.41842	22.72082	21.5	25.2	99.9	80	B
45	202.42013	22.72066	21.5	24.4	99.9	86	A
46	202.40819	22.70932	22.0	25.5	99.9	62	A
47	202.40452	22.70465	21.5	25.0	99.9	68	A
48	202.39479	22.70286	20.9	23.7	99.9	65	A
49	202.38768	22.70195	21.7	25.0	99.9	72	A

Table 6.18: SDSSJ1329.3+2243

N	RA (J2000)	Dec	H	I	R	Distance ["]	Priority
50	203.96988	-3.50613	21.9	25.0	99.9	129	A
51	203.97213	-3.50967	21.9	24.8	99.9	116	A

Table 6.19: SDSSJ1336.0-0331

N	RA (J2000)	Dec	H	I	R	Distance ["]	Priority
52	228.70558	22.77415	21.7	24.5	99.9	79	A
53	228.71580	22.75437	20.9	25.7	99.9	25	A
54	228.71482	22.75354	21.8	25.9	99.9	21	B
55	228.70438	22.74924	22.0	24.7	99.9	18	C
56	228.70787	22.74798	21.6	24.8	99.9	16	C
57	228.71336	22.74386	21.8	24.5	99.9	34	C
58	228.69147	22.74310	21.9	25.7	99.9	66	A
59	228.69239	22.73574	21.0	24.2	99.9	80	C
60	228.71723	22.73443	21.8	24.4	99.9	70	B

Table 6.20: SDSSJ1514.5+2245

N	RA (J2000)	Dec	H	I	R	Distance ["]	Priority
61	241.05805	22.75164	21.2	23.8	99.9	73	A
62	241.05294	22.74577	21.8	25.4	99.9	46	A
63	241.05000	22.72421	21.6	24.5	99.9	52	A
64	241.02155	22.71859	21.9	24.8	99.9	96	B
65	241.02605	22.71836	21.9	25.3	99.9	86	A

Table 6.21: SDSSJ1604.1+2244

N	RA (J2000)	Dec	H	I	R	Distance ["]	Priority
66	245.38055	6.11826	20.6	23.5	99.9	24	B

Table 6.22: SDSSJ1621.3+0607

N	RA (J2000)	Dec	H	I	R	Distance ["]	Priority
67	245.55652	10.10530	21.5	25.0	99.9	69	C
68	245.55566	10.09513	21.2	24.2	99.9	60	A
69	245.56973	10.09208	21.2	132.1	99.9	14	A
70	245.55015	10.09783	21.7	24.7	99.9	80	B
71	245.54556	10.08122	21.8	24.4	99.9	107	B
72	245.55040	10.07844	21.6	24.7	99.9	98	A
73	245.57215	10.07465	20.2	23.2	99.9	72	C

Table 6.23: SDSSJ1622.2+1006

6.3 Correlation Function

The auto-correlation function represents the deviation of a distribution of points (here galaxies) over a Poissonian random distribution (see Appendix G). Due to the surface magnification presents around galaxy clusters, the angular distribution of galaxies is distorted. However, one can study the distribution of the distances between LBGs and the center of the foreground lensing cluster.

The foreground cluster center were estimated by eye as the brightness galaxy or the center of the few (maximum 3) brightest galaxies. Then, for each LBG candidate, a distance to the nearest foreground cluster were measured and for each field, 100 random points were generated to model a random distribution of galaxy. The distance between each random point and the nearest foreground cluster were measured in order to normalize the correlation function. For each angle bin, the cluster distance correlation function were defined as :

$$Corr(\theta, \theta + \Delta\theta) = \frac{DC(\theta, \theta + \Delta\theta)}{RC(\theta, \theta + \Delta\theta)} \times \frac{Nr}{Nd} \quad (6.1)$$

Where DC (data-cluster) is the number of galaxy with a separation angle between θ and $\theta + \Delta\theta$ from the foreground cluster center; RC (random-cluster) is the number of random points with a separation angle between θ and $\theta + \Delta\theta$ from the foreground cluster center; Nr is the total number of random points ($100[points] \times 24[fields]$) and Nd is the total number LBG candidates (140).

The measured overdensity factor or “foreground cluster-LBG candidates correlation function” is presented in Figure 6.26. Around the foreground cluster, the density of LBG candidates is higher than for an uniform distribution. This is due to the luminosity magnification provided by the gravitational lensing effect from the foreground cluster and to the magnitude limited sample considered. In the other hand, far from the cluster, the density of LBG seems to be lower than for an uniform distribution but this is due to normalisation effects: as there is no control image, the integral of the correlation function is imposed to be zero on the cluster images. In other words : if there is an over-density here, to get the average density on the whole images, it is necessary to have

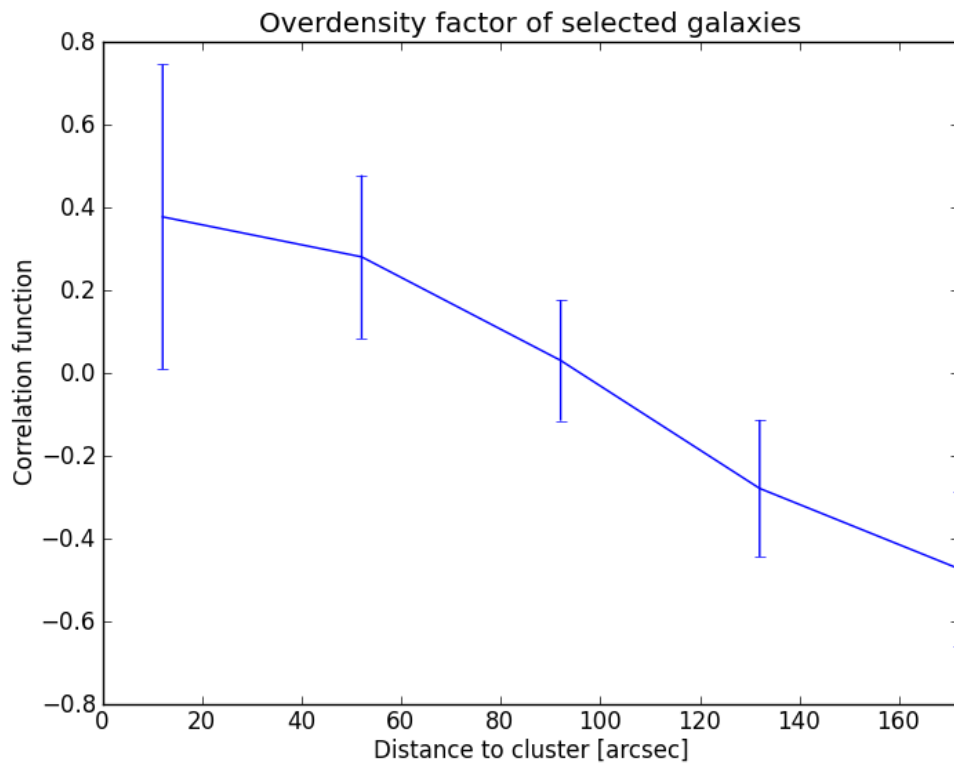


Figure 6.26: Overdensity factor of the LBG candidates according to their angular distance from the foreground cluster center.

a lower density there. A control image, far from a foreground lensing cluster would be necessary in order to correctly normalise the distribution of LBG candidates.

Appendix A

Geometry of a gravitational lens

Mass is curving space and time and its geodesic. A light ray passing through a gravitational field will be deviated by this field. The deflection angle is a 2D angle $\hat{\alpha}$ defined in the plane of the lens. Its value is :

$$\hat{\alpha}(\xi) = \frac{4GM(\xi)}{c^2\xi} \quad (\text{A.1})$$

Where ξ is the impact parameter, a two-dimensional vector in the lens plane. And M is the encircled mass inside a cylinder of radius $|\xi|$ around the lens. The demonstration of this equation is the object of Appendix 2. This can be seen as a kind of ratio of Energy gravitational by kinetic. In units of Schwarzschild radius ¹, $\hat{\alpha}$ the deflection angle is twice the inverse of the impact parameter.

As an example, the Schwarzschild radius of the Sun is 2.95 km and the solar radius is 6.96 ± 10^5 km. So that a light ray grazing the edge of the Sun is deflected by an angle $(5.9/6.96) \times 10^{-5}$ radians = $1.7''$. Note that this angle is twice the deviation angle made by a Newtonian object moving at velocity c . This is what happens in the lens plane. Now let's consider this situation from distant observer point of view.

Figure A.1 represents the geometry of a gravitational lens system, One can see there the obvious sum of the angles, called the lens equation :

$$\hat{\beta}(\hat{\theta}) = \hat{\theta} - \alpha(\hat{\theta}) \quad (\text{A.2})$$

¹ $R_{Schwarzschild} = \frac{2GM}{c^2}$

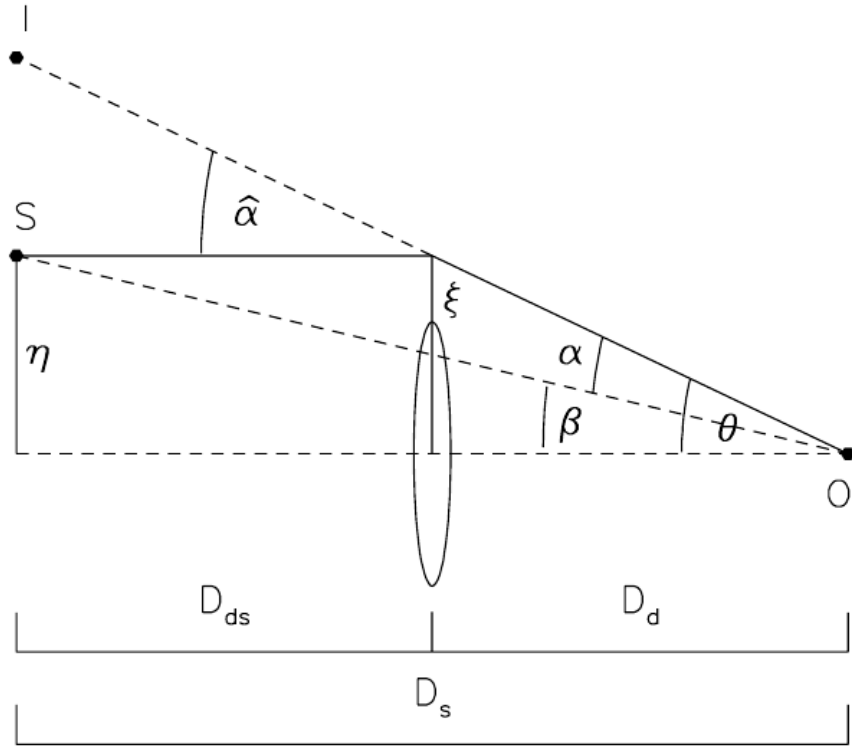


Figure A.1: Geometry of a gravitational lens configuration (Narayan and Bartelmann 1995) The distances D_d , D_s and D_{ds} are the angular distances between the observer and the lens, then observer and the source and between the lens and the source respectively. Angular distances are utilized because gravitational lensing is an issue of angular surface distortion.

Where $\hat{\theta}$ is the apparent angle between the source and the lens center; $\hat{\beta}$ is the observed angle between the lens center and the source if light would have travelled on a straight line. And α is the observed deviation angle. Note that α and $\hat{\alpha}$ is not the same angle: α is the observed deviation angle whereas $\hat{\alpha}$ is the lens plane deviation angle. To find $\hat{\beta}(\hat{\theta})$, an additional equation is needed to link $\alpha(\hat{\theta})$ to $\hat{\alpha}(\hat{\xi})$ which is know by Equation

A.1:

$$\begin{aligned}
SI = \alpha(\hat{\theta}) \times D_s &= \hat{\alpha}(\hat{\xi}) \times D_{ds} \\
\alpha(\hat{\theta}) &= \hat{\alpha}(\hat{\xi}) \times \frac{D_{ds}}{D_s} \\
&= \frac{D_{ds}}{D_s} \times \frac{4GM(\hat{\xi})}{c^2} \frac{1}{\hat{\xi}} \\
\alpha(\hat{\theta}) &= \frac{D_{ds}}{D_s} \times \frac{4GM(\hat{\xi})}{c^2} \times \frac{1}{\hat{\theta}D_d}
\end{aligned} \tag{A.3}$$

Thus, combining Equations A.2 and A.3 leads to :

$$\hat{\beta}(\hat{\theta}) = \hat{\theta} - \frac{D_{ds}}{D_s D_d} \times \frac{4GM(\hat{\xi})}{c^2 \hat{\theta}} \tag{A.4}$$

And, when $\beta = 0$ (i. e., Observer, lens and source are aligned), the symmetry of the situation leads to an ‘‘Einstein ring’’ : the image is a ring with the lens as a center and an angular radius, the ‘‘Einstein radius’’ :

$$\theta_E = \left(\frac{4GM(\theta_E)}{c^2} \frac{D_{ds}}{D_s D_d} \right)^{1/2} \tag{A.5}$$

Considering $G = 4.3 \times 10^{-3} pc M_\odot^{-1} (km/s)^2$, $M = 10^{14} M_\odot$, $c = 3 \times 10^5 km/s$ and $Dd=1254 \text{ Mpc}^2$, $Dds = 934 \text{ Mpc}$ (for a source at $z=6$ and lens at $z=1$) and $Ds = 1203 \text{ Mpc}$ gives $\theta_E = 26''$.

Let’s come back to a general β . For a point lens, Equations A.4 and A.5 imply:

$$\hat{\beta} = \hat{\theta} - \frac{\theta_E^2}{\hat{\theta}}$$

Which has 2 solutions :

$$\theta_\pm = \frac{1}{2} \left(\beta \pm \sqrt{\beta^2 + 4\theta_E^2} \right) \tag{A.6}$$

Therefore a point source and a point lens lead to a multiple images. These images have the same colour as a gravitational lens is achromatic. But if one of the images crosses some gas or dust contained in the lens, then it will be redder than the other.

Equation A.5 of the Einstein radius, reveals that θ_E depends on $M(\theta_E)$, the mass contained in a circle of radius θ_E in the lens plane. Can we imagine a lens surface density profiles such that θ_E spreads from 0 to infinity ? This surface density profile would then be a perfect lens. To determine if such a profile exist, suppose $\beta = 0$. And

² at $z=6$; angular distance = 1200 Mpc so 1Mpc = 2.86 min

for symmetry issues, this profile only depends on θ . So it is called $\Sigma(\theta)$. And equation A.5 can be written :

$$\int_0^\theta (\Sigma(\theta) \times 2\pi\theta \times d\theta) = \theta^2 \frac{c^2}{4G} \frac{D_s}{D_{ds}D_d} \quad (\text{A.7})$$

The lens is perfect if θ vanishes, which means that the observer see a Einstein ring at all radius. In that case, the density profile, called the critical density:

$$\Sigma(\theta) \equiv \Sigma_{cr} = \frac{c^2}{4\pi G} \frac{D_s}{D_d D_{ds}} = 0.35g.cm^{-2} \left(\frac{D}{1Gpc} \right)^{-1} \quad (\text{A.8})$$

Where D is the reduced length $D = \frac{D_d D_{ds}}{D_s}$. Note that there are lots of other ways to define the critical density. For example this is the density that makes equation A.2 linear in θ . It should be called the perfect surface density because it is calculated assuming a perfect lens.

Gravitational light deflection preserves surface brightness (because of Liouville's theorem), but the apparent solid angle of a source is modified. The total flux received from a gravitationally lensed image of a source is therefore changed in proportion to the ratio between the solid angles of the image and the source.

$$magnification = \mu = \frac{\Omega(Image)}{\Omega(Source)} \quad (\text{A.9})$$

Where $\Omega(Source)$ is the solid angle of the source which would be observed if light followed a straight line.

$$\mu = \frac{\int 2\pi\theta d\theta}{\int 2\pi\beta d\beta} = \frac{\theta}{\beta} \frac{d\theta}{d\beta} \quad (\text{A.10})$$

The lens equation, for not unresolved sources then gives :

$$\mu_{\pm} = \left(1 - \left[\frac{\theta_E^4}{\theta_{\pm}^4} \right]^4 \right)^{-1} = \frac{u^2 + 2}{2u\sqrt{u^2 + 4}} \pm \frac{1}{2} \quad (\text{A.11})$$

Where $u = \beta/\theta_E$

Lens Mapping : for an extended lens, the lens equation is defined by its Jacobian in the vicinity of an arbitrary point.

$$A \equiv \frac{\partial \hat{\beta}}{\partial \hat{\theta}} = \left(\delta_{ij} - \frac{\partial \alpha_i(\hat{\theta})}{\partial \theta_j} \right) = \left(\delta_{ij} - \frac{\partial^2 \psi(\hat{\theta})}{\partial \theta_i \partial \theta_j} \right) = M^{-1} \quad (\text{A.12})$$

Where M is the magnification tensor

$$\hat{\nabla}_{\theta}\psi = \hat{\alpha} \tag{A.13}$$

And

$$\psi(\hat{\theta}) = \frac{D_{ds}}{D_l D_s} \frac{2}{c^2} \int \phi(\hat{r}) dz \tag{A.14}$$

And $\phi(\hat{r})$ is the Newtonian potential of the lens. The local solid-angle distortion due to the lens is given by the determinant of A . Therefore the magnification is given by

$$\frac{\delta\hat{\theta}^2}{\delta\hat{\beta}^2} = \det M = \frac{1}{\det A} \tag{A.15}$$

Note that here the proper time parameters were not mentioned and geometric parameters were employed. But all the equations above can be derived by the proper time and the fact that a light will always follow a path that is a local optimum of proper time. Then, one can derive the time delay between two images.

Appendix B

The metric of light deviation

B.1 Connection coefficients

The Christoffel coefficients are defined by :

$$\Gamma_{\beta\gamma}^{\alpha} = \frac{1}{2}g^{\alpha\delta}(g_{\delta\beta,\gamma} + g_{\delta\gamma,\beta} - g_{\beta\gamma,\delta}) \quad (\text{B.1})$$

Where g is the metric tensor and the “,” represents the derivative.

Then the Rieman-Christoffel curvature tensor is linked to the Christoffel coefficients by :

$$R_{\beta\gamma\delta}^{\alpha} = -2 \left(\Gamma_{\beta[\gamma,\delta]}^{\alpha} + \Gamma_{\beta[\gamma}^{\epsilon} \Gamma_{\delta]\epsilon}^{\alpha} \right) \quad (\text{B.2})$$

Where the bracets means : without bracets - inverse what is in the bracets.

This 4⁴ values tensor is contracted to define the Ricci tensor and then the Ricci parameter :

$$R_{\alpha\beta} = R_{\alpha\gamma\beta}^{\gamma} \quad (\text{B.3})$$

$$R = R_{\alpha}^{\alpha} = g^{\alpha\beta} R_{\alpha\beta} \quad (\text{B.4})$$

We can thought define the Einstein equation :

$$\boxed{G^{\alpha\beta} \equiv R^{\alpha\beta} - \frac{1}{2}Rg^{\alpha\beta} = \frac{8\pi G}{c^4}T^{\alpha\beta}} \quad (\text{B.5})$$

Where T is the energy impulsion tensor defined below. Equation B.5 gives the relation between the size of space and its energy content.

$$T^{\alpha\beta} = \rho u^\alpha u^\beta$$

$$u = \frac{dx}{d\tau}$$

Where ρ is the density and x the space time coordinate.

B.2 Quasi-Minkowschy space

Suppose a particle much slower than light and with rest mass dominating its energy , ie:

$$\frac{|v|}{c} \ll 1 ; \quad \frac{|p|}{\rho c^2} \ll 1 \quad (\text{B.6})$$

So :

$$T^{00} \approx \rho c^2 ; \quad T^{0i} \approx c\rho v^i ; \quad T^{ij} \approx \rho v^i v^j + p\delta^{ij} \quad (\text{B.7})$$

Then the metric is derived by the Einstein equation (Equation B.5):

$$ds^2 \approx \left(1 + \frac{2U}{c^2}\right) c^2 dt^2 - 8cdt \frac{V \cdot dx}{c^3} - \left(1 - \frac{2U}{c^2}\right) dx^2 \quad (\text{B.8})$$

Where :

$$U(t, x) \equiv -G \int \frac{\rho \left(t - \frac{y}{c}, x + y\right)}{|y|} d^3y$$

$$V(t, x) \equiv -G \int \frac{(\rho v) \left(t - \frac{y}{c}, x + y\right)}{|y|} d^3y$$

Are the delayed potentials. If every object is much slower than light these potentials are not delayed. For example in a galaxy cluster, the typical velocity dispersion is 1000 km/s which is 3000 times slower than light. Therefore, the potentials are considered to displace instantaneously.

B.3 Schwarzschild metric

Consider a source localised at the floor of a spaceship of height Δr . The light will last $\Delta r/c$ in the referential of the ship to reach the roof. If the ship is at rest according in

earth referential at $t=0$ in free fall in a gravitational field of acceleration g : its velocity according to earth when the light reach the roof is :

$$v = g \frac{\Delta r}{c} \quad (\text{B.9})$$

The change in frequency of the light ($\Delta\nu$) between the earth and ship referential is then :

$$\frac{\Delta\nu}{\nu} = \frac{v}{c} = \frac{g\Delta r}{c^2} \quad (\text{B.10})$$

So the period, t is defined by :

$$\begin{aligned} \frac{1}{t(r)} &= \nu \\ \frac{1}{t(r+\Delta r)} &= \nu - \Delta \\ &= \nu \left(1 - \frac{g\Delta r}{c^2}\right) \\ &= \nu \left(1 - \frac{GM\Delta r}{r^2 c^2}\right) \end{aligned} \quad (\text{B.11})$$

At first order :

$$t(r + \Delta r) = t(r) \left(\frac{1 + GM\Delta r}{r^2 c^2} \right)$$

Integrating over r :

$$t(r) = t(\infty) \left(1 - \frac{GM}{rc^2} \right) \quad (\text{B.12})$$

The metric can be found by differentiation :

$$\begin{aligned} dt^2(r) &= dt^2(\infty) \left(1 - \frac{2GM}{rc^2} \right) \\ d\tau^2 &= dt^2 \left(1 - \frac{2GM}{rc^2} \right) \end{aligned}$$

Where $d\tau$ is the proper time and dt the coordinate time. The same consideration as above but considering the wavelength of the light and not the frequency any more, leads to :

$$dr' = dr \times \frac{dr^2}{1 - 2GM/rc^2} \quad (\text{B.13})$$

Where dr is the wavelength in the satellite frame and dr' is the wavelength in the earth frame. This new consideration leads to the Schwarzschild metric:

$$\boxed{ds^2 = c^2 d\tau^2 = c^2 dt^2 \left(1 - \frac{2GM}{rc^2} \right) - \frac{dr^2}{1 - 2GM/rc^2} - r^2 d\Omega} \quad (\text{B.14})$$

B.4 Light deviation

Consider a light geodesic (ie: $d\tau = 0$). So at first order in GM/rc^2 (i. e., small deviations), the Scharzchild metric is, in the equatorial plane (ie: $d\phi = 0$) :

$$0 = c^2 dt^2 \left(1 - \frac{2GM}{rc^2}\right) - \left(1 + \frac{2GM}{rc^2}\right) (dx^2 + dy^2) \quad (\text{B.15})$$

The x axis is defined as parallel to the light beam. The y component are determined by the geodesic equation :

$$\frac{D^2 y}{D\lambda^2} = \frac{d^2 y}{d\lambda^2} + \Gamma_{\mu\nu}^2 \frac{dx^\mu}{d\lambda} \frac{dx^\nu}{d\lambda} = 0 \quad (\text{B.16})$$

The deviation is supposed slight, so the only non negligible differentials are $dx/d\lambda$ and $dt/d\lambda$. And Γ_{10}^2 and Γ_{01}^2 vanishes because of the symmetry of the metric. So equation B.16 becomes :

$$\frac{d^2 y}{d\lambda^2} + \Gamma_{00}^2 \left(\frac{dt}{d\lambda}\right)^2 + \Gamma_{11}^2 \left(\frac{dx}{d\lambda}\right)^2 = 0 \quad (\text{B.17})$$

To first order in GM/rc^2 , the connection coefficients are :

$$\begin{aligned} \Gamma_{00}^2 &= \frac{g_{00,2}}{2(1 + 2GM/rc^2)} = \frac{dg_{00}/dy}{2(1 + 2GM/rc^2)} = \frac{GM y}{r^3 c^2} \\ \Gamma_{11}^2 &= \frac{GM y}{r^3 c^2} \end{aligned}$$

Replacing these values in equation B.17 and remembering that $dx^2/dt^2 = c^2$ gives :

$$\frac{dy^2}{dx^2} = -\frac{2GM y}{r^3 c^2} \quad (\text{B.18})$$

Assuming a slight deviation with impact parameter b, the deviation angle is derived :

$$\hat{\alpha} = \frac{dy}{dx} = \int \frac{d^2 y}{dx^2} dx = \boxed{\frac{4GM}{c^2 b} = \hat{\alpha}} \quad (\text{B.19})$$

The path of light is curved, which usually provides a convergent length increasing the apparent surface of a source without modifying the surface brightness.

Appendix C

Example of a asctoldac configuration file

Asctoldac is a routine converting ASCII catalogues to LDAC catalogues. A LDAC catalogue is a binary file with a header defining the content and type of the columns. This header and finally the binary codification are defined in asctoldac.conf configuration file needed for the asctoldac routine. Here is an example of such a configuration file.

```
# 1 NUMBER          Running object number
COL_NAME = NUMBER
COL_TTYPE = SHORT
COL_HTYPE = INT
COL_COMM = "Running object number"
COL_UNIT = ""
COL_DEPTH = 1
# 2 FLUX_AUTO      Flux within a Kron-like elliptical aperture    [count]
COL_NAME = FLUX_AUTO
COL_TTYPE = FLOAT
COL_HTYPE = FLOAT
COL_COMM = "Flux within a Kron-like elliptical aperture    [count]"
COL_UNIT = "count"
```

```

COL_DEPTH = 1
# 2 X_WORLD          Barycenter position along world x axis          [deg]
COL_NAME = X_WORLD
COL_TTYPE = FLOAT
COL_HTYPE = FLOAT
COL_COMM = "Barycenter position along world x axis          [deg]"
COL_UNIT = "deg"
COL_DEPTH = 1
# 3 Y_WORLD          Barycenter position along world y axis          [deg]
COL_NAME = Y_WORLD
COL_TTYPE = FLOAT
COL_HTYPE = FLOAT
COL_COMM = "Barycenter position along world y axis          [deg]"
COL_UNIT = "deg"
COL_DEPTH = 1
# 4 NUMBER_ASSOC    Number of ASSOCIated IDs
COL_NAME = NUMBER_ASSOC
COL_TTYPE = SHORT
COL_HTYPE = INT
COL_COMM = "Number of ASSOCIated IDs  ‘‘
COL_UNIT = ""
COL_DEPTH = 1

```

Appendix D

On the way Scamp can work

This appendix comes from a very interesting talk with Vincent Zuc. It is written for a curious reader and for me not to forget it. It is describing different methods to match two images thanks to catalogues of some reference points (called stars for simplicity) of the two images.

- A Delaunays triangulation is made over the two images. Then one sorts triangle sides by decreasing sizes and call its a, b, c . The shape of the triangle is saved with two parameters : b/a and c/a . These two parameters are stored in a two dimensional plane. And the triangle which have the same shape should match between each other (ie: be close). One can for example choose the nearest shape for each referenced shape and consider this is the matched triangle. Indeed with a, b, c , some shapes can be matched and the stars to match together can be deduced.
- On each pixel of the reference image, write the distance of the closest star. This can be done iteratively : first the pixels one pixel away from a star, then two pixels away (ie: one pixel away from the pixels one pixel away from a star) and follow this method recursively until all pixels are given a value. This gives an image where each pixel represents the distance to the closest star, the "distance-image". Deform the image that needs to match this reference image, it is now called the "deformed-image". For each star on the deformed image, look at the value of the same pixel on the distance-image. This value is the distance between the star in

the deformed-image and a star in the reference image. Sum the values obtained for each star. Try different deformations to minimise this sum.

- Other cross-correlation techniques can be thought. One can, for each star of the deforming image, make a vector to a star of the reference image. Stock all these vectors and plot its in a 2D graph. One area will be more populated. This is the shift to make. But you need to define a density binning to know what "more populated" means. Moreover, this easy task need the pixel scale and orientation to be well calibrated. Indeed, Scamp itself works much better with a good orientation and pixel scale.
- How does Scamp really work ? First it is assessing the pixel scale and position angle. And then it is calculating the shift in RA,Dec to apply. The PV factor (polynomial deformation) are calculated after.
 1. Pixel scale and position angle : Scamp is making an 2d histogram of pair sources. Angle and log(distance) are the coordinates of the histograms. Two histograms are generated : the reference and the data. Scamp cross correlates its and find the shift to apply in the (scale \otimes angle) space.
 2. Shift in RA Dec : Scamp is also doing a 2d histogram of the data in (Ra \otimes Dec) space. The best shift is calculated the same way.

The binning of the histograms are setted by MATCH_RESOL keyword. If this keyword is set to 0, $R = \sqrt{f_c \min(\rho, \rho_{ref})}$ where ρ and ρ_{ref} are the average density of the fields. This is an other reason to select properly the sources in the catalogues. And $f_c = 0.01$. In crowded field, R is increased to stay higher than the typical astrometric uncertainty.

Appendix E

WCS projection with FITS

header

The TPV World Coordinate System is described here. This is a system of keywords and parameters in the header of a FITS image defining the pixel to WCS projection. This system comes from a proposal from (Calabretta & Greisen 2002).

The TPV projection is evaluated as follows¹.

1. Compute the first order (linear) coordinates transformation from CRPIX (translation) and the CD matrix (rotation). The temporary coordinates ξ and η are defined as :

$$\xi = CD1.1 \times (X - CRPIX1) + CD1.2 \times (Y - CRPIX2)$$

$$\eta = CD2.1 \times (X - CRPIX1) + CD2.2 \times (Y - CRPIX2)$$

2. Apply the distortion transformation using the coefficients in the PV keywords as described below :

$$\begin{aligned}\xi' &= f_{\xi}(\xi, \eta) \\ \eta' &= f_{\eta}(\xi, \eta)\end{aligned}\tag{E.1}$$

¹we used for reference : <http://iraf.noao.edu/projects/ccdmosaic/tpv.html>

The functions f_ξ and f_η are characterized later.

3. Apply the projection from ξ' and η' (in a plane) to Ra Dec (in a sphere). The reference tangent point of the plane on the sphere is given by the 2 CRVAL values. The type of projection is given by the 2 CRTYPE strings with 8 characters. The unit of the projection is defined by CUNIT keywords. Usually "deg" (for degree) is used. Note that the units of ξ , η , f_ξ , and f_η are also CUNIT units.

The distortion functions shown as f_ξ and f_η above are defined as follows where the variable r is $\sqrt{\xi^2 + \eta^2}$. In this convention there are only odd powers of r . Because the even powers are presents in the terms including only ξ or η yet.

$$\begin{aligned}
\xi' = & (PV1.0 + PV1.1 \times \xi + PV1.2 \times \eta + PV1.3 \times r) + \\
& (PV1.4 \times \xi^2 + PV1.5 \times \xi \times \eta + PV1.6 \times \eta^2) + \\
& (PV1.7 \times \xi^3 + PV1.8 \times \xi^2 \times \eta + PV1.9 \times \xi \times \eta^2 + PV1.10 \times \eta^3 + \\
& PV1.11 \times r^3) + \\
& (PV1.12 \times \xi^4 + PV1.13 \times \xi^3 \times \eta + PV1.14 \times \xi^2 \times \eta^2 + PV1.15 \times \xi \times \eta^3 + \\
& PV1.16 \times \eta^4) + \\
& (PV1.17 \times \xi^5 + PV1.18 \times \xi^4 \times \eta + PV1.19 \times \xi^3 \times \eta^2 + \\
& PV1.20 \times \xi^2 \times \eta^3 + PV1.21 \times \xi \times \eta^4 + PV1.22 \times \eta^5 + PV1.23 \times r^5) + \\
& (PV1.24 \times \xi^6 + PV1.25 \times \xi^5 \times \eta + PV1.26 \times \xi^4 \times \eta^2 + PV1.27 \times \xi^3 \times \eta^3 + \\
& PV1.28 \times \xi^2 \times \eta^4 + PV1.29 \times \xi \times \eta^5 + PV1.30 \times \eta^6) + \\
& (PV1.31 \times \xi^7 + PV1.32 \times \xi^6 \times \eta + PV1.33 \times \xi^5 \times \eta^2 + PV1.34 \times \xi^4 \times \eta^3 + \\
& PV1.35 \times \xi^3 \times \eta^4 + PV1.36 \times \xi^2 \times \eta^5 + PV1.37 \times \xi \times \eta^6 + PV1.38 \times \eta^7 + \\
& PV1.39 \times r^7)
\end{aligned} \tag{E.2}$$

η' is defined in the same way put replacing PV1_ by PV2_ . Note that missing PV keywords default to 0 except for PV1.1 and PV2.1 which default to 1. With these defaults if there are no PV keywords the transformation is the identity and the TPV WCS is equivalent to the standard projection specified by CRTYPE (TAN for example). This convention only defines coefficients up to 39 corresponding to a maximum

polynomial order of 7. Implementing the inverse transformation requires inverting the distortion functions. But using a standard iterative numerical inversion based on the first derivative of the functions is not difficult. The derivatives of these functions are straightforward to express and evaluate thanks to the polygonal nature of the functions.

Appendix F

Schechter function

The Schechter function is defined as (Schechter, 1976) :

$$n(x)dx = \phi^* x^\alpha e^{-x} \quad (\text{F.1})$$

For the special case of Luminosity, it is written as :

$$n(L)dL = \phi^* (L/L^*)^\alpha e^{-L/L^*} \quad (\text{F.2})$$

Where ϕ^*, L^*, α are three parameters of the Schechter function. $n(L)$ is the number of galaxies of luminosity L in a slice dL . Luminosity (L) is link to magnitude (M) with :

$$\begin{aligned} L &= 10^{-0.4 \times M} = \exp(\ln(10) \times (-0.4M)) \\ dL &= -0.4 \ln(10) \times L dM \\ n(M) &= n(L) \end{aligned} \quad (\text{F.3})$$

The last equation only tells that there is the same number of galaxy of magnitude M than galaxies of the corresponding luminosity L . Using Equation F.3, Equation F.2 transforms :

$$\begin{aligned} n(M)dM &= -0.4 \ln(10)L \times n(L)dL \\ n(M)dM &= -0.4 \ln(10)\phi^x (10^{-0.4(M-M^*)})^{\alpha+1} \times \exp(-10^{-0.4(M-M^*)}) \end{aligned} \quad (\text{F.4})$$

That is why a LF is said to be flat when $\alpha = -1$ (i. e., asymptotically flat).

Now let's suppose that a surface magnification, given by a gravitational lensing for example. Surfaces are increased by a factor N and the angular surface observed is

decreased by the same factor N . In other words : the luminosity is multiplied by N and the typical number of objects, the normalisation (i. e., ϕ^*) is divided by the same factor N .

$$\begin{aligned} x &= X \times N \\ \phi^* &= \Phi^*/N \end{aligned} \tag{F.5}$$

So the LF becomes :

$$n(L)dL = \frac{\Phi^*}{N}(X \times N)^\alpha e^{-X \times N} \tag{F.6}$$

Where $X = L/L^*$. For low luminosity (the faint end), the exponential factor can be neglected. The faint end slope, α , will not be changed by gravitational lensing. Moreover, the normalisation, Φ will not change for $\alpha = 1$ because the N factors out of the exponential vanished.

So to resume, the effect of gravitational lensing on the factor :

- α , is null
- L^* , is positive : L^* increases with magnification (proportionally).
- Φ^* , is positive if $\alpha > 1$ and negative if $\alpha < 1$, null is $\alpha = 1$.

When the Schechter function is very degenerate, one can also fit a broken power law of the form :

$$\phi^* = \frac{\phi(m)}{10^{0.4(\alpha_1+1)(m-m^*)} + 10^{0.4(\alpha_2+1)(m-m^*)}} \tag{F.7}$$

Note that at high redshift, results from these 2 fitted forms can differ a lot, due to the unconstrained faint end : let's quote from (Henry et al 2007) : "If the $z = 6$ measurement by Bouwens et al. (2006) is a good indicator of the population at $z \sim 9.5$, then the density of sources which we expect is of order 0.01 degree^{-1} in the Schechter form, and about 1 degree^{-1} in the broken power law LF".

Integration of the LF : total flux There is no analytic form to integrate a Schechter function. But, as every defined function, one can get an approximation arbitrary close. Figure F.1 presents the flux lost due magnitude limited integration of the luminosity function.

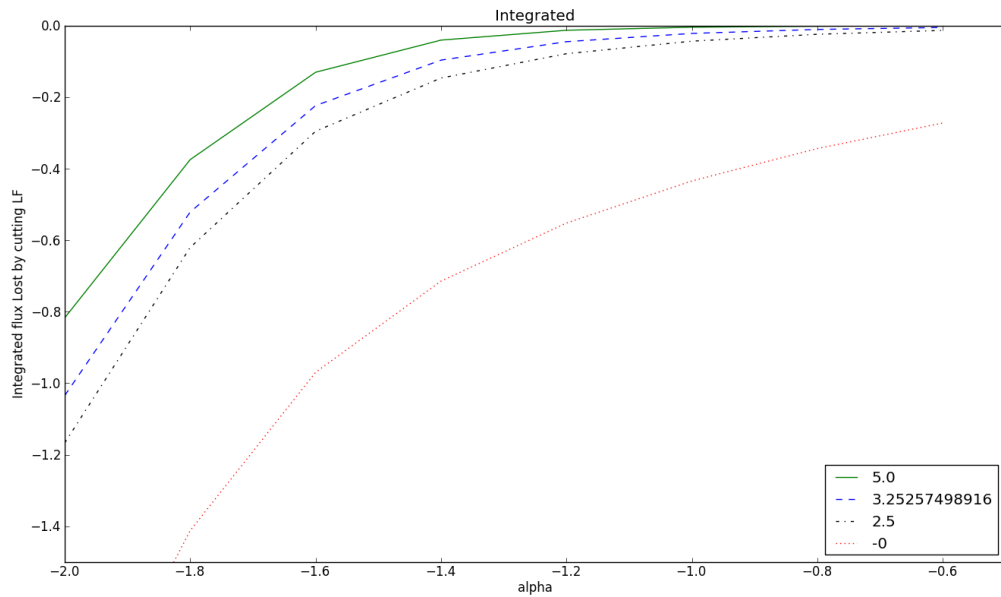


Figure F.1: The flux lost of the integrated flux (in log) in a Schechter function the integral of the flux is limited to a certain magnitude compared to the total integrated flux. This ratio is represented according to the α coefficient of the Schechter. Note that for $\alpha = -2$, the total integrated the total flux is divergent. From the top to the bottom, the curves represent the flux lost if the LF is integrated up to $\text{mag} = M^* + 5, M^* + 3.25, M^* + 2.5, M^*$. Notice that for $\alpha = -1.6$ and above, the errors in alpha and M^* are not dramatic but for alpha lower than -1.6, one need to have a good estimation of alpha, which is difficult. Otherwise, one can fit the data with a typical broken power law.

Appendix G

Auto-correlation Function

The auto correlation function or 2 points correlation function is employed to measure the deviation of a distribution (of galaxies in the sky or mushrooms on the ground) to a random distribution. One can also measure the correlation of human on the ground, to see that humans usually gather in town rather than being homogeneously distributed. But if one want to see if humans and mushrooms are correlated, this is not an auto-correlation function any more.

The auto-correlation function is usually scale dependant if our system is not conformally invariant. Therefore, in the general case, it will depend on r , the separation between 2 objects. According to (Peebles 1980) the two-point correlation function $\xi(r)$ determines a probability dP to find simultaneously two objects at a distance r from each other.

Let's consider 2 volume elements δV_1 and δV_2 around these two objects. Usually, δV_1 and δV_2 are chosen equal. If these 2 objects are in a sample with number density n , the probability to find the 2 objects simultaneously in δV_1 and δV_2 is :

$$dP = n^2[1 + \xi(r)]\delta V_1\delta V_2 \tag{G.1}$$

And if the objects are randomly distributed, we find $\xi(r) = 0; \forall r$. An equivalent way of describing the 2 points correlation function is by the contrast of density, the departure

from an equally distributed distribution with $\langle \rho(r) \rangle = n$:

$$\langle \rho(x)\rho(r+x) \rangle = n^2[1 + \xi] \quad (\text{G.2})$$

Where the mean is taken on x .

In the practice, there are four different estimators present in the literature to estimate $\xi(r)$:

1. Peebles & Hauser estimator: $\xi_{PH}(r) = \frac{N_r}{N} \frac{DD(r)}{RR(r)} 1$;
2. Davis & Peebles estimator: $\xi_{DP}(r) = \frac{2N_r}{N1} \frac{DD(r)}{DR(r)} 1$;
3. Hamilton estimator: $\xi_H(r) = \frac{4NN_r}{(N1)(N_r1)} \frac{DD(r)DR(r)}{RR(r)DR(r)} 1$;
4. Landy & Szalay estimator: $\xi_{LS}(r) = \frac{N_r(N_r1)}{N(N1)} \frac{DD(r)}{RR(r)} 2 \frac{(N_r1)}{N} \frac{DR(r)}{RR(r)} + 1$.

Where DD, RR and DR are the number of pairs at distance r in the data-data, random-random and random-data samples. N and N_r are the total number of pair in the data and random sample. One can take more data in the random sample and compute it $RR(r)$ only once. These different estimators are nearly equivalent on small scales.

The error of the correlation function, $\xi(r)$ can be estimated as follows. In the absence of clustering (Poissonian distribution [ie: homogeneously random]), $\langle \xi \rangle = 0$ and $\langle \xi^2 \rangle = 1/N_p$. Where N_p is the number of independent pairs within a given bin of radius (Peebles 1980). One could extrapolate and estimate for $\xi \neq 0$:

$$\frac{\Delta \xi}{1 + \xi} = \frac{1}{\sqrt{N_p}} \quad (\text{G.3})$$

Appendix H

Other points

I enumerate here some points, errors I made. These are very little issues but which can take hours or days to find because some of them are not obvious. This Appendix is in my opinion the most important, please have a quick look, it may help you in a future work.

- Sextractor : it computes the magnitude considering a ZPT=0 and EXPTIME=1
- FITS : sometimes one needs to remove the quotes of the numbers in the header values.
- Swarp : the polygonal deformation should be of an order lower or equal to 2 same for scamp and I guess sextractor
- Python : it uses `np.log10` and not `np.log` for the log in base 10.
- Python : `matplotlib` gets in conflicts with `pywcs`. And the WCS projection is badly computed. So import `matplotlib` just before the plot lines.
- Filters : Check the reference filter and your filter before computing a ZPT, for example, our I filter is closer to Johnson than to SDSS.
- Organization image : separate objects at the beginning, before separating by chip or filter. In this way, one can do the whole work for one object, see the difficulty and therefore make a good step by step pipeline.

-
- Iraf : after killing an process make the command "flpr" several times. flpr stands for flash process.
 - Try to propagate an weightmap in order not to need to discard some regions of an image, a to be able to compute a mega images composed of many chips (not easy).
 - Organisation software : for reading and plotting with python, better define global variables than classes because then one gets lost with classes variables and lot of if statements. In the same way, make just a simple plot function and call it many times to get a multi-plot.
 - IRAF : do not forget to remove an image before making a new image of the same name. Otherwise, nothing is done.
 - Algebraic computation : In python I multiplied an Image by 256. It was like multiplying by 0 because in 8 bits, $256=0$!!
 - Organisation image : While reducing images you need to store all your operations from the raw to be able to do it again automatically with only one software : organize your routines as your images.
 - FITS header : the date represents the last date of modification. It is for example modified by Swarp.

Abbreviations

2MASS	Two Micron All Sky Survey
ACF	Angular Correlation Function
ADU	Arbitrary Differential Unit
ASCII	American Standard Code for Information Interchange
BPM	Bad Pixel Map
CATS	astrophysical CATalogs support System
CCD	Compact Camera Device
CMB	Cosmological Microwave Background
CMD	Color Magnitude Diagram
DLA	Damped Lyman Absorber
DS9	Deep Space 9
ESO	European Southern Observatories
EW	Equivalent Width
FIR	Far Infra Red
FITS	Flexible Image Transport System
FORS2	FOcal Reducer/low dispersion Spectrograph 2
FOV	Field Of View
FTP	File Transfer Protocol
GIF	Graphics Interchange Format
GISSEL	Galaxy Isochrone Synthesis Spectral Evolution Library
GL	Gravitational Lens
HAWAII-2RG	HgCdTe Astronomy Wide Area Infrared Imager

	with 2k2 Resolution reference pixels and Guide Mode
HAWK-I	High Acuity Wide-Field K-band Imager
<i>H</i>	NIR band
HSB	Hight Surface Brightness
HTML	Hypertext Markup Language
HTTP	HyperText Transport Protocol
HTTPS	HyperText Transport Protocol Secure
<i>I</i>	Optical band
IGM	Inter-Galactic Medium
IMACS	Inamori-Magellan Areal Camera and Spectrograph
IMF	Initial Mass Function
IRAF	Image Reduction and Analysis Facility
IR	Infra Red
ISM	Inter-Stellar Medium
IVOA	International Virtual Observatory Alliance
JPEG	Joint Photographic Experts Group
LAE	Lyman Alpha Emitters
LDAC	Leiden Data Analysis Center catalogue format
LEDA	Lyon-Meudon Extragalactic Database
LLS	Lyman Limit System
LSB	Low Surface Brightness
MOS	Metal Oxyde Semiconductor
MIR	Middle InfraRed
NAN	Not A Number
N/A	Not Applying
NAO	National Astronomical Observatory (Japan)
NASA	National Aeronautics and Space Administration
NB	Narrow Band
NED	Nasa Extragalactic Database

NIR	Near InfraRed
PDF	Portable Document Format
PGM	Pre Galactic Medium
Pixel	PICture ELe ment
PMM	Precision Measuring Machine
PNG	Portable Network Graphics
PSF	Point Spread Function
PWV	Precipitable Water Vapor
RLG	Red Luminous Galaxy
RMS	Root Mean Square
RON	Read Out Noise
SAMP	Simple Application Messaging Protocol
SCAMP	Software for Calibrating AstroMetry and Photometry
SDSS	Sloan Digital Sky Survey
SED	Spectral Energy Distribution
SExtractor	Source Extractor
SSP	Simple Stellar Population
S/N	Signal sur Noise ratio.
SWarp	Software to Warp images.
URL	Universal Resource Locator
USNO-B1	United States Naval Observatory All-Sky Catalog
USS	Ultra Steep Spectra
WCS	World Coordinates System
WMAP	Wilkinson Microwave Anisotropy Probe
XML	Extensible Markup Language
ZPT	Zero PoinT

Table H.1: Acronyms utilized (column 1) and their meaning (column 2).